POLYMER DERIVED FUNCTIONAL CARBON AND CARBON BASED NANOCOMPOSITES

A Thesis Submitted to the
UNIVERSITY OF PUNE

For the Degree of
DOCTOR OF PHILOSOPHY
In
CHEMISTRY

By
PRASAD ASHOK YADAV

UNDER THE GUIDANCE
Dr. Mrs. JYOTI P. JOG

CO-GUIDE
Dr. SATISHCHANDRA B. OGALE

POLYMER SCIENCE & ENGINNERING DIVISION
NATIONAL CHEMICAL LABORATORY
PUNE – 411 008
INDIA
December 2012

Contents

8. APPENDICES:

Acknowledgements

I would like to take this opportunity to express my deep sense of gratitude to my Ph.D. supervisor Dr. Mrs. Jyoti Jog for giving me an opportunity to pursue Ph.D. with her and all her guidance, help and advice. I am always indebted for her trust, continuous support, and co-operation during the course of this journey. I also wish to express my heartfelt gratitude to her for motherly care, and friendly support throughout this journey.

I have had the honor of being able to work closely with Prof. Satishchandra Ogale at the National Chemical Laboratory for my doctoral thesis for the past four years as my mentor. I thank him for his great support and expert guidance. I am highly inspired by his natural spirit, dedication to science and his oratory skills. He is a very enthusiastic and highly energetic person with incredible amount of knowledge, and is always fascinated to pursue high quality research work, taking untiring efforts towards that. Since teaching as well as research is his passion, he has not only taught me lessons of physics/materials science but also the morals/ethics of the life. This gave me a confidence in a life to choose voluntarily research as my career.

I am sincerely obliged to the Director, National Chemical Laboratory (CSIR-NCL) for giving me opportunity to work at the Institute. I also wish to thank the Head, Physical Chemistry Division and Head, Polymer Science and Engineering Division, NCL for providing the infrastructural facilities to carry out the research work for Ph.D.

I am also grateful to Dr. Mrs. Anjali Ogale (Madam) for her motherly care and blessings throughout my Ph.D. work. I have been fortunate to have enthusiastic project students and friends such as Pravarthana, Anuja, Madhura, Neha, Parag, Punam etc. I wish to express my special thanks to scientists Dr. Beatrice Hannoyer, Dr. Deodatta Phase, Dr. S. Kurungot, Dr. Sangeeta Kale, Dr. A. A. Athawale, Dr. Amit Chawla, Dr. P. Wadgaonkar, Dr. Ashish Lele etc. for their timely help. I would like to thank my labmates and friends Hrushikesh, Kashinath, Rajesh, Sarfaraj, Anup, Sarika, Abhimanu, Harish, Ashish, Arif, Perwez, Tushar, Vivek, Subash, Chetan, Meenal, Lily, Onkar, Vishal, Datta, Mandakini, Shruti, Reshma, Rohan, Abhik, Shradha, Anil, Rounak, Deepti, Pradeep, Pooja, Dhanya, Anirudh, Satish, Satyawan etc. I wish to thank all my teachers from primary schools to Master’s level who educated and nurtured me academically to reach at this destiny.

I sincerely thank various funding agencies CSIR, DST, and UGC, New Delhi, Govt. of India for the research fellowships and travel grants.

I take this opportunity to thank my beloved family members for their support, dedication and love. It gives me a great pleasure to acknowledge all those people whose help, good wishes, encouragement and support have brought this task to the successful conclusion. I genuinely and humbly thank all of them who have directly-indirectly co-operated and supported me to reach to this important stage in my career.

Finally, but most importantly, I wish to thanks for my parent and sister for their motivation to chase my dream to undertake a research carrier and their constant and personal family support during this doctoral thesis work. I also thank them for being there for me for all phases of several such career steps during my education.

--- Prasad Ashok Yadav

Declaration by the Candidate

I declare that the thesis entitled **"POLYMER DERIVED FUNCTIONAL CARBON AND CARBON BASED NANOCOMPOSITES"** submitted by me for the degree of Doctor of Philosophy is the record of work carried out by me during the period from **18th July 2007 to 17th December 2012** under the guidance of **Dr. Mrs. Jyoti Jog** and has not formed the basis for the award of any degree, diploma, associateship, fellowship, titles in this or any other University or other institution of Higher learning.

I further declare that the material obtained from other sources has been duly acknowledged in the thesis.

Prasad Ashok Yadav

Date: 17th December, 2012 **Place: Pune**

सीएसआयआर-राष्ट्रीय रासायनिक प्रयोगशाला
(वैज्ञानिक तथा औद्योगिक अनुसंधान परिषद)
डॉ. होमी भाभा मार्ग, पुणे - 411 008. भारत
CSIR-NATIONAL CHEMICAL LABORATORY
(Council of Scientific & Industrial Research)
Dr. Homi Bhabha Road, Pune - 411 008. India.

CERTIFICATE OF THE GUIDE

CERTIFIED that the work incorporated in the thesis **"POLYMER DERIVED FUNCTIONAL CARBON AND CARBON BASED NANOCOMPOSITES"** submitted by **"Mr. Prasad Ashok Yadav"** was carried out under my supervision/guidance. Such material as has been obtained from other sources has been duly acknowledged in the thesis.

Dr. Mrs. Jyoti Jog
(Supervisor/Research Guide)

Dr. Satishchandra Ogale
(Supervisor/Research Co-guide)

Date: 17th December 2012

Place: Pune

mmunication
annels
NCL Level DID : 2590
NCL Board No. : +91-20-25902000
EPABX : +91-20-25893300
FAX
Director's Office : +91-20-25902601
COA's Office : +91-20-25902660
COS&P's Office : +91-20-25902664
WEBSITE
www.ncl-india.org

Abstract

The technological and scientific potentials of carbon based nanomaterials is certainly bright as revealed in the present study on carbon nanoscrolls, porous graphene, single sheet graphene, magnetite-graphene oxide, carbon coated ZnO etc. Moreover, the ultimate use of these carbon nanomaterials is strongly dependent upon the ability to precisely control their dimension, composition, surface property, phase purity and crystal structure. As the basic building block of these carbon nanostructures is a sheet of carbon in hexagonal network (graphene), these structures have high surface area together with enhanced conductivity, which is important for many applications. This work hence opens the new perceptive towards promising synthesis methods and developments of graphene based nanostructures to stretch the applications of these fascinating nanomaterials in the field of energy and environment.

During the course of the present research work, we have investigated various methods for the synthesis of carbon based nanomaterials and their applications for energy storage, field-effect transistor and photocatalysis.

The key concepts in nanoscience and a literature survey of the properties and applications of carbon nanomaterials have been discussed in the previous sections. These constitute the **First Chapter**.

In the **Second Chapter**, a brief overview of the techniques used for the synthesis of carbon nanomaterials is presented. Furthermore, a general outline of the instruments and methods used for the characterization of these carbon nanomaterials is also presented.

The **Third Chapter** discusses the synthesis of carbon nanoscrolls starting from pyrolysis of polymer. Pyrolysis of poly (acrylic acid co maleic acid) sodium salt leads to formation of carbon form and sodium carbonate. The carbon part of decomposition products undergo self-assembly upon its aqueous soaking to form carbon nanoscrolls. We also discuss synthesis of magnetite-graphene oxide (M-GO) composite by pyrolysis route.

In the **Fourth Chapter**, we have demonstrated the synthesis of hierarchically porous graphene with hexagonal nonopores. It is a catalyst-free synthesis leading to single-layer-graphene-assembled carbon without use of any template. The as-synthesized sample exhibits high surface area of about 1720 m^2/g and shows bulk specific

conductivity of 23 S/m. The material exhibits excellent supercapacitance performance in aqueous medium with maximum specific capacitance of 154 F/g at a current density of 0.5 A/g.

In the **Fifth Chapter,** we report on the synthesis of large area single layer graphene. It is a catalyst-free synthesis without use of any template. The as-synthesized graphene exhibits high surface area of about 350 m^2/g and shows bulk specific conductivity of 90 S/m. This graphene also shows good CV behaviour with approximate specific capacitance of 120-140 F/g. We have used this graphene for making graphene/P3HT composite and used this composite as a channel material for field effect transistor application.

In the **Sixth Chapter**, we report on synthesis of anisotropic structure of carbon coated ZnO nanoroads. The as synthesized carbon coated ZnO shows efficient visible light photocatalytic activity. Moreover it is also resistant to degradation by and scavenging of the dye without hindrance to charge transfer; a characteristic of significant interest to optical device applications.

The **Seventh Chapter** summarizes the work described in this thesis by presenting the salient features of the work and also mentions the possible avenues for future investigations.

Appendix I follows the work done on investigation of observation of strong ferroelectricity in hydrated sodium carbonate.

Chapter I

Introduction

This chapter introduces carbon and carbon composites especially emphasizing the properties and applications of carbon nanomaterials. A literature survey on synthesis, properties and applications of different carbon structures and composites with critical review of carbon nanostructures is presented in this chapter. The chapter focuses on two main carbon nanomaterials applications: supercapacitor and photocatalysis, having impacts on energy storage and pollution control of environment. At the end of the chapter, the motivation and objective of the presented research is elaborated.

1.1 Introduction

In the modern edge of human civilization the progress of science and technology has contributed significantly to the evolution of civilization. The mankind has experienced the industrial revolution followed by space revolution which is still in continuation with the advent of nano revolution since last few decades. The course of these developments is always supported by discoveries of novel materials having various interesting properties. The understanding that ‘size reduction of materials affects the physiochemical properties significantly’ has opened the doors to an exciting field of nanomaterials. Nanomaterials are engineered structures with at least one of its dimensions less than 100 nm. Figure 1.1 shows the comparison of size of nano scale object i.e. carbon nanotube with that of a eukaryotic cell, a diamond, oil rig and the Sun. With this figure we can appreciate the smallness of size of nanomaterials. The nanometer size of a material increases the surface to volume ratio. Also there is dominant emergence of quantum size effects due to decrease in the volume of nanomaterials (size confinement effect). This can change or enhance chemical reactivity, electronic, optical, mechanical, magnetic, and transport characteristics of nanomaterial as compared to their bulk analogues. This has resulted in exploring new strategies for synthesis of nanomaterials which will have the promise for solving global problems related to energy and environment.

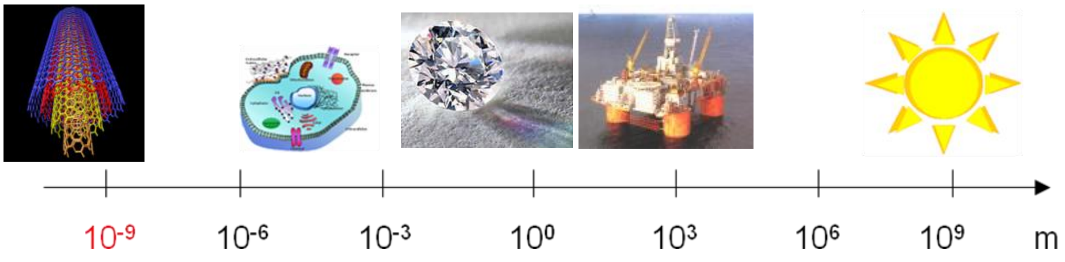

Fig. 1.1 *Size of carbon nanotubes in comparison with that of eukaryotic cell, diamond, Oil refinery and Sun [Re-ffolk.uio.no/kaidk/Nanocarbon1.ppt,* nanotech-now.com*]*

It is interesting to see that the demand for energy is increasing and set to continue growing in the future as well. It is expected that fossil fuels will continue to provide more than 90 per cent of the world’s total commercial energy needs, accounting for 95 per cent of the growth in demand over the next 20 years [1]. But with the increased use of fossil fuels there is increase in the green house gases such as CO_2, Carbon monoxide, nitrogen oxide and other harmful toxic waste products [1]. One of the solutions for decreasing the amount of these gases in environment is carbon capture and storage, where carbon dioxide is captured from large stationary sources, such as power stations and industrial sites, and is then injected into deep geological formations, where it is stored. The technology already exists but the investments are very expensive. There are other clean sources of energy like hydro, nuclear and new renewable, but contribution from these sources will flatten out in near future. Also some of these new renewable with extremely high growth rates make the growth in absolute terms rather limited due to their low initial base. Hence future development crucially depends on its long-term availability of energy in increasing quantities from sources that are dependable, safe, and environmentally sound. At present, no single source or mix of sources is at hand to meet this future need. This is because a lot of primary energy is wasted due to inefficient design or running of the equipment used to convert it into the services required as well as in the storage and transport of energy. In this regard it should be considered that storage of energy is as important as its generation. Choices must be made, but in the certain knowledge that choosing an energy strategy inevitably means choosing an environmental strategy. Along with this the energy efficiency and conservation measures, to reduce the wastage of energy is utmost important. Hence improved electrical energy storage is of paramount importance for widespread integration of solar, wind, and other non-polluting, but intermittent, energy resources into the electrical grid. In order to switch to cleaner energy technologies for transportation, new technologies must be developed to extract and store energy at densities that can compete with petroleum.

As our current electricity system is based primarily on coal-fired power stations, natural gas-fired power stations, and nuclear power plants which cannot be turned on and off at short notice. Hence energy storage can help to balance the electricity grid by storing off-peak generation and using it during peak hours. This helps to reliably incorporate more renewable energy generation into the grid. Energy storage is hence an important part of the move to a Smart Grid [2]. Figure 1.2 explains the need for such a Smart Grid. Smart Grid acts like a reservoir of energy which can store excess energy by taking it from grid at non-peak times and offer this stored energy back to grid at peak times. Smart Grid can operate efficiently only when the energy generated during off-peak hours is stored with minimum losses and available for its use in peak hours. Energy storage is hence an important aspect of Smart Grid.

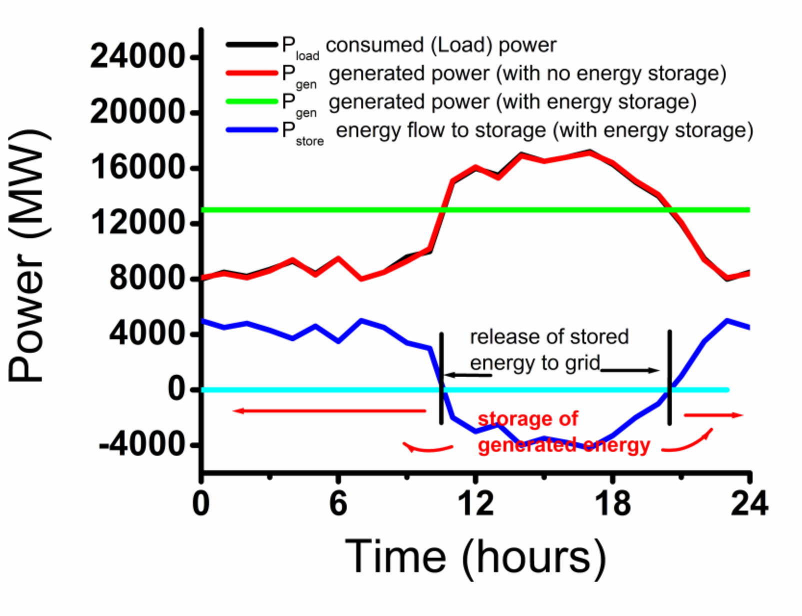

Fig. 1.2 *Simple illustration for efficient use of electrical energy during a day [Ref- en.wikipedia.org]*

In the area of energy storage, nanomaterials especially carbon nanomaterials are of great importance due to many reasons [3]. Incorporating carbon nanostructured electrodes into electrochemical energy conversion and storage devices offers several advantages for a variety of transportation and other green energy infrastructure applications, including batteries, fuel cells, and so-called supercapacitors [4]. In each of these devices, carbon nanostructured materials can be used to increase the surface area of electrodes, where the critical chemical reactions occur within the same volume and mass, thereby increasing the energy density, power density, electrical efficiency, and physical robustness of the system [3]. Such materials also have the potential to lower the manufacturing costs. Of these available energy storage systems, supercapacitors are much favoured among all due to many reasons. Supercapacitors or double-layer capacitor differs from a regular capacitor in the sense that it has a very high capacitance. Other than this a supercapacitor has the high power capability which is nearly comparable with that of conventional capacitor. A supercapacitor stores energy with a static charge which is like that in conventional capacitor, but the major distinction between supercapacitor and a conventional capacitor is that the supercapacitor has large surface area so it can acquire large electric double layer capacitance when charged. Applying a voltage differential on the positive and negative plates charges the capacitor and energy is stored. Supercapacitors can be charge very fast or can store energy very fast and hence avoids the loss of excess energy, although energy density of supercapacitor is lower than batteries. Figure 1.3 shows comparison of energy density and power density of such carbon based or metal oxide based supercapacitors with that of batteries, or fuels like gasoline or hydrogen and conventional capacitors. It can be clear from the figure supercapacitors have higher power density which comparable with that of conventional capacitor but low energy density as compared to batteries. Hence it is important to design supercapacitors with improved energy density which then can compete with batteries. In this regard, there are attempts to develop high energy density supercapacitors which are also called as ultracapacitors. Since last few years, these improved supercapacitors or ultracapacitors are experiencing rapid annual growth rates because they offer extremely high power densities suitable for energy storage in renewable energy applications. Hence these are expected to enhance the commercial viability of renewable energy technologies such as wind and solar power.

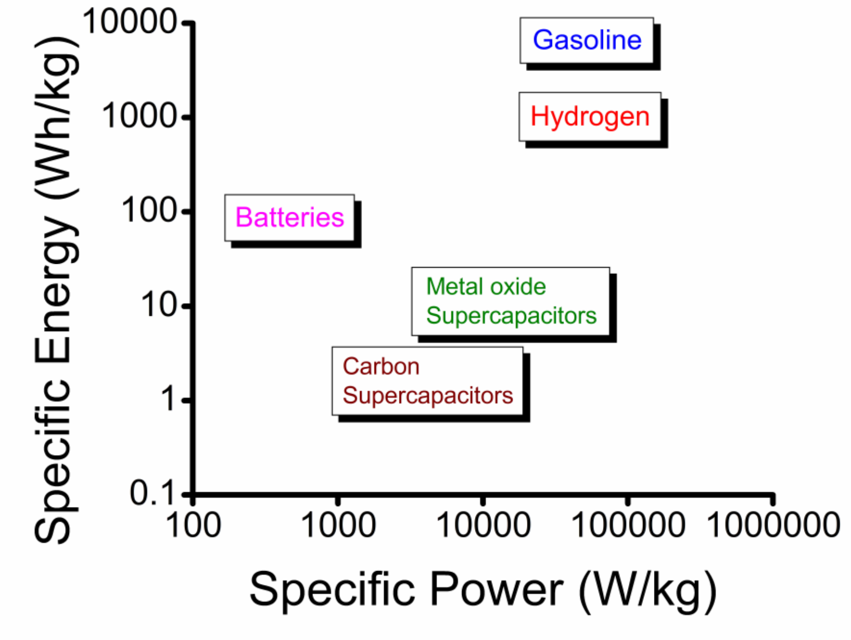

Fig. 1.3 *Comparison of power and energy densities of batteries and supercapacitors as compared to that of natural fuels [Ref- zebu.uoregon.edu]*

As carbon based ultracapacitors are easy to manufacture, the carbon nanomaterials based manufacturing processes can help expand the market for ultracapacitors. Also it is possible to lower manufacturing costs of ultracapacitor while increasing its performance in terms of energy densities and module reliability etc. by altering the material synthesis and design of supercapacitor. Hence it is the need of time to design simple and cost-effective routes for the synthesis of carbon nanomaterials at large scale, to be used for the building next generation supercapacitors/ultracapacitors which can replace batteries, and will be used for efficient energy storage.

1.2 Brief History of Carbon and Carbon Nanomaterials

Carbon was discovered by Antoine Lavoisier in 1772 [5]. He showed that diamonds are a form of carbon. Carl Wilhelm Scheele in 1779 showed that graphite was identical with charcoal and is another form of carbon [6]. There are several allotropes of carbon of which the predominant and naturally occurring are graphite, diamond, and amorphous carbon. The physical as well as chemical properties vary widely with the allotropic form of carbon. For example, diamond is highly transparent and has a very low electrical conductivity, while graphite is opaque and black and has very high conductivity but is anisotropic [5, 6]. Diamond is one of the hardest materials which exist on earth. Hence it can serve as ideal mechanical parts that resist wear and tear during friction [7-9]. On the other hand, graphite is very soft in nature so that it forms a streak on paper. The thermal conductivity of diamond is highest among the all known materials at standard conditions.

Graphite and diamond are most important form of carbon due to there properties and application. Graphite is the most thermodynamically stable form of carbon as compared to other carbon allotropes. The amorphous form is a special form of carbon with arrangement of carbon atoms in a non-crystalline, irregular fashion which has graphitic domains but not in a crystalline macrostructure. It is in the form of powder, and is the main constituent of substances such as charcoal, lampblack (soot) and activated carbon. In graphite, each carbon atom is bonded trigonally to three others in a plain composed of fused hexagonal rings. The resulting 2-dimensional network of carbon is in the form of flat sheets stacked one over other through weak van der Waals forces. Due to weak binding, graphite is soft and its cleaving properties are anisotropic (the sheets slip easily past one another). Graphite conducts electricity through the plane due to delocalization of π electrons, but in vertical i.e. plane perpendicular to graphitic plane there is no or less conductivity [10]. This results in a lower bulk electrical conductivity for graphite than for most metals. Diamond has the cubic structure is the hardest naturally occurring substance in terms of resistance to scratching. In diamond, each carbon atom is bonded tetrahedral to four others. Also diamonds are thermodynamically unstable under normal conditions and transform into graphite. However, due to a high activation energy barrier, the transition of diamond into graphite is extremely slow at room temperature as to be unnoticeable.

As stated previously, diamond and graphite are the crystalline allotropes of carbon which were known to man from 3 to 4 centuries. The nano crystalline forms of carbon are discovered at the end of 20th century due to progress in science and technology. The nanocrystalline forms of carbon consist of carbon nanotubes, fullerenes, carbon fibers, nanodiamond, graphene, carbon nanoscrolls etc. as illustrated in figure 1.4 [11-17]. Since last two decades and with the availability of high-resolution microscopy techniques such as Transmission Electron Microscopy and Scanning Tunneling Microscopy, the research in carbon nonomaterials is progressed. Carbon nanostructures such as fullerenes and carbon nanotubes were discovered around 1990s, while graphene was discovered in early 21st century. Fullerenes have a graphite-like structure, but instead of purely hexagonal packing, they also contain pentagons (or even heptagons) of carbon atoms, which bend the sheet into spheres, ellipses or cylinders.

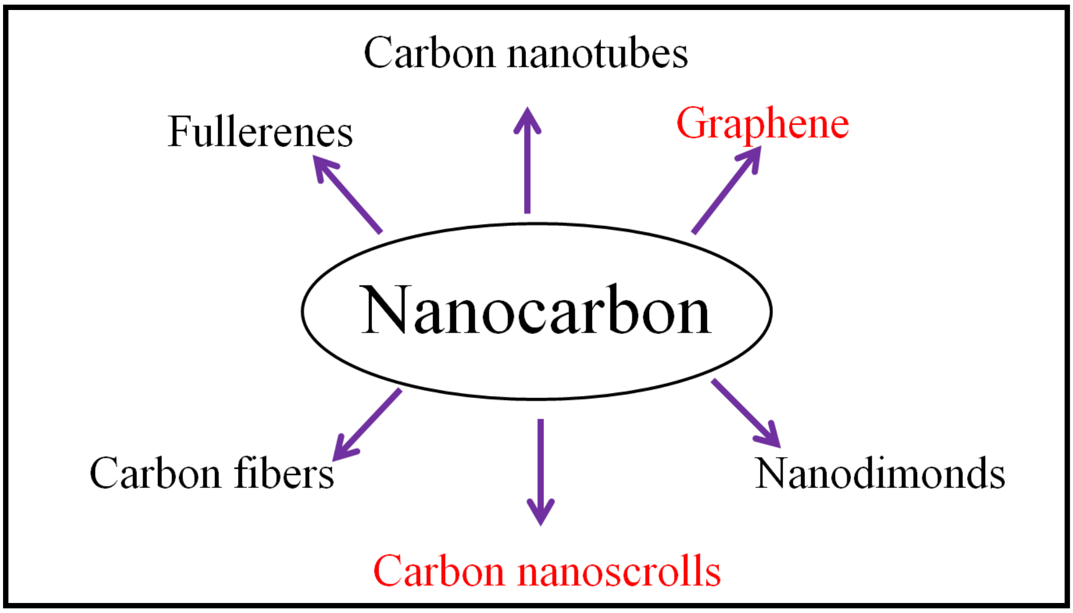

Fig. 1.4 *Types of Carbon nanomaterials*

The names "fullerene" and "buckyball" are coined for these forms of carbon due to the resemblance of structure of fullerenes with that of geodesic domes which was popularized by Richard Buckminster Fuller. The buckyballs are fairly large molecules formed completely of carbon bonded trigonaly; forming spheroids (the best-known and simplest is the soccerball-shaped C60 buckminsterfullerene).Carbon nanotubes are structurally similar to buckyballs, except that each carbon atom in carbon nanotube is bonded trigonally in a curved sheet that forms a hollow cylinder. Carbon nanoscrolls are structurally similar to carbon nanotubes. Topologically carbon nanotubes are co-axial closed cylinders of carbon, while carbon nanoscrolls are open ending rolled sheet of graphene. Carbon nanofibers are cylindrical nanostructures with graphene layers arranged imperfectly as stacked cones, cups or plates while graphene layers wrapped into perfect cylinders are called carbon nanotubes.

1.3 Types of Carbon Nanomaterials

As stated previously there are six major nanomaterials of carbon viz. carbon nanotubes, fullerenes (includes buckyballs, buckytubes), graphene, carbon nanofiber, carbon nanoscroll and nanodiamond.

1.3.1 Carbon nanotubes

Carbon nanotubes (CNTs) are broadly classified as single walled carbon nanotubes (SWCNT) and multi-walled carbon nanotubes (MWCNT). Most single-walled carbon nanotubes (SWCNT) have a diameter of close to 1 nanometer, with a tube length that can be many millions of times longer [18]. Multi-walled carbon nanotubes (MWCNT) consist of multiple rolled layers (concentric tubes) of graphene. There are two models that can be used to describe the structures of multi-walled nanotubes namely Russian Doll model and Swiss roll model [19-21] as illustrated in figure 1.5. In the Russian Doll model, sheets of graphite are arranged in concentric cylinders, like smaller diameter SWCNT within a larger diameter SWCNT. In the Swiss roll or Parchment model, a single sheet of graphite is rolled in around itself, resembling a scroll of parchment or a rolled newspaper. CNTs have very large aspect ratio i.e. length-to-diameter ratio which is significantly larger than for any other material. The interlayer distance in multi-walled nanotubes is close to the distance between graphene layers in graphite, about 3.4 Å. The Russian Doll structure is observed more commonly.

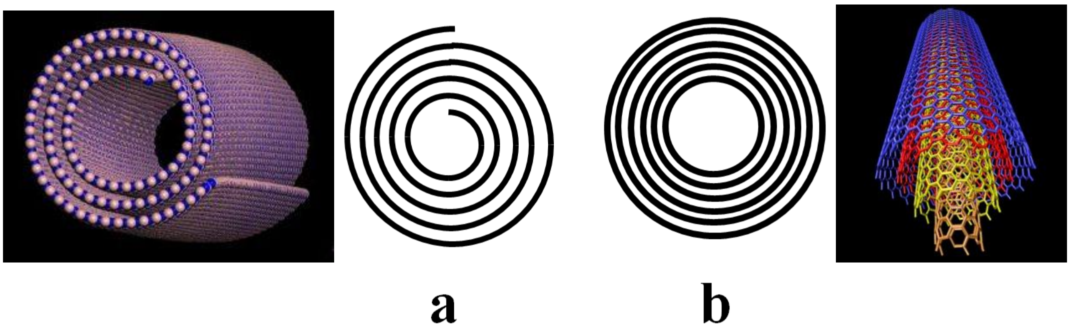

Fig. 1.5 *a) Swiss Roll Model b) Russian Doll Model [Ref-nanotechweb.org, nanotech-now.com]*

CNTs can be metallic, conducting or semiconducting [22]. There is a ballistic electronic transport in metallic SWCNTs and MWCNTs which occurs without scattering over larger lengths owing to their nearly one-dimensional electronic structure. This renders CNTs a property to carry high currents with negligible heating. Also it is reported that the MWCNTs can carry high current densities up to 10^9 to 10^{10} A/cm^2 without any measurable change in their resistance for long time [23]. But distortions like bending and twisting in CNTs affect there electrical and electronic properties. Table 1.1 shows Young's modulus of CNTs which gives the values of tensile strength and density of CNTs [24-26].

Material	Young's modulus (GPa)	Tensile Strength (GPa)	Density (g/cm3)	Thermal Conductivity W/m K	Phonon mean free path Nm
Single wall nanotube	1054.0	150.000	-	~ 2000	~ 100
Multiwall nanotube	1200.0	150.000	2.600		

Table 1.1 *Some physical and electrical properties of carbon nanotubes [Ref-www.nanocyl.com/CNT-Expertise-Centre/Carbon]*

The specific heat and thermal conductivity of CNTs are dominated by phonons as the electronic contribution is negligible due to low density of free charge carriers. The thermal properties along with mechanical properties of CNT are shown in table 1.1.

CNTs also possess unique optoelectronic properties, which find interesting applications in the field of nanotechnology, electronics, optics and materials science. As seen in table 1.1 the mechanical properties of CNTs are very excellent due to which they find applications as additives to various structural materials for e.g. in baseball bats, golf balls, or car parts, where CNTs give the structural stability and at the same time decrease the weight of the objects.

1.3.2 Fullerenes

Fullerenes have graphite-like structure, but without hexagonal packing. They contain hexagons, pentagons (or even heptagons) of carbon atoms, which bend the sheet into spheres, ellipses or cylinders. Fullerenes consist of about 20 hexagonal and nearly 12 pentagonal rings as the basis of icosohedral symmetry closed cage structure [12]. Each carbon atom is sp^2 hybridized and bonded to three other carbon atoms. The C60 molecule has two carbon-carbon bond lengths. The 6:6 ring bonds (between two hexagons) which are also termed as "double bonds" and are shorter than the 6:5 bonds (between a hexagon and a pentagon). The average bond length in fullerene is 0.14 nm. As electron delocalization in C60 molecule is poor, it behave like an electron deficient alkene, and reacts readily with electron rich species. The structural and electronic bonding factors of fullerenes account for the stability of the molecule. According to rules for making icosahedra, an infinite number of fullerenes can exist, dependant on their structure based on pentagonal and hexagonal rings. Figure 1.6 shows the structures of various fullerenes with size variation.

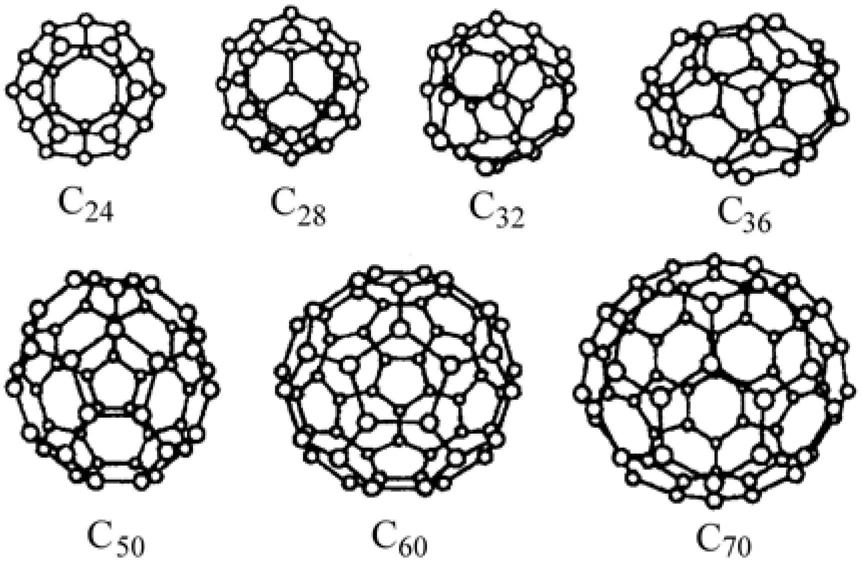

Fig. 1.6 *structure of various fullerenes having size variation [Ref- fulleren.com]*

The properties of fullerenes (split into buckyballs, buckytubes and nanobuds) have not yet been fully analyzed and thus represent an intense area of research in nanomaterials. Physically, buckyballs are extremely strong molecules, able to resist great pressure. However they do not bond each other chemically instead they tend to stick together through much weaker van der Waals forces. This gives buckyballs like graphite, potential as a lubricant. Table 1.2 shows some of the physical properties of Fullerenes. It has been found that Fullerenes take part in various chemical reactions which can be accounted for easy breakage of one of the double bonds in Fullerene [27]. It also serves as strong electron acceptor in presence of strong inorganic donors.

Property	Value	Property	Value
Mass density	1.72 g/cm^3	Band gap (HOMO-LUMO)	1.7 eV
Molecular density	1.44 x 10^{21}/cm^3	Thermal conductivity (300 K)	0.4W/Mk
Bulk modulus	14 GPa	Phonon mean free path	50 Å
Electron affinity (pristine C60)	2.65 eV	Resistivity	10^3 ohms m^{-1}

Table 1.2 *Physical properties of Fullerenes*
[Ref- https://sesres.com/PhysicalProperties.asp]

1.3.3 Graphene

Graphene is a one atom-thick planar sheet of sp2-bonded carbon atoms that are densely packed in a honeycomb crystal lattice. It is the basic structural unit of some carbon allotropes such as graphite, charcoal, carbon nanotubes and fullerenes. The term graphene was coined by Hanns-Peter Boehm in 1962 for describing single-layer carbon foils a combination of prefix from word graphite and the suffix –ene [15, 28, 29]. Graphite is nothing but a stack of plenty of graphene sheets over each other which have interplanar spacing of 0.335 nm. The one atom thick structure of isolated, single-layer graphene was identified by transmission electron microscopy (TEM). This is also called the suspended graphene which showed "rippling" of the flat sheet, with amplitude of about one nanometer. These ripples originate in graphene as a result of the instability of two-dimensional crystals. Graphene due to its structure related properties differ from most conventional three-dimensional materials. Although graphene is a basic building block of graphite, graphene has very interesting properties which are different from graphite. Graphene has some unique physicochemical properties such as excellent electrical and thermal conductivity, high surface area and optical transparency etc. The electrical conductivity of graphene is highest as compared to any other material on earth. Electrons moving in graphene behave as massless Dirac fermions which renders remarkably high electron mobility in graphene at room temperature [29, 30-32]. It is expected that defect free single sheet graphene should possess excellent transport properties and experimentally it is shown that graphene has remarkably high electron mobility at room temperature, with reported values in excess of 150,000 cm^2/Vs [33]. The theoretical resistivity of the graphene sheet is expected to be 10^{-6} Ωcm, which is less than the resistivity of silver, the lowest resistivity substance known at room temperature. However, for graphene on SiO_2 substrates, scattering of electrons by optical phonons of the substrate is a dominant effect than scattering by graphene's own phonons at room temperature [30-34]. This limits the mobility of graphene to 40,000 cm^2/Vs.

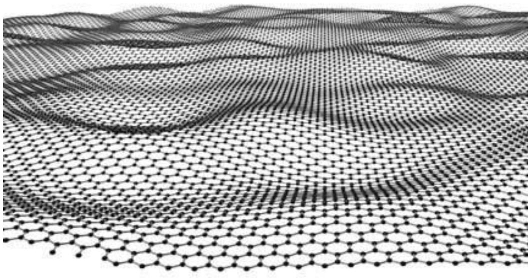

Fig. 1.7 *pictorial representation of single monolayer of graphene sheet [Ref-acrazychicken.blogspot.com]*

Other than this graphene's unique optical properties produce an unexpectedly high transparency. The single atomic monolayer of graphene absorbs ~ 2.3% of white light suggesting graphene to be used as transparent conducting coating [34]. Graphene does not have intrinsic band gap, but it is shown that by applying external electric field the band gap of graphene can be tuned from 0 to 0.25 eV in a dual-gate bilayer graphene field-effect transistor (FET) [35]. Due to small spin-orbit interaction and near absence of nuclear magnetic moments in carbon, graphene can be an ideal material for spintronics. The near-room temperature thermal conductivity of graphene is of the order of 10^3 $Wm^{-1}K^{-1}$ where the thermal conduction is phonon-dominated. [36]

1.3.4 Carbon nanofibers

The first technical records concerning carbon nanofibers is a patent dated 1889 on synthesis of filamentous carbon by Hughes and Chambers. They used a methane/hydrogen gaseous mixture in a gas pyrolysis method where they grew carbon filaments by carbon deposition method [36, 37]. In the early 1950s Soviet scientists Radushkevich and Lukyanovich first observed the electron microscopy images of carbon nanofibers who published a paper in the Soviet Journal of Physical Chemistry showing hollow graphitic carbon fibers that are 50 nanometers in diameter [37, 38]. Conventional carbon fibers are prepared from precursors such as polyacrylonitrile (PAN) and the fibers typically have diameters ranging from 5 to 10 μm. To prepare carbon fibers with diameters in the nanometer range, the method of electrospining followed by pyrolysis of polymer is adapted.

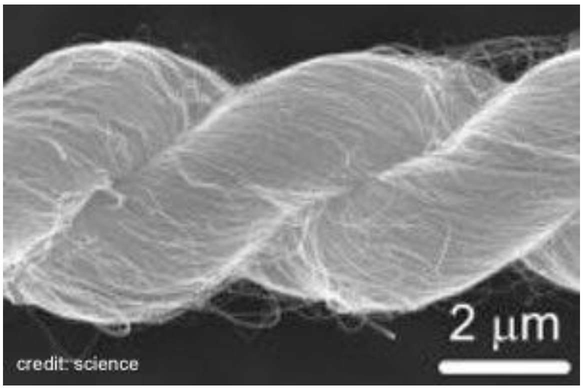

Fig. 1.8 *SEM image of carbon nanofibers [Ref- livescience.com]*

In the recent decade, several research efforts have been attempted to develop carbon nanofibers from electrospun precursors and to explore their potential applications in supercapacitors and batteries [39].

1.3.5 Carbon nanoscrolls

Carbon nanoscrolls (CNS) are open ended rolled sheets of graphene where the interlayer distance between adjacent rolled sheets corresponds to graphitic interlayer spacing. Bacon in 1960 first reported the presence of CNS as scroll whiskers [16, 17]. It is predicted that the properties of CNS are intermediate as compared to that of carbon nanotubes and graphene. Due to pi electron network along the sp^2 carbon sheet, CNS has good electrical conductivity as well as thermal conductivity. CNSs are also predicted to have high surface area. Due to rolled sheet structure, the CNS can undergo volume expansion and this feature is potentially important for a rich variety of applications, especially in energy storage in supercapacitors or batteries [40, 41]. As CNS can be intercalated with lithium ions these are useful in lithium-ion battery as a cathode material. CNS can easily vary the interlayer distance which is very useful for hydrogen storage.

1.3.6 Nanodiamonds

The term nanodiamonds refer to the nanosize diamonds of dimensions less than 100 nm. There are few methods for synthesis of nanodiamonds of which detonation method is the most popular. Detonation nanodiamonds were first synthesized in 1962 by a group of Soviet scientists Yevgeny Zababakhin, including K. V. Volkov, Vyacheslav Danilenko, and V. I. Elina. The detonation nanodiamond grains mostly have diamond cubic lattice and are structurally imperfect [42-45]. Nanodiamonds have a rounded shape, an active surface and a diamond-like hardness that can very useful in a number of applications.

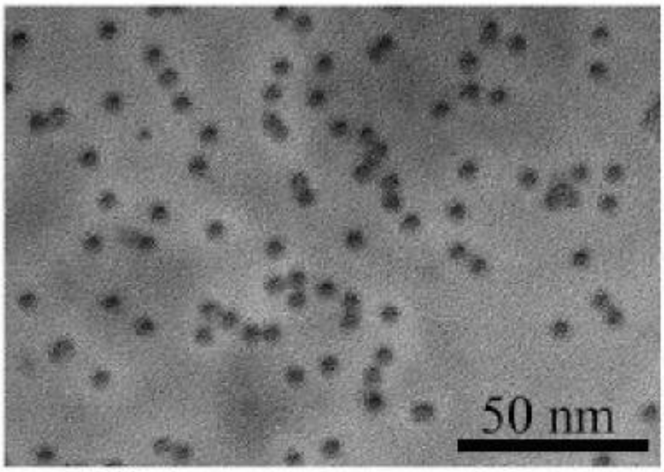

Fig. 1.9 *TEM image of nanodiamonds [Ref- nanotechweb.org]*

Other than this, nanodiamonds also have wear resistance and lubricating power like oils. Nanodiamonds are generally used for angstrom finish while polishing surfaces.

Due to these properties nanodiamonds have been used as polishing material, additives to engine oil, lubricants for metal, fillers for plastics and rubbers etc.

1.4 Metal Oxide-Carbon Composites

In recent decade there is a growing interest in the field of metal oxide-carbon composite, due to the advantages of composite system over carbon or metal oxide alone. The properties of metal oxide-carbon composites depend on both metal oxide and type of carbon material. Among the carbon nanomaterials graphene is the most versatile nano form of carbon due to its wide range of properties. Graphene is hence the favorite choice for making the composite with metal oxide [46-48]. In this regards there have been numerous reports for the metal oxide-graphene composite synthesis, such as with RuO_2, MnO_2, Co_3O_4, Mn_3O_4, ZnO, TiO_2, SnO_2, Fe_3O_4 etc. [46-48]. This opens a new area of materials which can be made applicable for various applications in the fields of energy storage, catalysis, environmental pollution control etc. In the field of energy storage there have been developments for the synthesis of an alternative electrode material for electrochemical capacitors (EC). Along with carbon, many transition metal oxides showed to be suitable as electrode materials for ECs. Apart from energy storage, visible light photocatalysis is also an active area where metal oxide-carbon composites find strong application in environmental pollution control. The reason for the increased interest in the photocatalytic process is the fact that the process is carried out under ambient conditions, and it does not require expensive oxidants and catalyst is inexpensive, nontoxic [46, 47, 49, 50]. In this context, design and development of highly efficient Metal oxide-carbon composite materials which have the potential applications in the degradation of toxic organic molecules and industrial effluents by photocatalysis is of importance.

1.5 Top-Down/Bottom-Up Approaches for Carbon Nanomaterials

There are different methods for synthesis of carbon nanomaterials. There are mainly two approaches for nanostructure syntheses: (a) Top-Down and (b) Bottom-up as shown in Fig. 1.10. Top-down approach mainly involves the processes where carbon nanomaterials like CNTs graphene and carbon nanofibers etc, are generated from bulk carbon material like graphite by Arc-discharge, Laser ablation method. It also includes the physical Scotch method or Chemical exfoliation method by which graphene is obtained from either graphite or from graphite oxide (indirectly from graphite).

Top down approach

Arc-discharge Method

Laser ablation

For graphene

- Physical Scotch tape method
- Chemical exfoliation method

Bottom-up approach

Chemical vapor deposition

Pyrolysis (e.g. of sugar, sodium ethoxide, polymers etc

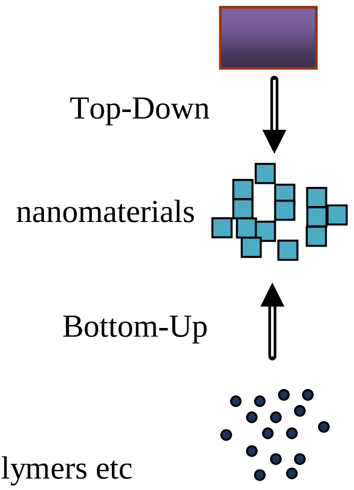

Fig. 1.10 *Different methods for carbon Nanomaterials syntheses*

Bottom-up approach includes chemical vapor deposition and pyrolysis where CNTs, graphene, carbon nanofibers etc. are generated from simple hydrocarbons like sugar, polymers etc.

1.5.1 Arc-discharge Method

Arch-discharge is one of the older methods for synthesis of carbon nanotubes (CNTs) and fullerenes, graphene etc. [11, 51]. Initially C60 fullerenes were synthesized by the carbon arc discharge method, also it is the most common and perhaps easiest way to produce CNTs and very easy to operate. Despite of this advantage this technique produces a complex mixture of components which requires further purification to separate the CNTs from the soot and the residual catalytic metals present in the crude product. The CNTs are synthesized through arc-vaporization of two carbon rods placed end to end, separated by a distance of 1mm, in an enclosure that is usually filled with inert gas at low pressure.

Arc-discharge method is yet another interesting method for growth of CNTs in liquid nitrogen medium. A high current at approximately 20-25 volts is sufficient to create a high temperature discharge between two carbon electrodes. This causes vaporization surface of one of the carbon electrode, which deposits in the form of rod-shaped carbon growth on another electrodes surface.

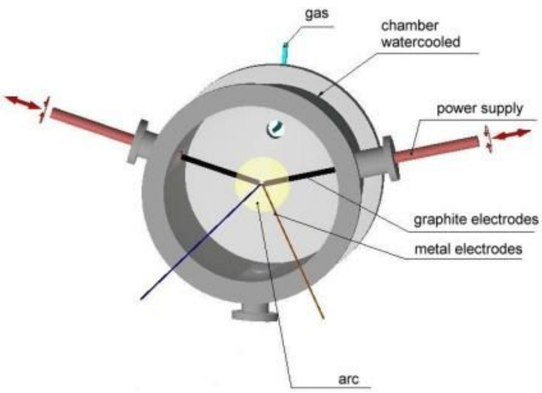

Fig. 1.11 *Schematic of Arc-discharge system [Ref- ifw-dresden.de]*

This growth on the other carbon electrode is then scrapped to obtain CNTs. A high yield of CNTs can be obtained by this method, but it depends on the uniformity of the plasma arc, and the temperature of the deposit forming on the carbon electrode [52].

1.5.2 Laser ablation Method

Laser ablation is also the favorite method for growing CNTs on substrates [53, 54]. Laser ablation involves the removal of material from a solid surface by irradiating it with a laser beam. The material is heated by the absorbed laser energy at lower flux and evaporates or sublimates. Typically at high laser flux, the material is converted to plasma and then deposits on the substrate. The whole process is carried out in a closed chamber maintained at high vacuum or with little percentage of inert gas. Normally the laser is used in continuous pulses, so the laser intensity is usually kept high to carry out laser ablation of material.

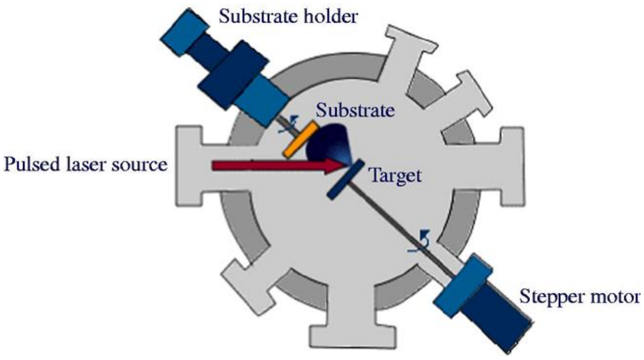

Fig. 1.12 *Schematic of Laser ablation system [Ref- emeraldinsight.com]*

Guo et al. in 1995 were the first to carry out laser ablation of block of graphite and later on graphite mixed with catalytic metal [54]. The catalytic metals such as cobalt, niobium, platinum, nickel and copper etc are responsible for the growth of CNTs from carbon plasma state.

1.5.3 Scotch tape Method

In 2004, Graphene was discovered by Geim group of Manchester, where they obtained graphene by the micro-mechanical cleavage of graphite [15]. Graphite is very soft material in which the interplaner graphitic sheets are hold together by Van-der Walls forces. So the single graphitic plane is easily cleaved by nominal force. The adhesive tape was used to repeatedly split graphite crystals into increasingly thinner pieces. The process is repeated till the optically transparent flake was obtained. The tape with attached optically transparent flakes was dissolved in acetone, and after a few further steps, the flakes including monolayers were sedimented on a silicon wafer. The flakes with monolayers are transferred on TEM grid substrate which then clearly viewed under Transmission Electron Microscope. This method is useful to obtain extremely high quality graphene crystallites.

1.5.4 Chemical exfoliation method

In this method graphite oxide (GO) which is the oxidation product of graphite is chemically reduced to graphene and is also termed as chemically reduced graphite oxide (RGO) [15]. GO is synthesized by Hummer’s method [55]. Briefly graphitic oxide is prepared by stirring powdered flake graphite and sodium nitrate in sulfuric acid. This oxidizes the graphite partially to graphite oxide and separates the sheets of graphite oxide from each other. After cooling and vigorous agitation of the reaction mixture, potassium permanganate is added to it. The reaction mixture is washed several times for removal of impurities, and then treated with peroxide, which turns the solution bright yellow. The suspension is then filtered and after washing the precipitate several times a yellowish-brown filter cake is obtained which is nothing but graphitic oxide residue. This GO is dispersed in D.I. water and then used for preparation of graphene or reduced graphitic oxide (RGO). A known quantity of hydrazine hydrate is added to GO solution and is vigorously stirred for 1 day at about 100^0C with attachment of water condenser. After 1 day a black precipitate of graphene is obtained in the form of suspension which is filtered and washed several times to remove unreacted reagents and impurities. This filtered mass is termed as graphene or RGO.

1.5.5 Chemical vapor deposition

Chemical vapour deposition or CVD is a common technique for depositing a solid material from a gaseous phase. Generally precursor gases (like methane, acetylene etc.) along with carrier gases are delivered into the reaction chamber at ambient temperatures for the growth of carbon on substrate [56]. The nature of gases and the temperature of reaction chamber decide the nature of product. When these gases pass over and come into contact with a heated substrate, react and decompose to deposit solid growth onto the substrate. For CVD method it is important that the precursor must be a gas or a volatile liquid. In this case, the substrate temperature is critical and influences various reactions that take place in reactor.

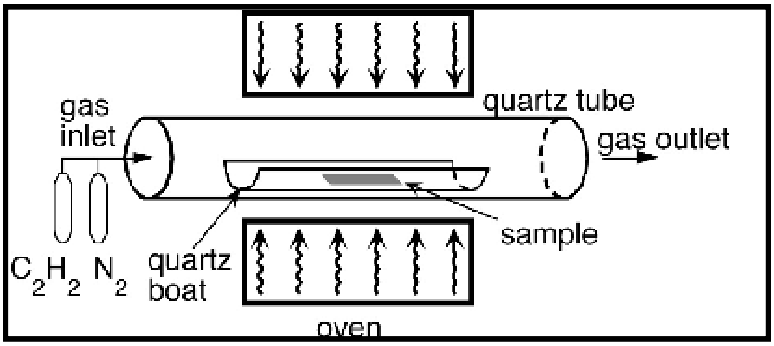

Fig. 1.13 *Schematic of Chemical vapour deposition system*
[Ref- http://ipn2.epfl.ch/CHBU/]

The history of CVD for the synthesis of carbon nanomaterials dates back to nineteenth century. In 1890, French scientists observed the growth of carbon filaments during experiments involving the passage of cyanogens over red-hot porcelain [57]. Since 1950 CVD was used for the growth of carbon filaments and fibers from hydrocarbon precursors in the presence of metal catalyst [58]. Like laser ablation, here also a catalyst is necessary to promote the growth of carbon nanostructures. In 1993 Yacaman et al. for the first time, used the CVD technique to grow MWCNTs from the decomposition of acetylene over iron particles [59]. The MWCNTs are generally produced from acetylene at temperatures typically between 600 – 800°C. As SWNTs have higher energy of formation, the temperature of CVD chamber has to be significantly higher (900 – 1200°C). Also the gases like carbon monoxide or methane must be used because of their increased stability at higher temperatures as compared to acetylene. Apart from carbon fibers and carbon nanotube there is increase in the production of graphene by CVD technique [56, 57]. The growth of graphene is accomplished on copper surface which acts as sacrificial catalyst. Other than copper, nickel can also be served as catalyst for growth of graphene.

1.5.6 Pyrolysis

Pyrolysis is a thermochemical decomposition of organic material at elevated temperatures without the participation of oxygen. Pyrolysis is a special case of thermolysis wherein most common organic materials are thermally decomposed to one or more products. It may also be called as one of the processes involved in charring. In general, pyrolysis of organic substances produces gas and liquid products and leaves a solid residue richer in carbon content, char. Extreme pyrolysis, which leaves mostly carbon as the residue, is called carbonization. Interestingly, the properties of the carbon forms depend on the starting precursors and the synthesis protocol. Generally mesoporous carbon, activated carbon and carbon fibers are mainly synthesized by pyrolysis method. Rayon and polyacrylonitrile (PAN) are used as precursors for most of the commercial carbon fibers, although use of other precursors such as pitch, phenolic resins, and poly (vinylidene fluoride) (PVDF) poly (styrene sulfonate-co-maleic acid) has also been reported [58-62]. PMMA, polystyrenes and certain resins have been used for the synthesis of mesoporus carbon and activated carbon, glassy carbon, carbon fibers and Char etc. [58-65]

1.6 Pyrolysis – A Promising Method for Synthesis of Carbon Nanomaterials

As stated above, pyrolysis is one of the promising method for synthesis of carbon nanomaterials and there composites. In the current work, we have used certain class of polymers’s for pyrolysis to obtain specific carbon nanomaterials. These polymers essentially contain either acrylic acid, or maleic acid or both as the repeating units of polymer. In this respect it is important to state that there has been lot of work especially on the pyrolysis of PAN and some other polymers to synthesize carbon nanofibers, mesoporous carbon and activated carbon etc, [58-65]. Out of these carbon forms only carbon nanofibers have presence of specific size and shape. Along with this the extent of graphitization and ratio of sp^2/sp^3 carbon is highest in carbon nanofibers as compared to mesoporous carbon and activated carbon. In case of carbon fibers, initially the carbon fibers with diameters in the range of several microns were synthesized by simple pyrolysis of PAN. But with the availability of electrospining technique, there have been reports on the synthesis of the polymer fibers with diameter ranging from 50-500 nanometer range from PAN and some other polymers which then successively converted to carbon fibers through pyrolysis [63]. However carbon nanofibers from polymer nanofibers are reported for polyacrylonitrile (PAN), polyimide (PI), poly(vinyl alcohol) (PVA), poly(vinyliden fluoride) (PVDF) and pitch, although so many kinds of polymers have been electrospun. Other than this there are very few reports on the synthesis of other carbon nanomaterials such as graphene by the pyrolysis of polymers [58-62]. In the current work we demonstrate that with suitable choice of polymers and the pyrolysis conditions, graphene and its structural varients can be synthesized by pyrolysis of some selected class of polymers which essentially are polyelectrolytes (salt form of polymer). We also discuss the possible mechanism for the formation of these structures. As polymers are the richest source of carbon, pyrolysis of polymers is an attractive strategy to synthesize novel carbon nanomaterials such as graphene on the large scale.

1.7 Applications of Carbon Nanomaterials and Carbon Composites

In the current work we have investigated the as synthesized carbon nanomaterials and there composites for applications such as energy storage (Supercapacitor electrode material), Field effect transistors (Channel material) and visible light photocatalysis.

1.7.1 Carbon based Supercapacitor

The demand for environmentally friendly, high-performance energy-storage systems is increasing with the rapidly growing market in portable electronic devices, hybrid electric vehicles (HEVs) etc. [64]. Supercapacitors are nothing but electrochemical capacitors which are also known as ultracapacitors, are such devices, which can provide high power capability, long cyclic life (>100,000 cycles), low maintenance, and fast charging discharging [4]. The power density of supercapacitors is many thousand times higher than lithium ion batteries, which hence act complementary to primary energy source like battery which has low power density [65]. The distinction between normal capacitors and supercapacitors is due to their energy density. Normal capacitors have very low surface area hence can store very negligible energy as compared to supercapacitors. Supercapacitors on the other hand due to their high surface area of electrode materials and thin electrolytic dielectrics possesses capacitances several orders of magnitude larger than conventional capacitors [66]. Also supercapacitors are able to attain greater energy densities while maintaining the characteristic high power density of conventional capacitors. Conventional capacitors consist of two conducting electrodes separated by an insulating dielectric material. It consists of electrodes which are normally metal plates and insulator with a high voltage breakdown property.

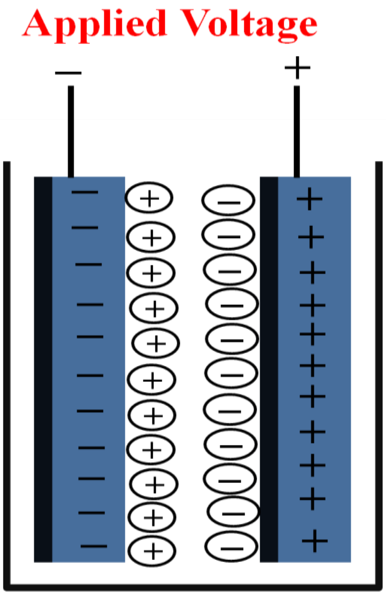

Fig. 1.14 *Schematic showing structure of conventional capacitor*

When a voltage is applied across this capacitor, opposite charges accumulate on the surfaces of each electrode. The charges are kept separate by the dielectric, thus producing an electric field that allows the capacitor to store energy. Capacitance C in this case is defined as the ratio of stored charge Q to the applied voltage V.

$$C = Q / V$$

For a conventional capacitor, C is directly proportional to the surface area A of each electrode and inversely proportional to the distance D between the electrodes.

$$C = \varepsilon_0 \varepsilon_r \frac{A}{d}$$

The constant ε_0 is the dielectric constant (or “permittivity”) of free space and ε_r is the dielectric constant of the insulating material between the electrodes. The dielectric constant of free space is a constant, and dielectric constant of medium is constant for a given material and changes as the material changes. So for a fixed dielectric material the area of electrode and the distance between the electrodes are crucial factors that decides the capacitance of capacitor.

The energy density and the power density are the two main primary attributes of a capacitor. The energy density of a capacitor calculated as an electrical energy stored per unit mass or per unit volume, and the energy (E) stored in a capacitor is directly proportional to its capacitance (C). V is the potential applied to the capacitor through which capacitor is charged from 0 to ‘V’ volt.

$$E = (CV^2)/2$$

Whereas power density P of a capacitor is nothing but the energy expended by capacitor per unit time. In order to have the maximum power density for a capacitor, the internal resistance of capacitor should be minimum to be able to provide sudden burst of charges or electrical energy to an external load. This equivalent series resistance (ESR) accounts for the internal resistive components of the capacitor (e.g., current collectors, electrodes, and dielectric material). The voltage during discharge is determined by these resistances. Hence the maximum power P_{max} for a capacitor is given by-

$$P_{max} = V^2/ (4 \times ESR)$$

In case of conventional capacitors, the ESR can limit the maximum power of that given capacitor. But even though, the conventional capacitors have relatively high power densities and relatively low energy densities when compared to electrochemical batteries and fuel cells. In case of supercapacitors the energy density is very (by several orders of magnitude) high as compared to conventional capacitor and the power density is comparable or lower than that of conventional capacitor. As compared to conventional capacitors, a battery can store more total energy, but it cannot deliver it very quickly, which means its power density is low. Capacitors, on the other hand, store relatively less energy per unit mass or volume, but what electrical energy they do store can be discharged rapidly to produce a lot of power, thus their power density is usually high. Hence capacitors and batteries plays complementary role for storing and delivering the energy when needed.

The principle of working of supercapacitor is same as that of conventional capacitors [65]. However, the supercapacitor incorporates electrodes with much higher surface areas and much thinner dielectrics. This decreases the distance D between the electrodes. As can be seen from above equations, as the area of electrode is increased, with simultaneous decrease in the distance (d) between the electrodes, the capacitance and or energy density (E) also increases. The decrease distance between the electrodes decreases the ESR in supercapacitor; so that they are able to achieve higher power densities. Additionally, supercapacitors have several advantages over electrochemical batteries and fuel cells, including higher power density, shorter charging times, and longer cycle life and shelf life [4]. The performance of a supercapacitor is evaluated from the "Ragone plot" as shown in figure 1.15. It is a plot of energy density vs. power density for a given energy storage device.

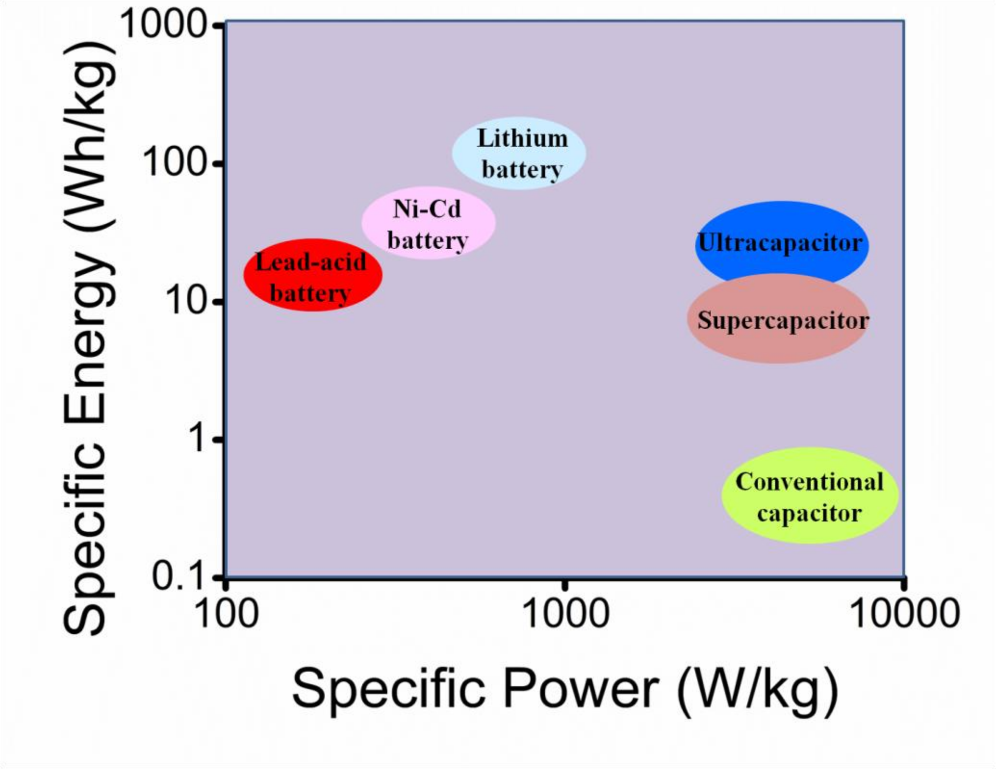

Fig. 1.15 *Ragone plot for comparison of energy and power density of different energy storage devices*

The Ragone plot comparison of various energy storage systems is shown in Figure 3. It is seen from the graph that supercapacitors/ultra capacitors occupy a region between conventional capacitors and batteries [64]. Ultracapacitors are better than supercapacitors in terms of energy density. It is also seen from the graph that the energy density of supercapacitors is much higher than conventional capacitors, but it is still lower than batteries and fuel cells. The energy density of most of the commercially available supercapacitors is less than 10 Whkg^{-1}, which is 10 to 20 times lower than batteries (150-200 Whkg^{-1} in case of lithium ion batteries). As the supercapacitors are having higher power density but lower energy density, there has been a great deal of research effort on increasing the energy storage performance of supercapacitors to be close to or even beyond that of batteries. There are two distinct mechanisms for the energy storage in supercapacitors either by ion adsorption (electrical double layer capacitors, EDLCs) or fast and reversible Faradic reactions (pseudocapacitors). Depending upon the electrode material, the two mechanisms can function simultaneously. In case of EDLCs, a proper control over the pore size and specific surface area of the electrode is crucial for an appropriate electrolyte solution. Normally the carbon electrode is used for EDLC type of supercapacitors [67]. The performance of a supercapacitor in terms of both power delivery rate and energy storage capacity depends upon the properties of both electrode and electrolyte. With carbon as an electrode material, there has been limitation on the increasing energy density beyond some value. The capacitance can be increase further drastically if the presence of foreign electro-active species on the electrode can be coupled with the electrical double layer capacitance. This is then termed as pseudo-capaciter. The electrical double layer (EDL) capacitance arises from pure electrostatic charge accumulation at the electrode-electrolyte interface and the pseudo-capacitance due to fast and reversible surface redox processes at characteristic potentials.

The structure of the supercapacitor is similar to that of a conventional capacitor or battery [68-71]. It consists of two electrodes of porous and conducting carbon material in contact with an electrolyte solution separated by a separator (Fig. 3a). The overall performance of supercapacitor is decided by the components that make up the supercapacitor, including the electrodes, the separator, the current collector, as well as the electrolyte. In case of EDLC type supercapacitor it is only the use of carbon electrode, while pseudocapacitance involves use of active redox species generally an oxide coupled with carbon is used [65].

The pseudo-capacitance involves faradic charging and discharging where a net electron transfer is involved between electrode and electrolyte. Supercapacitors can be divided into groups as Electric double layer capacitor (EDLC), Hybrid capacitor and pseudo-capacitor as shown in figure 1.16.

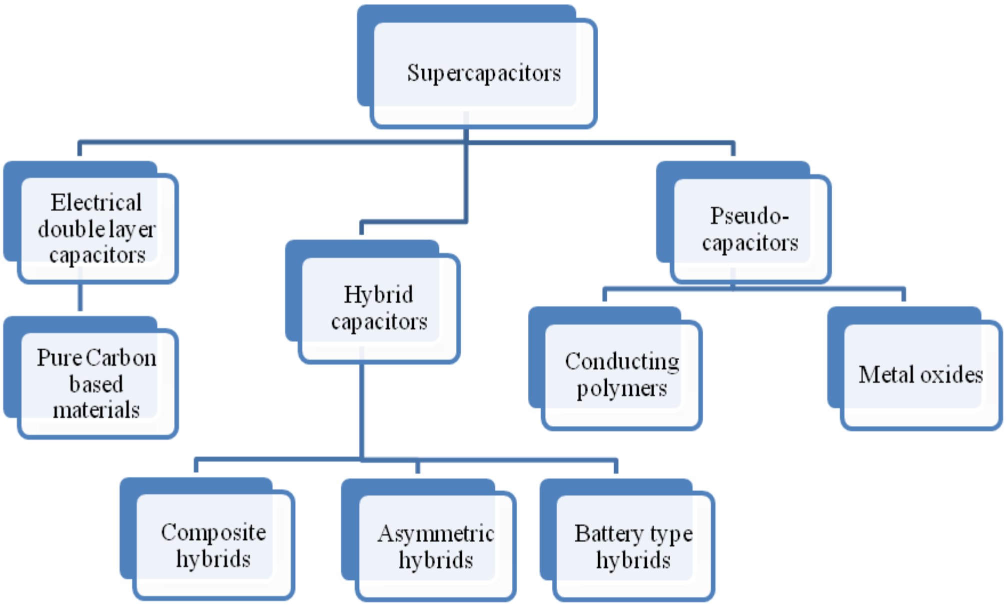

Fig. 1.16 *Taxonomy of supercapacitors*

These groups can be further divided into more subgroup depending upon the type of electrode material. Out of these EDLC types of supercapacitors are studied in the present work.

Electrochemical Double-Layer Capacitors

Electrochemical double-layer capacitors (EDLCs) consist of two carbon-based electrodes in electrical contact with each other by suitable electrolyte, and separated by a porous ion percolative separator. Like convention capacitors EDLCs store charge electrostatically, or non-Faradaically, and there is no transfer of charge between electrode and electrolyte. EDLCs are characterized by formation of electrochemical double-layer of charges to store energy [4, 65]. As the potential is applied across the two electrodes, positive and negative charges accumulate on the opposite electrode surfaces. The ions in the electrolyte solution attract towards the oppositely charged electrode and diffuse across the separator into the pores of the electrode of opposite charge. The potential is not enough to cause the recombination of the charges on the ions with that of oppositely charged electrode. Thus, a double-layer of charge is produced at each electrode. As the surface area of electrodes decides the extent of double-layer formation, the electrodes with higher surface area store more charges, allowing EDLCs to achieve higher energy densities than conventional capacitors [1-3]. As there is no permanent transfer of charge between electrolyte and electrode, there are no chemical or compositional changes associated with non-Faradic processes. This enables charge storage in EDLCs to be highly reversible, with very high cycling stabilities. The typical commercial EDLCs generally operate for many charge-discharge cycles (possibly 10^6 cycles) with stable performance characteristics. Due to their long cycling stability, EDLCs are well suited for applications that involve non-user serviceable locations, such as deep sea or mountain environments. Generally porous carbon materials are often the best choice of the electrode material due to their good electrical conductivity together with the large interface area [64-71].

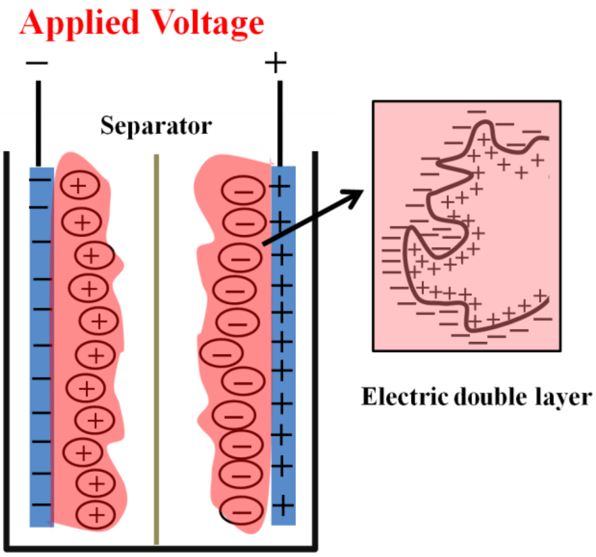

Fig. 1.17 *Schematic diagram showing structure of supercapacitor where is the fig?*

Figure 3b represents the typical EDL structure (known as Stern model) formed on a positively charged porous electrode surface. The specific capacitance C (F/g) for the EDL type of supercapacitor is generally assumed to follow that of a parallel-plate capacitor.

$$C = \varepsilon_0\varepsilon_r \frac{A}{d}$$

Where ε_0 is the dielectric constant (or "permittivity") of free space (Fm^{-1}) and ε_r is the relative permittivity. A (m^2g^{-1}) is the specific surface area of the electrode accessible to the electrolyte ions, and d is the effective thickness of the EDL which is also known as the Debye length).

The performance characteristics of an EDLC can easily be tuned by changing the nature of its electrolyte, for e.g. an EDLC can utilize either an aqueous or organic electrolyte. Generally aqueous electrolytes, such as H_2SO_4 and KOH, which have lower ESR values, are used. These electrolytes require lower minimum pore size requirements compared to organic electrolytes, such as acetonitrile. However, aqueous electrolytes can never be charged above 1 V as they have lower breakdown voltages. Therefore, the choice of aqueous or organic electrolyte depends on the device parameters such as capacitance, ESR, and voltage [64-71]. Due to these reasons the choice of electrolyte often depends on the intended application of the supercapacitor. Along with the nature of electrolyte the subclasses of EDLCs are distinguished primarily by the form of carbon they use as an electrode material. Different forms of carbon materials such activated carbons, carbon aerogels, and carbon nanotubes, graphene etc. can be used to store charge in EDLC type of supercapacitor.

1.7.2 Field Effect Transistor

There is an increasing demand for the low-cost, high-volume manufacturing of flexible transistor-based electronics, such as display drivers, radio frequency identification tags, pressure mapping elements, and chemical sensors etc. Today other than silicon based transistors, organic and polymeric semiconductors based transistors exhibit high on/off ratios in organic field-effect transistors (OFETs). But these OFETs suffer from low mobility's that limit the range of possible applications [72-76]. In this case it is interesting to see that graphene is a new 2D material, which have very high electron mobility can be an ideal candidate for a transistor material with gigahertz or terahertz of working frequency. Although poor on/off ratios of graphene based devices is the major hurdle in the development of FETs made of graphene material. Also in case of OFETs the need for higher mobility organic semiconductors is still compelling, especially for materials used in conjunction with solution processes. The new alternative to this problem involve the use of both organic semiconductor materials together with carbon-based materials such as graphene and carbon nanotubes (CNTs) which exhibit very high mobility [66].

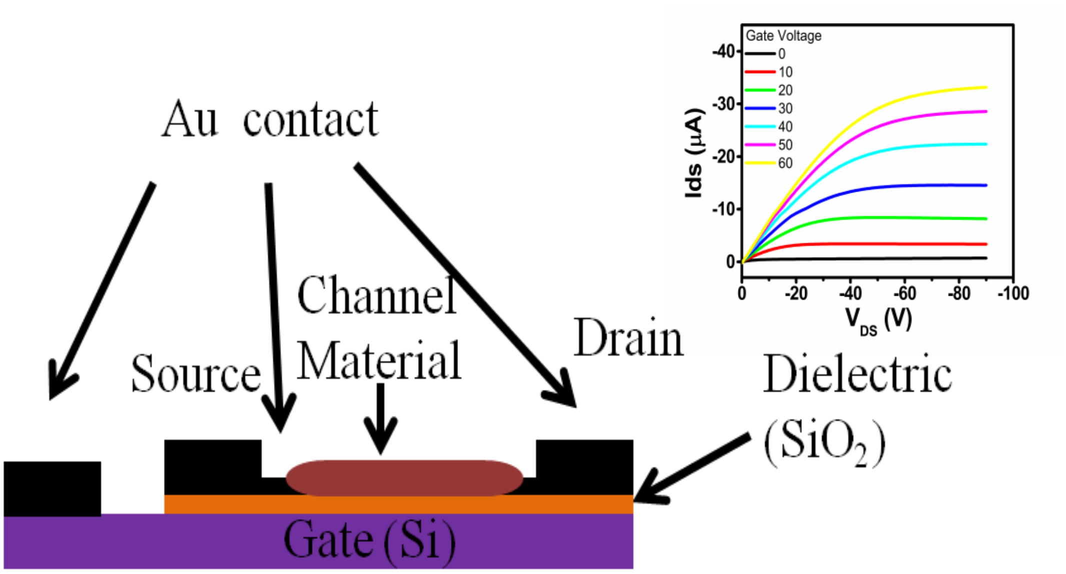

Fig. 1.18 *Schematic showing assembly of field-effect transistor*

Materials like graphene and or CNTs enhance the mobility of FET device while organic semiconductors helps to keep the on/ off ratio sufficiently high [72-74]. In this case there are few reports dealing with organic semiconductor/carbon hybrid field-effect transistors, with a remarkable increase in apparent field-effect mobility resulting from carbon having been inserted into or beneath the semiconductor film. The carbon materials like graphene and or CNTs act as conducting bridges between the crystalline regions of the semiconductor film. However, the on/off ratio appears to decrease just as the mobility begins to increase. As there are very limited reports about these types of FETs, there is a tremendous chance for research in this very recent field.

1.7.3 Visible light Photocatalysis

Energy, Environment and Health are perhaps the most critical and interrelated fields of human concern at the present time. The development of advanced functional materials with novel set of properties is considered the key to address and resolve them. Nanomaterial’s, in particular, are being actively looked at as the most promising ingredients of such functional systems in view of the novel quantum aspects of the phenomena they support and the large surface to volume ratio. The phenomenon of photocatalysis (particularly, visible light photocatalysis) is such field which combine the fields of nanotechnology in an interesting way. It uses photons for generation of excited electrons and holes which can reach the surface quickly in a nanosystem for catalytic action and can be used for elimination of chemical and bio-pollutants from water or air. The basic function of photocatalyst is to separate electron-hole pair by absorbing light. As the more 90% of solar radiation comes in visible region it is hence necessary that the photocatalyst should work in visible region. These separated electron-hole pair then can be utilized for oxidation reduction reaction of harmful pollutant, or can be used for splitting of water. Several studies have been published on photocatalysis. The search for newer and efficient photocatalyst is never ending since the goal of such ideal photocatalyst is to trap and harvest solar energy for splitting of water. The obvious requirement will be the material with low band gap which should absorb the light in visible region. Not only that, but the material should be non-toxic, dispersible in water so as to easily processable into a desired shape. The semiconducting oxide based photocatalyst has been studied in detail to understand the mechanism of photocatalysis in these materials.

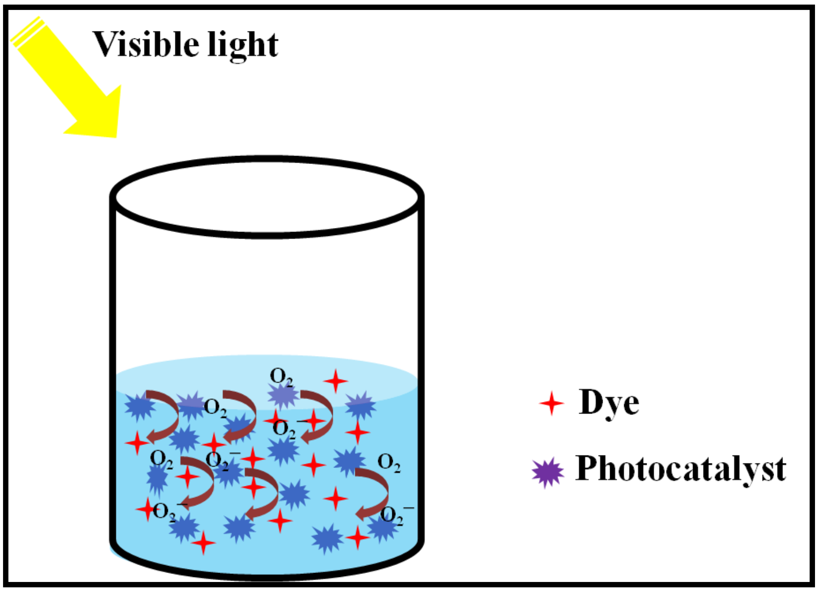

Fig. 1.19 *Schematic showing function of photocatalyst*

Most of the work on visible light photocatalysis is done with the doped metal oxides such as TiO_2, ZnO etc. With the recent discovery of graphene possessing a unique two dimensional layer structure of sp^2-hybridized carbon atoms, there have been many reports for the visible light photocataysis using graphene composites. Due to its unique electronic property for storing and transporting electrons of graphene, it has been shown that graphene incorporated with nanoparticles such as, Au, TiO_2, CdS and Pt display high activity for catalytic applications, including photocatalytic reduction, solar cells, fuel cells, etc [46, 47, 49, 50]. This advance functionality of these hybrids is due to electron transfer from the conduction band of semiconductor to the graphene. Also it is shown that an excited dye can inject electrons to the conduction band of the semiconductor, which can possibly inject electrons to graphene or graphene derivatives because of the higher redox potential of graphene. As graphene possesses excellent electron accepting property, it can be expected that the introduction of graphene into such hybrid system will enhance the catalytic performance of the semiconductor.

1.8 Scope and Objective of the Work

Carbon nanomaterials and there composites have new and novel physico-chemical and electronic properties as compared to their bulk analogs i.e. graphite and diamond. Scientific research in material science for the last decades was dominated by synthesis and property study as well as application oriented study of carbon nanomaterials such as fullerenes, carbon nanotubes, graphene etc. Still today the new routes for the synthesis of these carbon nanomaterials are being investigated due to their importance in material science. My objective seeks the synthesis of graphene and graphene related materials by polymer pyrolysis route. As polymers are richest source of carbon, it is possible to synthesize these carbon nanomaterials on large scale. The aim of study is to synthesize graphene and related variant in single step synthesis protocol, as this will open up the new pathway for the alternate and simple approach towards synthesis of these graphene based nanomaterials. So the objectives of the present thesis are

1. To establish a technique for synthesis of graphene and graphene based materials.
2. To establish a technique for synthesis of metal oxide/carbon composites.
3. To study pyrolysis of various polymers for the synthesis of graphene and graphene based materials.

1.9 Outline of thesis

Chapter 1 discusses the history, importance and fascinating applications of carbon nanotechnology along with the necessary fundamental aspects of it. This is followed by literature survey on synthesis and properties of carbon and carbon nanomaterial with emphasis on graphene and related nanomaterials which is presented with short notes on explored applications of these nanomaterials.

Polymer pyrolysis route for the synthesis of carbon nanomaterials for the current was chosen for study due to simple and catalyst free methodology requires for synthesis of these carbon nanomaterials. The detail synthesis protocol and thorough characterization of these carbon nanomaterials was done by various techniques which are discussed elaborately in chapter II.

3D network of carbon nanoscrolls was synthesized starting from pyrolysis of poly (acrylic acid-co-maleic acid) sodium salt. It is a catalyst-free process where pyrolysis of polymer poly (acrylic acid co maleic acid) sodium salt leads to formation of carbon form and sodium carbonate. Upon water soaking of pyrolysis product, the carbon form undergoes self-assembly to form carbon nanoscrolls. The detail synthesis protocol and opto-electronic properties together with applications of these carbon nanoscrolls has been discuss extensively in section I of chapter III. Along with this work, synthesis of magnetite-graphene oxide (M-GO) composite by pyrolysis of poly (acrylic acid-co-maleic acid) sodium salt with Fe-complex is discussd in section II of the chapter III.

Single-layer-graphene-assembled 3D hexaporous carbon (SLGAPC) was prepared by catalyst free pyrolysis of poly (styrene 4-sulfonate-co-maleic acid) sodium salt. This method represents a facile approach to fabricate 3D graphene-based meso-microporous materials. The process is catalyst/template free and generates hierarchical structure of microporous as well as mesoporous graphene with hexagonal nanopores of uniform size and shape. This SLGAPC have excellent properties together with application in energy storage. These results have been presented in detail in chapter IV.

Large area single sheets of graphene have been synthesized by catalyst free pyrolysis of polymer poly (acrylic acid) sodium salt. It is simple bottom-up process by which large amounts of graphene can be synthesized in single batch requiring no specialized chemicals. The method is scalable and establishes a new and easy approach to fabricate micron size sheets of graphene. Section I of this chapter includes the discussion on detailed synthesis protocol as well as characterization of graphene. Along with this graphene-P3HT hybrid is synthesized starting from the graphene that has been synthesized by pyrolysis of poly (acrylic acid) sodium salt. This composite is then investigated for the use as channel material in field effect transistor. The results of this work are presented in section II of chapter V.

Chapter VI includes the work done on carbon coated ZnO. Water-soluble poly (acrylic acid-co-maleic acid) sodium salt was used to synthesize polymer coated ZnO nanoplates from solution phase reaction. The polymer coated ZnO nanoplates is then annealed in air at 500^0C for 2 hours to obtain carbon coated ZnO nanoroads. The carbon coated ZnO nanoroads gives excellent photocatalytic activity in the visible region. It is also resistant to degradation by and scavenging of the dye without hindrance to charge transfer which is significant for optical applications.

The last chapter VII summarizes the research work and presents future scope of the current studies. In the appendix investigation of hydrated form of sodium carbonate as a ferroelectric material, is presented.

References:

[1] a) L. O. Bengtsson, C. U. Hammer eds., "Geosphere-biosphere Interactions and Climate", *Cambridge University Press*, **2001**, ISBN 0-521-78238-4, 90. b) E. Claussen, V. A. Cochran, D. P. Davis, "Climate Change: Science, Strategies, & Solutions", *University of Michigan*, **2001**, 373. c) A. Allaby, M. Allaby, "A Dictionary of Earth Sciences", *Oxford University Press*, **1999**, ISBN 0-19-280079-5, 244.

[2] http://energy.gov/oe/technology-development/smart-grid, U.S. Department of Energy. "Smart Grid / Department of Energy", **2012**.

[3] C. Liu, Z. Yu, D. Neff, A. Zhamu, B. Z. Jang, *Nano Lett.*, **2010**, *10*, 4863.

[4] L. L. Zhang, R. Zhou, X. S. Zhao, J. Mater. Chem. **2010**, *20*, 5983.

[5] Antoine Lavoisier's original table of elements, taken from theTraité Élémentaire de Chimie, 1789, as quoted in J. R. Partington's A Short History of Chemistry (Dover, 1989, ISBN 0486659771).

[6] Chemical Observations and Experiments on Air and Fire. Uppsala & Leipzig, 1780

[5] A. T. Collins, *Philosophical Transactions of the Royal Society A*, **1993**, *342*, 233.

[6] N. Deprez, D. S. McLachlan, *J. Phys. D: Appl. Phys.* **1988**, *21*, 101.

[7] T. Lierse, M. Kaiser, *Industrial Diamond Review*, **2002**, *4*, 12.

[8] H. K. Tonshoff, H. Hillmann-Apmann H, J. Asche, *Diamond and Related Materials*, **2002**, *11*, 736.

[9] I. P. Hayward, *Surface and Coatings Technology*, **1991**, *49*, 554.

[10] R. Sengupta, M. Bhattacharya, S. Bandyopadhyay, A. K. Bhowmick, *Progress in Polymer Science*, **2011**, *36*, 638.

[11] S. Iijima, *Nature* **1991**, *354*, 56.

[12] H. W. Kroto, J. R. Heath, S. C. O’Brien, R. F. Curl, R. E. Smalley *Nature*, **1985**, *318*, 162.

[13] C. Frondel, U. B. Marvin, *Nature*, **1967**, *214*, 587.

[14] G. Tibbetts, *Journal of Crystal Growth*, **1985**, *73*, 431.

[15] A. Geim, K. Novoselov, *Nature Materials*, **2007**, *6*, 183.

[16] R. Bacon, *J Appl Phys.* **1960**, *31*, 283.

[17] L. Viculis, J. Mack, R. Kaner, *Science*, **2003**, *299*, 1361.

[18] X. Wang, Q. Li, J. Xie, Z. Jin, J. Wang, Y. Li, K. Jiang, S. Fan, *Nano Letters*, **2009**, *9*, 3137.

[19] W. Rulanda, A. K. Schaperb, H. Houa, A. Greinera, *Carbon*, **2003**, *41*, 423.

[20] O. Zhou, R. M. Fleming, D. W. Murphy, C. H. Chen, R. C. Haddon, A. P. Ramirez, *Science*, **1994**, *263*, 1744.

[21] G. Xu, Z. Feng, Z. Popovic, J. Lin, J. J. Vittal, *Adv Mater.*, **2001**, *13*, 264.

[22] X. Lu, Z. Chen, *Chemical Reviews*, **2010**, *105*, 3643.

[23] S. Hong, S. Myung, *Nature Nanotechnology*, **2007**, *2*, 207.

[24] B. Peng, M. Locascio, P. Zapol, S. Li, S. L. Mielke, G. C. Schatz, H. D. Espinosa, *Nature Nanotechnology*, **2008**, *3*, 626.

[25] P. G. Collins, *Scientific American*, **2000**, *5*, 67.

[26] T. Filleter, R. Bernal, S. Li, H. D. Espinosa, *Adv Mater.*, **2011**, *23*, 2855.

[27] M. P. Johansson, J. Jusélius, D. Sundholm, *Angewandte Chemie International Edition*, **2005**, *44*, 1843.

[28] H. P. Boehm, R. Setton, E. Stumpp, *Pure and Applied Chemistry*, **1994**, *66*, 1893.

[29] H. P. Boehm, A. Clauss, G. O. Fischer, U. Hofmann, *Zeitschrift für anorganische und allgemeine Chemie*, **1962**, 316, 119.

[30] J. C. Charlier, P.C. Eklund, J. Zhu, A. C. Ferrari, *Advanced Topics in the Synthesis, Structure, Properties and Applications*, ed. A. Jorio, G. Dresselhaus, M. S. Dresselhaus. Berlin/Heidelberg: Springer-Verlag.

[31] S. V. Morozov, *Phys. Rev. Lett.* **2008**, *100*, 016602.

[32] J. H. Chen, Nature Nanotechnology, **2008**, *3*, 206.

[33] J. H. Chen, *Nature Nanotechnology*, **2008**, *3*, 206.

[33] A. Akturk, N. Goldsman, *Journal of Applied Physics*, **2008**, *103*, 053702.

[34] A. B. Kuzmenko, E. V. Heumen, F. Carbone, D. V. Marel, *Phys Rev Lett.* **2008**, *100*, 117401.

[35] Y. Zhang, *Nature* **2009**, *459*, 820.

[36] A. A. Balandin, S. Ghosh , W. Bao, I. Calizo, D. Teweldebrhan, F. Miao, C. N. Lau, *Nano Lett.*, **2008**, *8*, 902.

[36] T. V. Hughes, C. R. Chambers, Manufacture of Carbon Filaments, *US Patent No. 405*, **1889**, 480.

[37] P. Morgan, Carbon Fibers and Their Composites, *Taylor & Francis Group, CRC Press*, Boca Raton, FL, **2005**.

[38] L. V. Radushkevich, V. M. Lukyanovich, *Zh. Fiz. Khim*. **1952**, *26*, 88.

[39] T. Koyama, M. T. Endo, Processes of Vapor-Grown Carbon Fibers (in Japanese), *O. Buturi*, **1973**, *42*, 690.

[40] G. Mpourmpakis, E. Tylianakis, G. Froudakis, *Nano Lett.* **2007**, *7*, 893.

[41] V. Coluci, S. Braga, R. Baughman, D. Galvao, *Phys. Rev. B*, **2007**, *75*, 125404.

[42] K. Iakoubovskiia, M. V. Baidakovab, B. H. Woutersc, A. Stesmansa, G. J. Adriaenssensa, A.Y. Vul, P. J. Grobet, *Diamond and Related Materials* **2000**, *9*, 861.

[43] K. Iakoubovskii, K. Mitsuishi, K. Furuya, *Nanotechnology*, **2008**, *19*, 155705.

[44] S. Ji, T. Jiangb, K. Xub, S. Li, *Appl. Surf. Sci.* **1998**, *133*, 231.

[45] E. M. Galimov, A. M. Kudin, V. N. Skorobogatskii, V. G. Plotnichenko, O. L. Bondarev, B. G. Zarubin, V. V. Strazdovskii, A. S. Aronin, A. V. Fisenko, I. V. Bykov, A. Y. Barinov, *Doklady Physics*, **2004**, *49*, 150.

[46] L. V. Tian, P. Likun, L. Xinjuan, S. Zhuo, *Catal. Sci. Technol.*, **2012**, *2*, 754.

[47] J. Zhang, Z. Xiong, X. S. Zhao, *J. Mater. Chem.*, **2011**, *21*, 3634.

[48] Z. Li, N. Liu, X. Wang, C. Wang, Y. Qi, L. Yin, *J. Mater. Chem.*, **2012**, *22*, 16640.

[49] Q. Luo, X. Yu, B. Lei, H. Chen, D. Kuang, C. Su, *J. Phys. Chem. C*, **2012**, *116*, 8111.

[50] L. Baojun, H. Cao, *J. Mater. Chem*., **2011**, *21*, 3346.

[51] T. W. Ebbesen, P. M. Ajayan, *Nature*, **1992**, *358*, 220.

[52] M. Wilson, *Nanotechnology: Basic Science and Emerging Technologies*, **2002**.

[53] T. Guo, P. Nikolaev, R. G. Andrew, D. T. David, Colbert, R. E. Smalley, *J. Phys. Chem.* **1995**, *99*, 10694.

[54] T. Guo, P. Nikolaev, A. Thess, D. Colbert, R. E. Smalley, *Chem. Phys. Lett.* **1995**, *243*, 49.

[55] S. William, J. Hummers, R. E. Offeman, *J. American Chemical Society*, **1958**, *80*, 1339.

[56] C. Mattevi, H. Kim, M. Chhowalla, *J. Mater. Chem*., **2011**, *21*, 3324.

[57] M. Kumar, Y. Ando, *Journal of Nanoscience and Nanotechnology*, **2010**, *10*, 3739.

[58] P. Ball, *Nature*, **2001**, 414, 142.

[58] C. T. Nguyena, D. P. Kim, *J. Mater. Chem*. **2011**, *21*, 14226.

[59] M. J. Yacaman, M. M. Yoshida, L. Rendon, J. G. Santiesteban, *Appl. Phys. Lett*., **1993**, *62*, 657.

[59] A. Oya, S. Yoshida, J. Alcaniz-Monge, A. Linares-Solano, *Carbon* **1995**, *33*, 1085.

[60] Y. Yang, A. Centrone, L. Chen, F. Simeon, T. A. Hatton, G. C. Rutledge, *Carbon*, **2011**, *49*, 3395.

[61] J. Yamashita, M. Shioya, T. Kikutani, T. Hashimoto, *Carbon*, **2001**, *39*, 207.

[62] Z. P. Zhou, C. L. Lai, L. F. Zhang, Y. Qian, H. Q. Hou, D. H. Reneker, *Polymer*, **2009**, *50*, 2999.

[63] C. T. Nguyena, D. P. Kim, *J. Mater. Chem*., **2011**, *21*, 14226.

[64] M. J. Hudson, J. W. Peckett, C. S. Sibley, P. J. F. Harris, *Ind. Eng. Chem. Res.*, **2008,** *47,* 2605.

[65] G. M. Jenkins, K. Kawamura, *Polymeric carbonsscarbon fiber, glass and char*; Cambridge University Press, Cambridge, **1976**.

[63] M. Inagaki, Y. Yang, F. Kang, *Adv. Mater.* **2012**, *24*, 2547.

[64] A. Chu, P. Braatz, *Journal of Power Sources*, **2002**, *112*, 236.

[65] L. Chenguang, Y. Zhenning, J. Bor, Z. Z. Aruna, B. Z. Jang, *Nano Letters*, **2010**, *10*, 4863.

[66] M. S. Halper, J. C. Ellenbogen, *Supercapacitors: A Brief Overview*, **2006**.

[67] E. Frackowiak, F. Beguin, *Carbon*, **2001**, *39*, 937.

[68] C. M. Arbizzani, *Journal of Power Sources*, **2001**, *100*, 164.

[69] D. Y. Qu, H. Shi, *Journal of Power Sources*, **1998**, *74*, 99.

[70] J. Gamby, P. L. Taberna, *Journal of Power Sources*, **2001**, *101*, 109.

[71] H. Shi, *Electrochimica Acta.* **1996**, *41*, 1633.

[72] M. S. Fuhrer, B. M. Kim, T. Durkop, T. Brintlinger, *Nano Lett*, **2002**, *2*, 755.

[73] E. S. Snow, J. P. Novak, P. M. Campbell, D. Park, Appl. Phys. Lett. **2003**, *82*, 145.

[74] X. Z. Bo, C. Y. Lee, M. S. Strano, M. Goldfinger, C. Nuckolls, G.B. Blanchet, *Appl. Phys. Lett.* **2005**, *86*, 182102.

[75] X. Z. Bo, N. G. Tassi, C. Y. Lee, M. S. Strano, C. Nuckolls, G. B. Blanchet, *Appl. Phys. Lett.*, **2005**, *87*, 203510.

[76] J. X. Geng, B. S. Kong, S. B. Yang, S. C. Youn, S. Park, T. Joo, H. T. Jung, *Adv. Funct. Mater.*, **2008**, *18*, 2659.

……………………………….

Chapter II

Experimental and Characterizations Techniques

This chapter presents the details of the synthesis protocol used in this research work. Also a discussion on characterization of structural, optical, electrical and magnetic properties of the synthesized products is provided.

2.1 Synthesis Technique

During the past decade, various techniques have been developed for synthesize and characterization of materials with at least one dimension on the nanoscale (nanoparticles, nanolayers, nanotubes etc.) Still, the design and synthesis (or fabrication) of nanoscale materials with controlled properties is a significant challenge in nanoscience and nanotechnology. Nanoscience is still largely in the “discovery phase” wherein new materials are being synthesized on small as well as large scale for testing specific physiochemical properties. The primary focus in this phase is identifying new properties and exploring corresponding applications. The nature of engineered nanomaterials and their proposed uses provides compelling reasons for the implementation of green chemistry in the development of the new materials and applications. The technology is early in development and expected to be widely applied and distributed. These materials are expected to (i) exhibit new size-based properties (both beneficial and detrimental) that are intermediate between molecular and particulate, (ii) incorporate a wide range of elemental and material compositions, including organics, inorganics, and hybrid structures, and (iii) possess a high degree of surface functionality.

Carbon nanomaterials have unique properties and applications. Synthesis of carbon nanomaterials as well as their composites under technologically desirable conditions with controlled size, shape and phase remains a major task for the scientists. Also synthesis of various carbon forms as well as carbon composites is of great importance for the scientists due to applications of these carbon forms and carbon composites in various fields. Pyrolysis is one such method for synthesis of carbon nanomaterials as well as their composites. Pyrolysis is a thermochemical decomposition of organic material at elevated temperatures without the participation of oxygen. Pyrolysis can be tailor to synthesize large amount of carbon nanomaterials.

In the present work we have carried out pyrolysis of polymers to synthesize various carbon nanomaterials and carbon composites. Pyrolysis of polymers is a general route for synthesis of various carbon forms [1-5]. It is the one of the easiest route to synthesize these carbon forms and their composites on large scale. The advantage of pyrolysis is that the design of the process is simple, and also the operation of the process developed or adopted is easy. This process is also easily scalable. Figure

2.1 shows the photo of a split-tube furnace that has been used for the pyrolysis of polymers in the current study.

Fig. 2.1 *Photo of split-tube furnace*

Split-tube furnace can be operated at different temperature with ramp rates from 1^0C/min to 10^0C/min. The pyrolysis process in split tube furnace can be carried out in different atmospheres such as air, argon or nitrogen etc. depending upon the need of experiments.

2.2 Materials

The present research work mainly focuses on the syntheses of carbon forms and their composites by pyrolysis of polymers such as poly (acrylic acid-co-maleic acid) sodium salt (Mol. Wt. 50,000), poly(acrylic acid) sodium salt (Mol. Wt. 5,000) and poly (4-styrene sulfonic acid-co-maleic acid) sodium salt (Mol Wt. 20,000). These polymers are obtained from Sigma-Aldrich and were used as-is in the synthesis protocol. The details of pyrolysis process are explained in the respective chapters. The synthesized forms of carbon were then characterized for their structure and properties using various experimental techniques described in the following section.

2.3 Materials Characterization Techniques

The characterization of a material is very important to ensure the quality and composition of the synthesized material. It is also important to consider that without better resolution, higher sensitivity and greater accuracy of characterization tools, it is difficult to understand the exact nature and properties of the materials. Hence it is necessary to design appropriate technological devices for characterization of materials.

2.3.1 Optical Spectroscopy

Optical Spectroscopy deals with the recording of absorption signals due to electronic transitions from near ultraviolet to near infrared region. In carbon material the extent of oxidation of carbon decides the band gap of concerned material, for example, graphene do not possesses band gap while graphene oxide has considerable band gap (variable and depends upon the extent of oxidation). When the incident photon energy exceeds the band gap energy of the materials like metal oxide and or oxidized carbon like GO, absorption takes place and signal is recorded by the spectrometer. The spectrometer can operate in two modes (i) transmission and (ii) reflection mode. In transmission mode usually materials like carbon and/or colloidal nanoparticles (NPs) which are well-dispersed in solvent are used. The optical measurements for opaque thin films and those NPs and or carbon materials which are not dispersible in solvents are recorded in the diffuse reflectance (DRS) mode.

The light from the source is alternatively split into one of two beams by a chopper; one beam is passed through the sample and the other through the reference. The detector, which is often a photodiode, alternates between measuring the sample beam and the reference beam. Some double beam instruments have two detectors, and the sample and reference beam are measured at the same time.

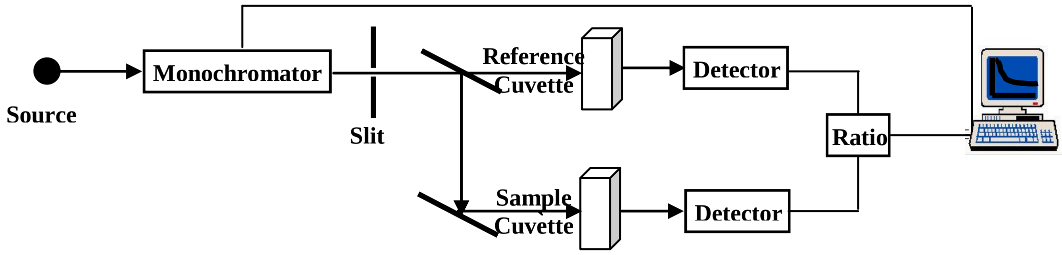

Fig. 2.2: *Schematics of UV-VIS Spectrophotometer in Transmission Mode*

The schematic diagram of UV-VIS Spectrophotometer is shown in figure 2.2. In other instruments, the two beams pass through a beam chopper which blocks one beam at a time.

Broadening of spectral transitions: (a) Doppler Broadening: Random motion of NPs in the liquids and gaseous samples causes their absorption and emission frequencies to show a Doppler shift and hence the spectrum lines are broadened. This effect is more pronounced in liquids than gaseous samples due to significant collisions in solutions. In the case of solids, the motions of the particles are more limited in extent and less random in direction, so that solid phase spectra are often sharp but show evidence of interactions by the splitting of the lines into two or more components. (b) Heisenberg's Uncertainty Principle: If a system exists in an energy state for a limited time 'δt' seconds, then the energy of that state will be uncertain (fuzzy) to an extent 'δE' and is given by $\delta E \times \delta t \approx h/2\pi \approx 10^{-34}$ J.s ,where h = Planck's Constant. Usually life time of excited state is 10^{-8} sec, i.e. 10^{8} Hz, so the uncertainty in the radiation frequency which is, in fact, small as compared to UV-Vis frequency regime ($10^{14} - 10^{16}$ Hz).

Intensity of Spectral lines: There are three main factors that decide the intensity of spectral lines: (i) *Transition probability*: The likelihood of a system in one state changing to another state which is usually governed by quantum mechanical selection rules. (ii) *Population of states*: The number of atoms/molecules initially in the state from which the transition occurs. This is governed by the equation: $N_{upper} / N_{lower} = \exp(-\Delta E/kT)$; Where, $\Delta E = E_{upper} - E_{lower}$, T= temperature (K), k = Boltzman's Constant = 1.38×10^{-23} J/K. (iii) *Concentration and path length*: Clearly since the sample is absorbing energy from a beam of radiation, more the sample-more the beam traverses and more energy will be absorbed from it. Besides the amount of the sample, the concentration of the sample is also deciding factor for the energy absorption. Based on this, Beer-Lambert law, which is often written as:

$$I / I_0 = \exp(-\kappa cl) \quad \text{or} \quad I / I_0 = 10^{-\varepsilon cl} = T$$

Where, κ = constant, for particular spectroscopic transition under consideration.

Where T = transmittance = I / I_0 , ε = molar absorption coefficient.

Inverting above equation and taking logarithms,

$$I_0 / I = 10^{\varepsilon cl} \quad \text{Or} \quad \log (I_0 / I) = \varepsilon cl = A,$$

Where A = absorbance / optical density

Thus, absorbance is directly proportional to the concentration, where the path length and molar extinction coefficient is suppose to be constant for the particular measurement. The source used for the UV and visible light are deuterium and tungsten lamps respectively and the detector used is usually PMT.

In the present study, UV-Vis spectroscopy measurements were carried out on a Jasco UV-Vis spectrophotometer (V570 UV-VIS-NIR) operated at a resolution of 1 nm at National Chemical Laboratory, Pune, INDIA.

2.3.2 Microscopy Techniques

We primarily used Transmission electron Microscope (TEM) and Scanning Electron Microscope (SEM) for microstructural characterization of the carbon materials.

2.3.2a Transmission Electron Microscopy (TEM): TEM is used to investigate the internal structure of micro- and nanomaterials. It works by passing electrons through the sample and using magnetic lenses to focus the image of the structure, much like light is transmitted through materials in conventional light microscopes. Because the wavelength of the electrons is much shorter than that of light, much higher spatial resolution is attainable for TEM images than for a light microscope.

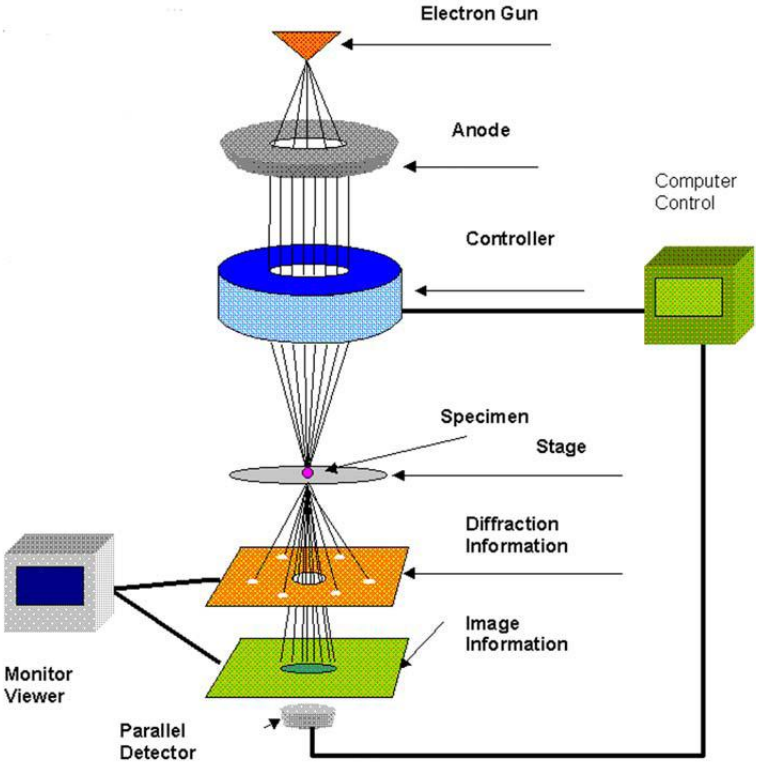

***Fig. 2.3** Schematic diagram of the Transmission Electron Microscope.*
[http://www.rpi.edu/dept/materials/COURSES/NANO/shaw/Page5.html]

The schematic of TEM is shown in figure 2.3. TEM can reveal the finest details of internal structure, in some cases individual atoms. TEM not only produces images but also electron diffraction patterns where high energy electron interacts with the sample which enables to make crystal structure analysis.

2.3.2b Scanning Electron Microscope (SEM): SEM uses a beam of electrons focused to a diameter spot of approximately 1nm in diameter on the surface of the specimen and scanned back and forth across the surface. The surface topography of a specimen is revealed either by the reflected (backscattered) electrons generated or by electrons ejected from the specimen as the incident electrons decelerate secondary electrons. A visual image, corresponding to the signal produced by the interaction between the beam spot and the specimen at each point along each scan line, is simultaneously built up on the face of a cathode ray tube similar to the way that a television picture is generated.

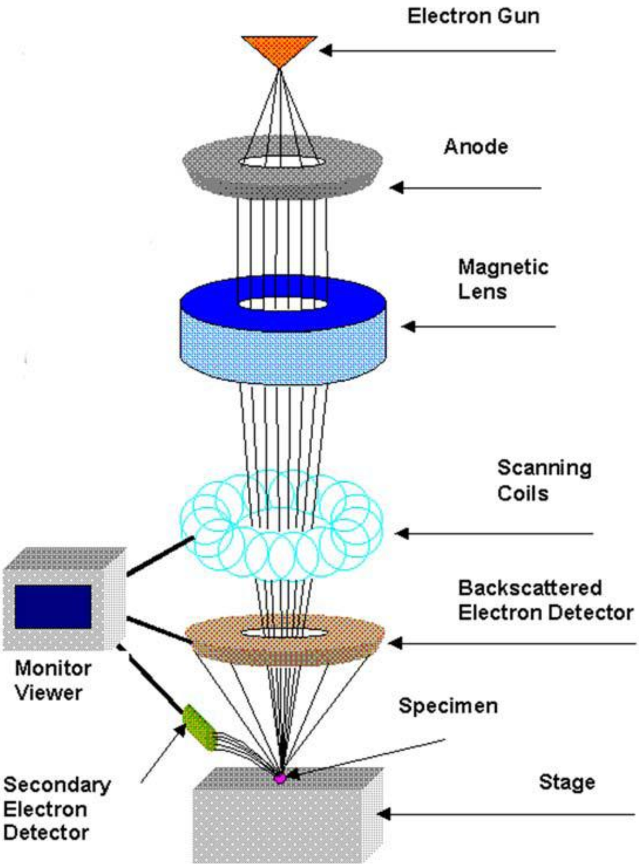

Fig. 2.4 *Schematic diagram of the Scanning Electron Microscope.* *[http://www.rpi.edu/dept/materials/COURSES/NANO/shaw/Page5.html]*

The best spatial resolution currently achieved is of the order of 1nm. Figure 2.4 shows the schematic diagram of Scanning Electron Microscope. In the present work, the TEM and SEM images for the carbon and carbon composites samples were recorded on instrument (IFEI, Techni F30 FEG with 300 kV for TEM and FEI quanta 200 for SEM) at National Chemical Laboratory, Pune.

2.3.3 Powder X-Ray Diffraction

X-ray diffraction (XRD) technique is used to realize structural properties of materials and obtain information about crystal structure/phase, lattice parameters, crystallite size, orientation of single crystals, preferred orientation of polycrystals, defects, strains and so on [6-8]. This technique is suitable for thin films, bulk and nanomaterials. In case of nanostructures, the change in lattice parameter w. r. t. bulk gives idea of nature of strain present in the material.

In XRD, a collimated monochromatic beam of X-rays is incident on the sample for diffraction to occur. A constructive interference occurs only for certain θ*'s* correlating to those (hkl) plane, where path difference is an integral multiple (n) of wavelength. Based on this, the Bragg's condition is given by

$$2d\sin\theta = n\lambda$$

Where, λ is the wavelength of the incident X-ray, d is the interplaner distance, 'θ' is the scattering angle and n is an integer called order of diffraction. In nanostructures, X-rays are diffracted by the oriented crystallites at a particular angle to satisfy the Bragg's condition. Having known the value of θ and λ, one can calculate the interplaner spacing. The XRD can be taken in various modes such as θ-2θ scan mode, θ-2θ rocking curve, and ϕ scan. In the θ-2θ scan mode, a monochromatic beam of X-ray is incident on the sample at an angle of θ with the sample surface. The detector motion is coupled with the X-ray source in such a way that it always makes an angle 2θ with the incident direction of the X-ray beam (Fig. 2.4). The resulting spectrum is a plot between the intensity recorded by the detector versus 2θ. Schematic view of XRD is shown in Fig. 2.5.

The incident X-rays may reflect in many directions but will only be measured at one location so we will require:

$$\text{Angle of Incidence } (\theta_i) = \text{Angle of Reflectance } (\theta_r)$$

This is done by moving the detector twice as fast in (θ) as the source. So, only where $\theta_i = \theta_r$, will be the intensity of the reflected X-rays to be measured.

Nanomaterials have smaller sized crystallites and significant strains due to surface effects, causing considerable peak broadening and shifts in the peak positions w.r.t standard data. From the shifts in the peak positions, one can calculate the change in the d-spacing, which is the result of change of lattice constants under strain. The crystallite size (D) is calculated using Scherrer's formula:

$$D = k\,\lambda / \beta \cos\theta$$

Where, k = Scherrer's Constant ≈ 0.9, β = Full Width at Half Maximum (FWHM).

Only disadvantage of XRD is its less sensitivity towards low-Z materials, thus usually high-Z materials are used. In such cases, electron or neutron diffraction is employed to overcome the low intensity of diffracted X-rays. Figure 2.4 shows the representation of X-ray Diffraction.

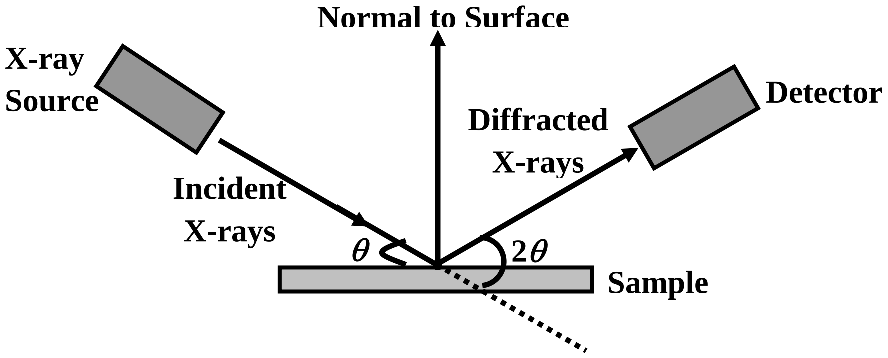

Fig. 2.5 *Representation of X-ray Diffraction. The* θ*-*2θ *scan maintains these angles with the sample, detector and X-ray source. Only planes of atoms that share this normal will be seen in the* θ*-*2θ *scan.*

In the present work, the XRD pattern for the carbon and carbon composites samples were recorded at National Chemical Laboratory, Pune using Pananlytical Philips X'Pert PRO powder diffractometer. In all the cases the radiation source was Cu-K_α (λ = 1.542 Å).

2.3.4 Fourier Transform Infrared Spectroscopy

Infrared spectrum appears only when the vibrations amongst bonded atoms produces a change in the permanent electric dipole moment of the molecule/solid. It is reasonable to suppose that the more polar a bond, the more intense will be IR spectrum arising from the vibrations of that bond. IR spectrophotometer consists of mainly source, monochromator and detector [9, 10]. The source is in some form of filament (e.g. Nernst Filament, made of a spindle of rare earth oxides or globar filament, made of carborundum rod) which is maintained at red- or white-heat by an electric current. The monochromator guides IR beam and focuses to the sample. The detectors are based on either temperature (bolometer/thermometer) or conductivity rise at given frequency (PbS).

Fourier Transform IR Spectroscopy: FTIR has considerably speeded and improved the spectroscopy in the IR region in general and in particular far IR region i.e. below 400 cm^{-1} where good deals of useful molecular information is contained, is usually called as ‘Energy Limited’ region, where sources become weak and detectors insensitive, resulting poor signal to noise ratio.

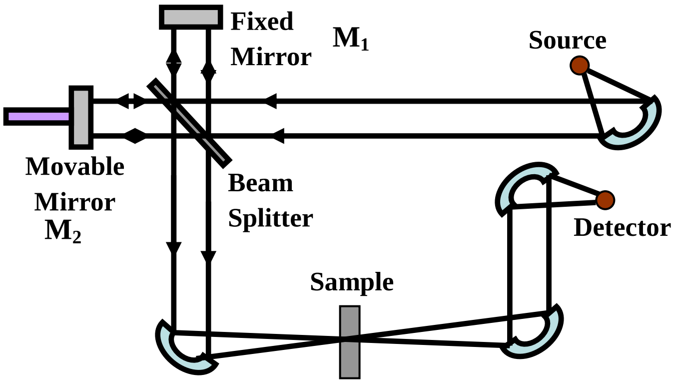

Fig. 2.6 *Schematic of FTIR Spectrophotometer*

Figure 2.6 shows the schematic of FTIR spectrophotometer. The apparatus derives from the classical attempt by Michelson to measure the ‘ether wind’ by determining the velocity of light in two perpendicular directions. A parallel beam of radiation is directed from the source to the interferometer, consisting of the beam splitter B and two mirrors, M_1 and M_2. The beam splitter is a plate of suitably transparent material (e.g. KBr) so as to reflect just 50% of the radiation falling on it. Thus half the radiation goes to M_1, and half to M_2, returns from both these mirrors along the same path, and is then recombined to a single beam at the beam splitter (clearly half the total radiation is sent back to the source, but this is immaterial). It is well known (and the essence of the Michelson experiment) that if monochromatic radiation emitted by the source, the recombined beam leaving B shows constructive or destructive interference, depending on the relative path lengths B to M_1 and B to M_2. Thus if the path lengths are identical or differ by integral multiple of wavelengths, constructive interference gives bright beam leaving B, whereas if the difference is a half integral number of wavelengths, the beam cancels at B. As the mirror M_2 is moved smoothly away or towards from B, therefore, a detector sees radiation alternating in intensity. It is fairly easy to imagine that if the source emits two separate monochromatic frequencies, υ_1 and υ_2 then interference pattern of υ_1 and υ_2 would overlay the interference caused by M_1 and M_2; the detector would see a more complicated intensity fluctuation as M_2 is moved, but computing the Fourier transform of the resultant signal is very rapid way of obtaining the original frequencies and intensities emitted by the source. Taking the process further, even white radiations emitted by the source produces an interference pattern which can be transformed back to the original frequency distribution.

The production of a spectrum is a two-stage process: (a) Without a sample in a beam, mirror M_2 is moved smoothly over period of time (say one second) through a distance of about 1 cm, while the detector signal – the interferogram – is collected into multi-channel computer; the computer carries out the Fourier transformation of the stored data to produce background spectrum. (b) A sample interferogram is recorded in exactly the same way, Fourier transformed, and then ratioed against the background spectrum for plotting as transmittance spectrum. Alternatively, the sample and background spectra may each be calculated in absorbance forms and the latter simply subtracted from the former to give an absorbance spectrum of the sample alone. The advantage of using FTIR is that the whole spectrum is obtained across the entire frequency range at once with constant resolving power over entire range.

Powdered samples were mixed with the standard KBr powder. The FTIR measurements of these samples were carried out on a Perkin Elmer Spectrum One FTIR spectrometer operated in the diffuse reflectance mode at a resolution of 4 cm^{-1} at National Chemical Laboratory, Pune, INDIA.

2.3.5 Raman Spectroscopy

When a beam of visible light is passed through a transparent substance, a small amount of the radiation energy is scattered, the scattering persisting even if all other extraneous matter are rigorously excluded from the substance. If monochromatic radiation is used, if the scattered energy will consist almost entirely of radiation of the incident frequency then it is so-called *Rayleigh scattering* but, in addition, certain discrete frequencies above and below that of the incident beam will be scattered, it is referred to as *Raman scattering* [9].

According to quantum theory of radiation, when photons having energy ‘hυ’ undergo collisions with molecules and, if the collision is perfectly elastic, they will be deflected unchanged. A detector placed to collect energy at right angles to an incident beam will thus receive photons of energy ‘hυ’, i.e. radiation of frequency ‘υ’. However, it may happen that energy is exchanged between photon and molecule during the collision: such collisions are ‘inelastic’. The molecule can gain or lose amounts of energy only in accordance with the quantum laws; i.e. its energy change, ΔE joules, must be the difference in energy between two of its allowed states. That is to say, ΔE must represent a change in the vibrational and/or rotational energy of the molecule. If the molecule gains energy ΔE, the photon will be scattered with the energy hυ- ΔE and the equivalent radiation will have a frequency υ- ΔE/h. Conversely, if the molecule loses energy ΔE, the scattered frequency will be υ+ ΔE/h. Radiations scattered with a frequency lower than that of the incident beam is referred to as Stokes’ radiation, while that at higher frequency is called anti-stokes’ radiation. Since the former is accompanied by an increases in molecular energy (which can always occur, subject to certain selection rules) while the latter involves a decrease (which can only occur when the molecule is originally in an excited vibrational/rotational state). Stokes’ radiation is generally more intense than anti-Stokes’ radiation.

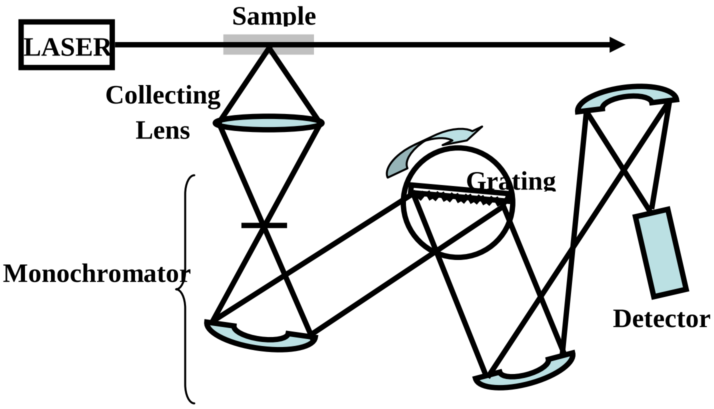

Fig. 2.7 *Schematic of Raman Spectrometer* [7]

Figure 2.7 shows the schematic of Raman spectrometer. Raman Spectrometer consists of Laser beam (very narrow, monochromatic, coherent and powerful) which when passed through the cell, usually a narrow glass or quartz tube filled with the sample, light get scattered sideways from the sample, which is collected by a lens and passed into a grating monochromator. The signal is measured by a sensitive PMT and after amplification; it is usually processed by a computer which plots the Raman spectrum. Raman spectroscopy measurements were done on instrument (Confocal micro-Raman spectrometer LabRAM ARAMIS Horiba Jobin-Yvon apparatus with laser excitation wavelength of 532 nm) in France.

2.3.6 Photoluminescence Spectroscopy

Photoluminescence (PL) is the spontaneous emission of light from a material under optical excitation. The appropriate excitation energy and intensity is required to choose to probe the sample’s discrete electronic states accurately. When light of sufficient energy is incident on a material, photons are absorbed, material got excited and electronic transitions occurred. Eventually, these excitations relax and the electrons return to the ground state. If radiative relaxation occurs, the emitted light is called PL [11]. This light can be collected and analyzed to yield a wealth of information about the photo-excited material. The PL spectrum provides the transition energies, which can be used to determine electronic energy levels, defects and impurity states in the sample. The PL intensity gives a measure of the relative rates of radiative and non-radiative recombination.

PL is divided into two categories, fluorescence and phosphorescence, depending upon the electronic configuration of the excited state and the emission pathway. Fluorescence is the property of some atoms and molecules to absorb light at a particular wavelength and to subsequently emit light of longer wavelength after a brief interval, termed the fluorescence lifetime. The process of phosphorescence occurs in a manner similar to fluorescence, but with a much longer excited state lifetime.

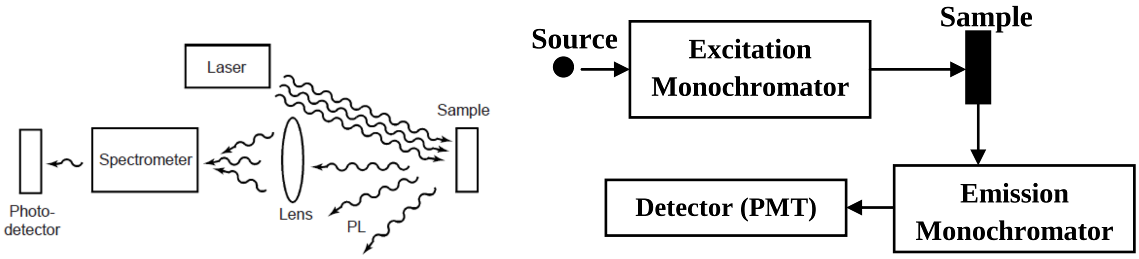

Fig. 2.8 *Fig. at left side shows: Schematic of PL process while Fig. at right side shows: Schematic Layout of PL Set-up*

Figure 2.8 shows the schematic of PL process as well as schematic layout of PL Set-up. PL is simple, versatile, and nondestructive measurement technique. The PL signal itself is characterized by two essential features: peak energy and intensity. The excitation energy and optical intensity can be chosen properly in order to yield more accurate information on the energy levels available to electrons in the material. The PL signal often depends on the density of photo-excited electrons and the intensity of the incident beam. The intensity of the PL signal depends on the rate of radiative and non-radiative events, which depends in turn on the density of nonradiative interface states. Usually, defects and impurities break the periodicity of the lattice and perturb the band structure locally. This perturbation is attributed to the discrete energy levels lying within the band gap. Depending on the defect or impurity, the state acts as a donor or acceptor of electrons in the lattice. Surfaces and interfaces contain a high concentration of impurity or defect states. Dangling bonds at a semiconductor surface or defects give rise to electronic states within the bandgap. These mid-gap states fill up to the Fermi level with electrons that originate in the bulk of the material. The fundamental limitation of PL analysis is its reliance on radiative events. Materials with poor radiative efficiency, such as low-quality indirect bandgap semiconductors, are difficult to study via ordinary PL.

The PL measurements of nanopowders and NPs dispersed in solvent were done using LS 55 spectrophotometer at National Chemical Laboratory, Pune, INDIA.

2.3.7 X-Ray Photoelectron Spectroscopy

X-ray photoelectron Spectroscopy (XPS) probes the binding energies of core electrons in an atom. Although such electrons play little part in chemical bonding, different chemical environments can induce small changes in their binding energies; this is because the formation of bonds; changes the distribution of electrons in the system and hence, by modifying nuclear shielding, produces changes in the effective nuclear charge of the bound atoms [7]. Thus, XPS involves the analysis of emitted electrons from a material as a result of incident X-rays, is also rarely called as electron spectroscopy for chemical analysis (ESCA). Only the photoelectrons from atoms near the surface escape, typically from top 2-5 nm. The actual depth varies with the materials and electron energy. A typical sampling area is 1 cm^2. This technique mainly gives information about the elemental composition of the surface of the materials and the information about the chemical state of elements. It is one of the most employed surface analysis techniques. This is usually performed using X-rays (typically from Al or Mg) to excite photoelectrons from the core levels of atoms in a specimen.

Photoelectron spectroscopy is an excellent technique for probing atomic and molecular electronic energy levels. Figure 2.9 shows the schematic for principle of photo-electron spectroscopy as well as Schematic of XPS instrument. When an atom or molecule is subjected to higher energy radiations, photons in the radiations colloid with and eject electrons from atoms, leaving behind ions. Ejected electrons depart with different velocities and photoelectron spectroscopy measures the velocity distribution of the released electrons. Each electron is held in place by nucleus with a characteristic binding energy.

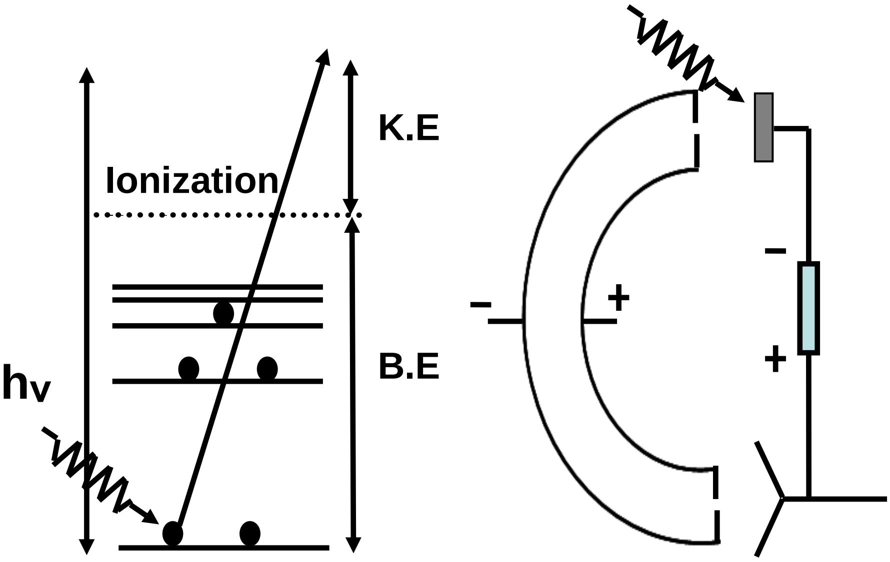

Fig. 2.9 *(A) Principle of Photo-electron spectroscopy, (B) Schematic of XPS* [7]

The energy of the photon is imparted to the electron and, if this energy is greater than the B.E., the electron will leave the atom and carry with it an excess energy – thus it will have certain K.E. (and velocity). Clearly the total energy must conserve:

hυ = binding energy + Work Function + kinetic energy

Binding Energy = hυ – Kinetic Energy

Provided we know the energy of the exciting monochromatic radiations, we can measure the binding energies of electrons in the atom under examination by observing the kinetic energies with which they leave.

Main components of XPS are (i) X-ray source, (ii) Sample holder, (iii) electron energy analyzer. The (ii) and (iii) component must be in UHV. The X-ray source is a simple X-ray tube with double anodes (typically Al and Mg) incident radiation energy can be switched from one to the other. In both, XPS, the kinetic energy of the ejected electrons is measured using a hemispherical analyzer. Monochromatic X-ray or UV radiation falls on the sample and ejected electrons pass between a pair of electrically charged hemispherical plates which act as an energy filter, allowing electrons of only a particular kinetic energy to pass through – the pass energy, E_{pass}. The resulting electron current, measured by an electron multiplier, indicates the number of electrons ejected from the surface with that kinetic energy. E_{pass} can be systematically varied by changing the retarding voltage (V_R) applied to the analyzer. XPS measurements of different samples were carried out on a VG MicroTech ESCA 3000 instrument at Center for Materials Characterizations (CMC), National Chemical Laboratory, Pune. The core level binding energies (BE) were corrected with the carbon binding energy of 285 eV.

2.3.8 Bet Surface Area Measurement

The specific surface area of a material can be analyzed by BET surface area analyzer. The BET theory accounts for the physical adsorption of gas molecules on a solid surface and thereby serves as an important analysis technique for the measurement of the specific surface area of a material [12]. In 1938, Stephen Brunauer, Paul Hugh Emmett, and Edward Teller published an article about the BET theory. The word “BET” consists of the first initials of their family names. The concept of the theory is an extension of the Langmuir theory, which is a theory for monolayer molecular adsorption, to multilayer adsorption with the following hypotheses: (a) gas molecules physically adsorb on a solid in layers infinitely; (b) there is no interaction between each adsorption layer; and (c) the Langmuir theory can be applied to each layer. The resulting BET equation is expressed by following equation

$$\frac{1}{v\left[(P_0/P)-1\right]} = \frac{c-1}{v_m c}\left(\frac{P}{P_0}\right) + \frac{1}{v_m c}$$

Where P and P0 are the equilibrium and the saturation pressure of adsorbates at the temperature of adsorption, v is the adsorbed gas quantity (for example, in volume units), v_m is the monolayer adsorbed gas quantity and c is the BET constant, which is expressed by following equation.

$$c = \exp\left(\frac{E_1 - E_L}{RT}\right)$$

E_1 is the heat of adsorption for the first layer, and E_L is that for the second and higher layers and is equal to the heat of liquefaction. Equation (1) is an adsorption isotherm and can be plotted as a straight line with $1 / v[(P0 / P) - 1]$ on the y-axis and $\phi = P / P0$ on the x-axis according to experimental results. This plot is called a BET plot. The linear relationship of this equation is maintained only in the range of $0.05 < P / P0 < 0.35$. The value of the slope (A) and the y-intercept (I) of the line are used to calculate the monolayer adsorbed gas quantity v_m and the BET constant c. The following equations can be used.

$$v_m = \frac{1}{A + I} \qquad c = 1 + \frac{A}{I}$$

Total surface area S_{total} and a specific surface area (S) are evaluated by the following equations, where v_m is in units of volume which are also the units of the molar volume of the adsorbate gas, N is Avogadro's number, s is adsorption cross section of the adsorbing species, V is molar volume of adsorbate gas and a is mass of adsorbent (in g)

$$S_{BET,total} = \frac{(v_m N s)}{V} \qquad S_{BET} = \frac{S_{total}}{a}$$

BET surface area measurements of different samples were carried out on a Quadrasorb-SI instrument at National Chemical Laboratory, Pune. This is a state-of-the-art, high-performance Surface Area Analyzer and Pore Size Analyzer with four independent analysis stations.

2.3.9 Cyclic Voltammetry and Electrochemical Charge-Discharge Measurement

Cyclic voltammetry or CV is a type of potentiodynamic electrochemical measurement. In a cyclic voltammetry experiment the working electrode potential is ramped linearly versus time like linear sweep voltammetry. Cyclic voltammetry takes the experiment a step further than linear sweep voltammetry which ends when it reaches a set potential. When cyclic voltammetry reaches a set potential, the working electrode's potential ramp is inverted. This inversion can happen multiple times during a single experiment. The current at the working electrode is plotted versus the applied voltage to give the cyclic voltammogram trace.

Cyclic voltammetry of as synthesized carbon sample and carbon coated ZnO was done to check there electrochemical properties. In a typical experiment carbon sample was coated uniformly on carbon paper electrodes on one side having area of 1 cm^2. The cathode and anode of the CV instrument is connected to these two electrodes, which immersed in 1M H_2SO_4 solution. Then the typical CV measurement is done at different scan rates and the CV curves were recorded. Figure 2.10 shows the typical CV curves of porous carbon at different scan rates. Cyclic Charge Discharge is the standard technique used to test the performance and cycle-life of EDLCs and batteries. A repetitive loop of charging and discharging is called a cycle. Most often, charge and discharge are conducted at constant current until a set voltage is reached.

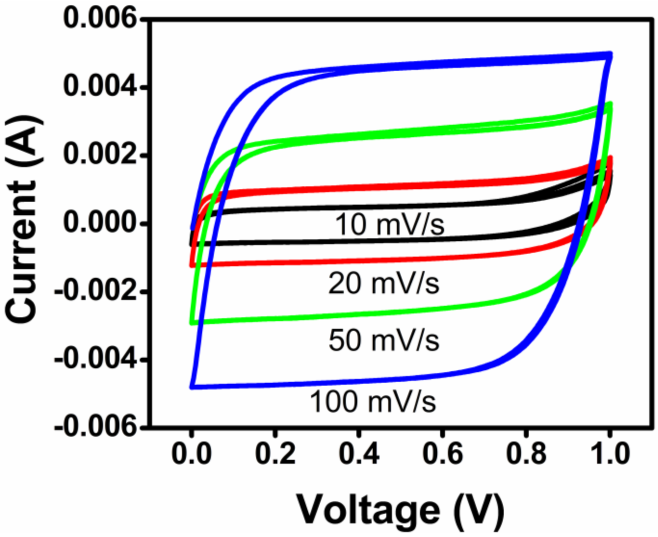

Fig. 2.10 *Typical Cyclic voltammogram of Porous carbon at various scan rates*

The charge (capacity) of each cycle is measured and the capacitance C, in farad (F), is calculated (from Equation 1). Both are plotted as a function of cycle number. This curve is called the capacity curve. In practice, charge is commonly called capacity. If capacity falls by a set value – 10 % or 20 % are customary – the actual number of cycles indicates the cycle-life of the capacitor. In general, commercial capacitors can be cycled for hundreds of thousands of cycles. This new EDLC shows almost ideal behaviour and the slope of the curve (dv/dt) is constant and is defined by following Equation.

$C = Q/V$ or $Q = CV$

So $\frac{dQ}{dt} = C_s \frac{dv}{dt} \rightarrow I = C_s \frac{dv}{dt} \rightarrow Cs = \frac{2I \frac{dt}{dv}}{m}$

Where, V is the cell potential in volts (V), I is the cell current in amperes (A), and Q is the charge in coulombs (C) or ampere-seconds (As). The factor 2 comes in the last equation to account for 2 electrode system. The capacitance (C) should be divided by the mass loading of carbon in order to get specific capacitance.

The cyclic voltammetry and other electrochemical characterisations were done on AutoLab PGSTAT 30, eco-chemie.

2.3.10 Superconducting Quantum Interferometery Device (SQUID)

SQUID is extensively exercised to perceive incredibly small magnetic moment of the order of 10^{-6} emu [13]. Such an immense sensitivity of the SQUID devices is associated with measuring changes in magnetic field related with one flux quantum. SQUID consists of two superconductors separated by thin insulating layers to form two parallel Josephson junctions. One of the discoveries associated with Josephson junctions was that flux is quantized in units.

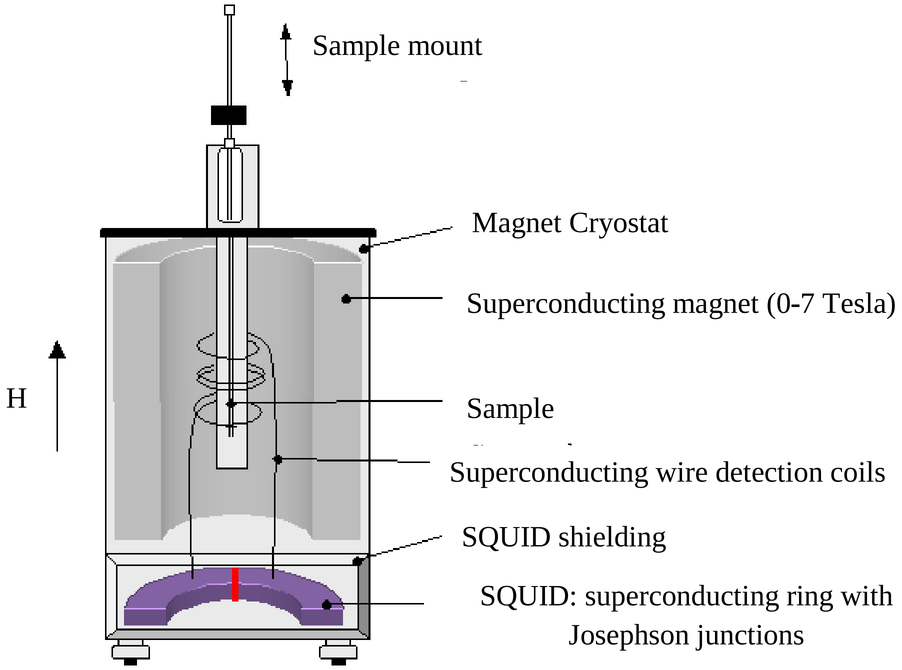

Fig. 2.11 *An illustration of SQUID Magnetometer*

Figure 2.11 shows the schematic diagram or illustration of SQUID Magnetometer. In SQUID magnetometer the sample is placed in an applied magnetic field of 0-11 Tesla produced by a superconducting magnet. The sample is moved slowly though a set of detection coils coupled to the SQUID via superconducting wires. The output voltage detected by the SQUID magnetometer is proportional to the magnetic moment of the sample. The SQUID output voltage, when properly calibrated using a sample of known magnetic moment, can be used to provide accurate values for the magnetization of the sample.

In the present work magnetic property measurements of Magnetite-GO composite using SQUID has been done on instrument Quantum Design MPMS SQUID VSM at National Chemical Laboratory, Pune. The SQUID magnetometer has certain advantages over the VSM, such as it provides better sensitivity (of the order of 10^{-6} emu) in the magnetization measurement as compared to the VSM sensitivity (of the order of 10^{-4} emu). This is because SQUID magnetometer involves superconducting Josephson junctions, which is very sensitive to any minute change in magnetic flux/voltage. For the operation of these Josephson junctions, they are maintained in liquid helium. Hence, at higher temperature (> 300K), the measurement is difficult as liquid helium starts boiling off. However, in VSM pick up coils do not require cooling for their operation. Therefore, VSM can be operated at higher temperature also.

2.3.11 Mössbauer Spectroscopy

Mössbauer spectroscopy is a versatile technique that can be used to provide information about the chemical, structural and magnetic properties of a material. [17] Key to the success of the technique is the discovery of recoilless γ-ray emission and absorption, referred to as the "Mössbauer Effect" [14]. Certain nuclei embedded in a solid matrix can emit or absorb γ-rays with no recoil, giving rise to resonant nuclear γ-ray absorption. Nuclei in atoms undergo a variety of energy level transitions, often associated with the emission or absorption of γ-rays. These energy levels are influenced by their surrounding environment, both electronic and magnetic, which can change or split these energy levels (Fig 2.11). These changes in energy levels can be probed using Mössbauer spectroscopy as the sensitivity of this technique is 1 eV in 10^{13} eV.

When source and absorber atoms are in different local environments, their nuclear energy levels are different (Figure 2.11). At its simplest (blue), this appears in the transmission spectrum as a shift of the minimum away from zero velocity; this shift is called isomer shift (IS or δ). The 1/2 and 3/2 labels represent the nuclear spin, or intrinsic angular moment, quantum numbers, 'I'. Interaction of the nuclear quadrupole moment with the electric field gradient leads to splitting of the nuclear energy levels (red). For ^{57}Fe, this causes individual peaks in the transmission spectrum to split into doublets (red) having a quadrupole splitting (QS or Δ). When a magnetic field is present at the nucleus, Zeeman splitting takes place, yielding a sextet pattern (green) and the internal magnetic field B_{hf} ; in the simplest case, the areas of the lines vary in the ratio of 3:2:1:1:2:3.

So Mössbauer spectra are described using three parameters: isomer shift (δ), which arises from the difference in *s* electron density between the source and the absorber, quadrupole splitting (Δ which is a shift in nuclear energy levels that is induced by an electric field gradient caused by nearby electrons, and hyperfine splitting (for magnetic materials only). Graphically, quadrupole splitting is the separation between the two component peaks of a doublet, and isomer shift is the difference between the midpoint of the doublet and zero on the velocity scale (Figure). So, these changes in the energy levels can provide information about the atom's local environment within a system. Mössbauer spectroscopy can only be applied to a relatively small group of atoms ^{57}Fe is by far the most common element studied using the technique.

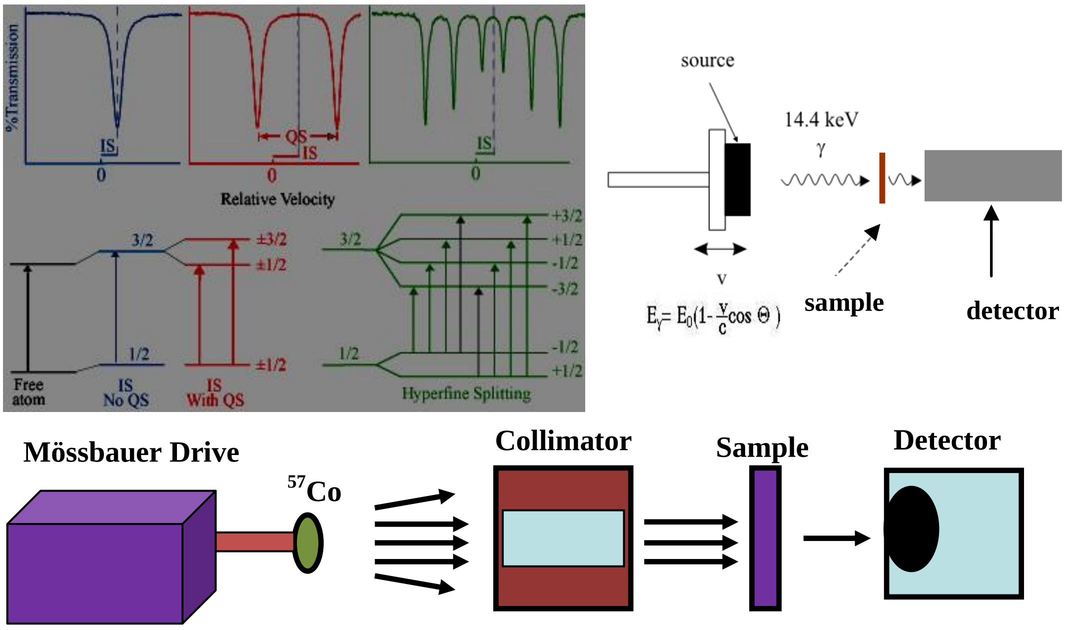

Fig. 2.12 Schematics of Mossbauer spectrometer and nuclear energy level splitting

Figure 2.12 shows the schematics of Mossbauer spectrometer and nuclear energy level splitting. The experiment was performed in transmission mode with a ^{57}Co(Rh) source in a Wissel spectrometer. The solid sample is exposed to the beam of γ radiation, and a detector measures the intensity of the beam that is transmitted through the sample. The γ-ray energy is varied by accelerating the gamma-ray source through a range of velocities with a linear motor. The relative motion between the source and sample results in an energy shift due to the Doppler effect (change in the apparent frequency of a wave as observer and source move toward or away from each other).

In the resulting spectra, gamma-ray intensity is plotted as a function of the source velocity. The source velocity is calibrated by means of a reference sample, metallic iron (B_{hf} = 33T). At velocities corresponding to the resonant energy levels of the sample, some of the gamma-rays are absorbed, resulting in a drop in the measured intensity and a corresponding dip in the spectrum. The number, positions, and intensities of the peaks provide information about the chemical environment of the absorbing nuclei and can be used to characterize the sample. The spectra as then computer-fitted assuming a Lorentzian line shape and isomer shifts are given relative to metallic iron. Mössbauer parameters are temperature-sensitive, and this characteristic is exploited by using lower temperatures to improve peak resolution and induce interesting magnetic phenomena. A Janis cryostat was used. Mossbauer spectroscopy was performed using ^{57}Co(Rh) ϒ-ray source and α-Fe foil as the standard for calibration. Measurements on magnetite-graphene oxide composite were done at Dept. of Physics, Rouen University, France.

2.3.12 Ferroelectric Analysis

Ferroelectricity is a property of certain materials which possess a spontaneous electric polarization that can be reversed by the application of an external electric field. The term is used in analogy to ferromagnetism, in which a material exhibits a permanent magnetic moment. Ferromagnetism was already known when ferroelectricity was discovered in 1920 in Rochelle salt by Valasek. Most materials are polarized linearly by an external electric field; nonlinearities are insignificant. This is called dielectric polarization. The electric permittivity, corresponding to the slope of the polarization curve, is thereby a function of the external electric field. In addition to being nonlinear, ferroelectric materials demonstrate a spontaneous polarization [15]. The distinguishing feature of ferroelectrics is that the direction of the spontaneous polarization can be reversed by an applied electric field, yielding a hysteresis loop. Ferroelectric crystals often show several transition temperatures and domain structure hysteresis, much as do ferromagnetic crystals. A ferroelectric crystal shows a reversible spontaneous electric polarization and a hysteresis loop that can be observed in certain temperature regions, delimited by a transition point called the Curie temperature, T_c. At temperatures above T_c, the crystal is no longer ferroelectric and exhibits normal dielectric behavior. Ferroelectric materials usually, but not always, exist in a nonpolar state at temperatures above Tc, and have anomalously high dielectric constants, especially near the Curie temperature. The dielectric constant increases very rapidly to a very high peak value at T_c. The anomalously high value of permittivity (ε_r) in the neighborhood of T_c is generally referred to as the anomalous value. At $T > T_c$, anomalous behavior follows closely the Curie–Weiss relation where C is known as the Curie constant.

$$\varepsilon_r = \frac{C}{T - T_c}$$

In fact, anomalous behavior always appears near any transition point between two different phases, even at T below T_c. At the transition points, there are anomalies not only in the dielectric constant and polarization, but also in piezoelectric and elastic constants and specific heat, because of the change in crystal structure. Ferroelectrics have reversible spontaneous polarization. The word spontaneous may mean that the polarization has a nonzero value in the absence of an applied electric field. The word reversible refers to the direction of the spontaneous polarization that can be reversed by an applied field in opposite direction. The spontaneous polarization Ps usually increases rapidly on crossing the transition point and then gradually reaches a saturation value at lower temperatures. The most prominent features of ferroelectric properties are hysteresis and nonlinearity in the relation between the polarization P and the applied electric field F.

Ferroelectricity analysis was carried out using aixACCT systems, GmbH Germany at ARDE, Pune.

2.13 REFERENCES:

[1] C. T. Nguyena, D. P. Kim, *J. Mater. Chem*. **2011**, *21*, 14226.

[2] A. Oya, S. Yoshida, J. Alcaniz-Monge, A. Linares-Solano, *Carbon* **1995**, *33*, 1085.

[3] Y. Yang, A. Centrone, L. Chen, F. Simeon, T. A. Hatton, G. C. Rutledge, *Carbon*, **2011**, *49*, 3395.

[4] J. Yamashita, M. Shioya, T. Kikutani, T. Hashimoto, *Carbon*, **2001**, *39*, 207.

[5] Z. P. Zhou, C. L. Lai, L. F. Zhang, Y. Qian, H. Q. Hou, D. H. Reneker, *Polymer*, **2009**, *50*, 2999.

[6] D. Dijkamp, T. Venkatesan, X. D. Wu, S. A. Shaheen, N. Jisrawi, Y. H. Min-Lee, W. L. McLean, M. Croft, *Appl. Phys. Lett.*, **1987**, *51*, 619.

[7] X. D. Wu, D. Dijkamp, S. B. Ogale, A. Inam, E. W. Chase, P. F. Miceli, C. C. Chang, J. M. Tarascon, T. Venkateshan *Appl. Phys. Lett.*, **1987,** *51*, 861.

[8] *Elements of X-ray Diffraction*, ed. by B. D. Cullity, Addison Wesley Publishing Co., **1978**.

[9] (a) C. N. Banwell, E. M. McCash, A Book: *Fundamentals of Molecular Spectroscopy*, 4th Ed., Tata McGraw Hill Publishing Co. Ltd., **2002** (b) Ph. D. Thesis by A. Sanyal, submitted to University of Pune, **Nov. 2006.**

[10] J. Coates, *Interpretation of Infrared Spectra: A Practical Approach*, *Encyclopedia of Analytical Chemistry*, R.A. Meyers (Ed.), *10815*, John Wiley & Sons Ltd, **2000**.

[11] T. H. Gfroerer, *Photoluminescence in Analysis of Surfaces and Interfaces*, *Encyclopedia of Analytical Chemistry*, R.A. Meyers (Ed.), 9209, John Wiley & Sons Ltd, Chichester, **2000**.

[12] A. Adamson, A. Gast, *Physical Chemistry of Surfaces*, *6th ed.*, Wiley, **1997**.

[13] (a) A. Barone *Principles and Applications of Superconducting Quantum Interference Devices*, ed. World Scientific Publishing, **1992**. (b) J. Clarke, *Scientific American* **1994**, *271*, 36.

[14] V. G. Bhide, Indian Ref: *Mössbauer Effect and Its Applications*, ed. by (Tata McGraw Hill, New Delhi, **1973**).

[15] K. Rabe, C. H. Ahn, J.-M. Triscone eds. *Physics of Ferroelectrics: A Modern Perspective*, **2007**, *105*, 1–30.

……

Chapter III

Carbon nanoscrolls and Magnetite-Graphene oxide nanocomposite by pyrolysis of a polymer

This chapter discusses the synthesis, properties and applications of carbon nanoscrolls obtained by pyrolysis of poly (acrylic acid-co-maleic acid) sodium salt. Further this chapter also discusses the synthesis and properties of magnetite-graphene oxide nanocomposites synthesized from pyrolysis of mixture of poly (acrylic acid-co-maleic acid) sodium salt and Fe-complex. In both synthesis methods the final product was obtained by soaking the pyrolyzed product in water for some time.

3.1 Introduction:

Carbon is amongst the most abundant elements in the Earth's crust and forms perhaps the widest variety of compounds of both organic and inorganic nature due its property of catenation and ability to form bonds with various elements. In the case of pure elemental carbon several allotropes such as the graphite, diamond, carbon nanotube (CNT), buckyball, Lonsdaleite, amorphous carbon, graphene are known with a range of interesting and diverse set of application-worthy properties [1-10] For instance, graphite is an excellent electrical conductor while diamond is electrically highly insulating. Carbon nanotubes can be conducting, semiconducting or insulating depending on their chirality. Importantly, most forms of pure carbon are biocompatible. Novel forms of carbon are also attractive due to their high surface area and conductivity for applications in supercapacitors and batteries. [11, 12] The functionality of carbon forms can be further tuned by making their composites with transition metal oxides. Indeed, metal oxide-carbon composites can serve not only as anode materials for lithium Ion batteries but also as efficient catalysts for various oxidation/reduction reactions. [13-15]

In this work we synthesize novel functional forms of carbon by simple pyrolysis of a polymer salt without and with Fe-complex. We show further that subsequent aqueous dissolution of the product of thermolysis leads to direct evolution of carbon nanascrolls in one case and magnetite-graphene oxide in other case.

Section I: Carbon nanoscrolls by the pyrolysis of polymer

3-I.1 Introduction

Over the years several physical and chemical routes have been developed to synthesize technologically important forms of carbon [16-18]. Since last two decades with the availability of high resolution microscopy techniques such as Transmission Electron Microscopy and Scanning Tunneling Microscopy, the research in carbon nanomaterials is progressed. There are several carbon nanoforms like carbon nanotubes, Fullerenes, graphene, carbon nanofibers that find interesting properties with diverse set of applications [1, 2, 19, 20]. Among these nanoforms, carbon nanoscrolls have received much attention during the last few years. Carbon nanoscrolls are open ended rolled sheets of graphene where the interlayer distance between adjacent rolled sheets corresponds to graphitic interlayer spacing. Bacon in 1960 first reported the presence of carbon nanoscrolls as scroll whiskers [21]. In 2003 Viculis et. al. showed that exfoliation of graphite produces a carbon sheet structure which on sonication leads to carbon nanoscrolls [22]. Similarly Prokofiev et. al. showed that when the oxidation product of graphite was sonicated, it leads to formation of carbon nanoscrolls [23]. Recently Chen et. al. showed that Carbon nanoscrolls can be formed by scrolling of functionalized graphene oxide single sheets by Langmuir–Blodgett (LB) approach [24]. Properties of carbon nanoscrolls are very interesting from application point of view. Due to rolled sheet structure, carbon nanoscrolls can easily undergo volume expansion. Also various simulation studies of carbon nanoscrolls show that the carbon nanoscrolls should possess high surface area and therefore useful for hydrogen storage. [25, 26]. These features are potentially important for a rich variety of applications, especially in the field of energy storage as cathode electrode in super-capacitors or batteries. There are a number of methods to synthesize these potentially important nano forms of carbon but the thermal decomposition of polymers (without or with a catalyst) represents an interesting synthesis strategy which can yield carbon fibers, carbon nanotubes, graphene and amorphous carbon [27-35]. Although there are many reports on the synthesis of carbon fibers and amorphous carbon by decomposition of polymers, there are relatively limited efforts towards catalyst-free thermal decomposition of suitably selected polymers for the synthesis of novel carbon forms [30]. Interestingly, the properties of the carbon forms depend on the starting precursors and the synthesis protocol. Rayon and polyacrylonitrile (PAN) are used as precursors for most of the commercial carbon fibers, although use of other precursors such as pitch, phenolic resins, and poly (vinylidene fluoride) (PVDF) poly (styrene sulfonate-co-maleic acid) has also been reported [28, 36-39]. Other than this various carbon nano forms like carbon nanotube, graphene can be synthesized by pyrolysis of polymers [29-32]. As polymers are the richest source of carbon, thermal decomposition of polymer is also an attractive strategy to synthesize novel carbon forms on the large scale.

In the light of these findings this section presents a catalyst-free synthesis method of carbon nanoscrolls by self-assembly of pyrolysed carbon form in aqueous medium. The pyrolysed carbon product obtained from poly (acrylic acid-co-maleic acid) sodium salt undergo self-assembly upon aqueous soaking. The structure and properties of these nanoscrolls are determined using a variety of techniques. The possible mechanism of formation of carbon nanoscrolls is discussed as well as their application in supercapacitor is explored.

3-I.2 Experimental Section

The poly (acrylic acid-co-maleic acid) sodium salt was obtained from Sigma Aldrich (Mol wt 50,000). For pyrolytic decomposition, the polymer was heated in a furnace at 500^0C for 1 hour in air atmosphere. The choice of the pyrolysis temperature was made by analyzing thermogravimetric data of poly (acrylic acid-co-maleic acid) sodium salt as seen in the fig. 3.1. The pyrolysed sample was then characterized using X-ray diffraction (XRD). It was confirmed that the product consists of carbon form and sodium carbonate (fig. 3.2). The product formed by pyrolysis of polymer was then soaked in water to remove the sodium carbonate and was dried subsequently. In a typical washing process the composite (about 2 g) was added to 100 ml D.I. water, mixed by shaking thoroughly and then the solution was kept undisturbed for some time. The carbon mass settled down after some time and a clear solution of water saturated with sodium carbonate was removed by a pipette. The carbon mass was again dispersed in fresh D.I. water. This process was repeated till the pH of carbon mass dispersed in water became neutral. This carbon mass was then dried. The dried carbon residue was then examined for the structural, chemical and morphological properties using various techniques such as X-ray diffraction (XRD, Philips X'Pert PRO), Raman spectroscopy (Confocal micro-Raman spectrometer LabRAM ARAMIS Horiba Jobin-Yvon apparatus with laser excitation wavelength of 532 nm), high resolution transmission electron microscopy (HRTEM, FEI Tecnai 300) and field emission scanning electron microscopy (FESEM, Hitachi S-4200). The surface area and porosity study were performed by the standard nitrogen adsorption (BET method) isotherm at 77K. Electrochemical measurements were performed with Autolab PGSTAT Potentiostat. Specific capacitance of carbon nanoscrolls was determined by cyclic Voltammetry (CV) measurements in 0.5M H_2SO_4. The scan rate for CV measurement was kept 50 mV/s.

3-I.3 Results and Discussions

Figure 3.1 shows the themogravimetric analysis of polymer in air atmosphere. It can be seen from the graph that polymer degrades to some extent about (40 %) upto 500^0C, which can be ascibed to conversion of polymer to carbon mass. Then the weight loss is not much which can be ascribed to air oxidation of carbon compound.

Figure 3.2 shows the FESEM image of as pyrolysed product of polymer and the corresponding XRD spectra. It truely indicates formation of sodium carbonate and a carbon mass.

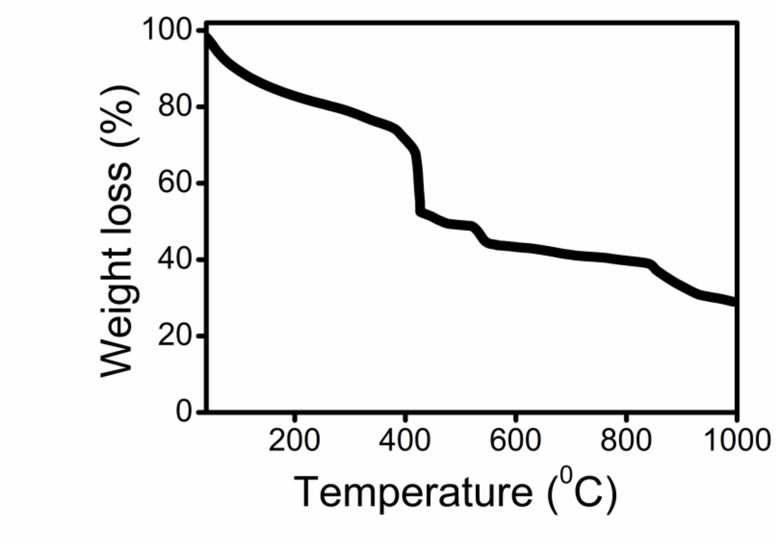

Fig. 3.1 *TGA of polymer in air atmosphere*

Figure 3.3 shows the electron microscope images of the dried carbon residue from the pyrolysis. Figure 3.3a shows the high resolution scanning electron microscopy (SEM) image, while Figure 3.3b shows the transmission electron microscopy (TEM) image. Both these images reveal a 3D interlaced random wire-like network

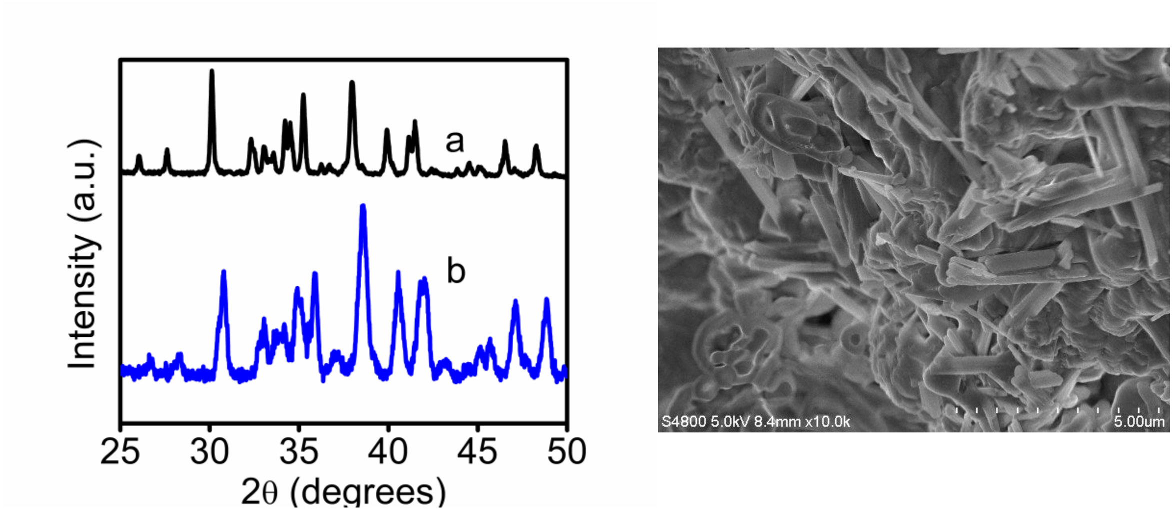

Fig. 3.2 *XRD spetrum and FESEM image of as pyrolysed product of polymer*

Figure 3.3c shows the high resolution TEM image of a single tubule. The average length of the same is several microns while the diameter is around 15-20 nm. The average d-spacing between the two neighbouring carbon walls is around 0.34 nm (line plot of d-spacing shown as inset) [40]. The TEM of the terminal end of one isolated tubule is also shown in the figure 3.3d, which resembles a rolled sheet of graphene, termed as a nanoscroll [22,40,41].

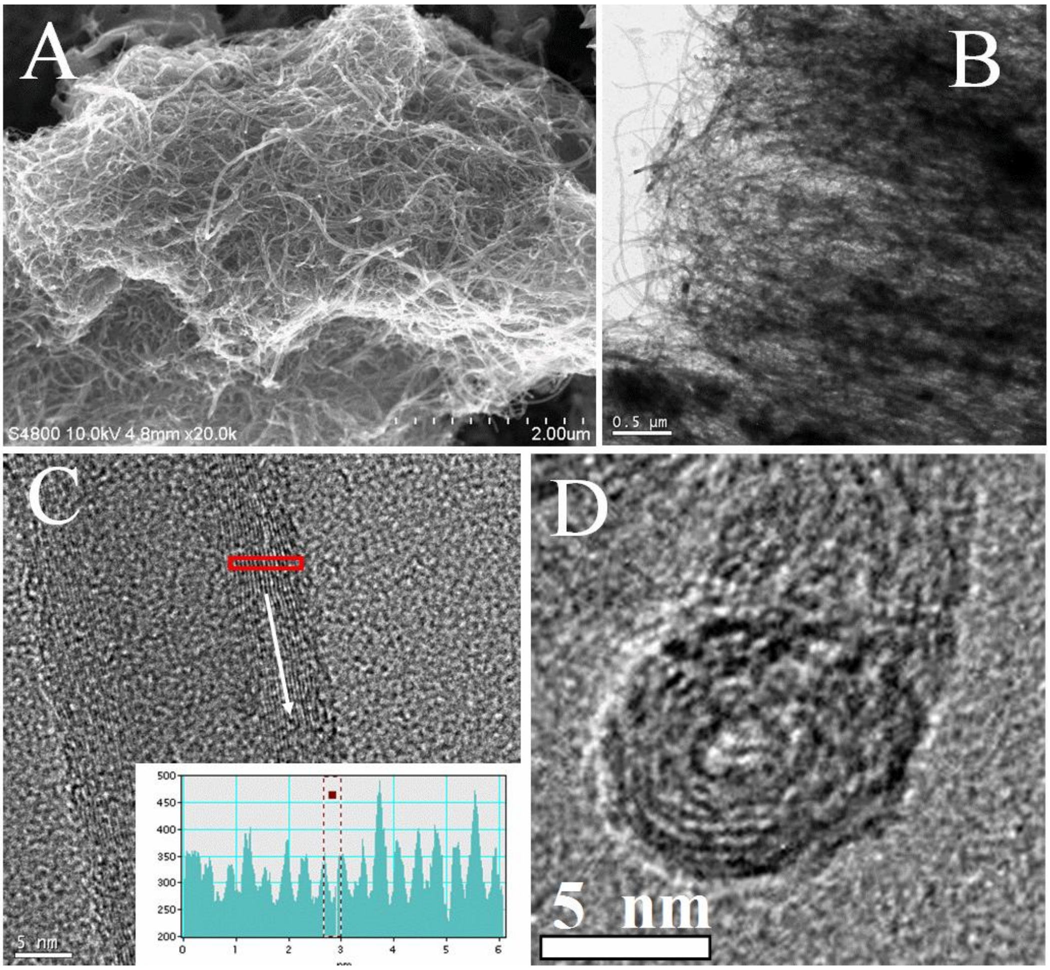

Fig. 3.3 *A) SEM, B) TEM, C) and D) High resolution TEM images of carbon nanoscrolls.*

The possible mechanism for formation of carbon nanoscroll can be given as below. Upon pyrolysis of the polymer, first a carbon sheet with sodium carbonate is formed. This can be considered as a bottom-up process wherein the 1D polymer chain is converted to 2D carbon sheet. We suggest a possible mechanism with reference to Figure 3.4. When the poly (acrylic acid-co-maleic acid) sodium salt is heated, adjacent polymer chains undergo a condensation reaction with loss of sodium carbonate at every linkage (Figure 3.4A). There is an additional loss of a CO molecule leading to the formation of 2D stable six-membered ring structure.

Due to the high temperature treatment, the carbon six membered ring structures undergo aromatization. When the condensation followed by cyclization reaction occurs only between the maleate units on the adjacent polymer chains, aromatic hexagonal ring systems are formed leading to the formation of an extended graphitic network.

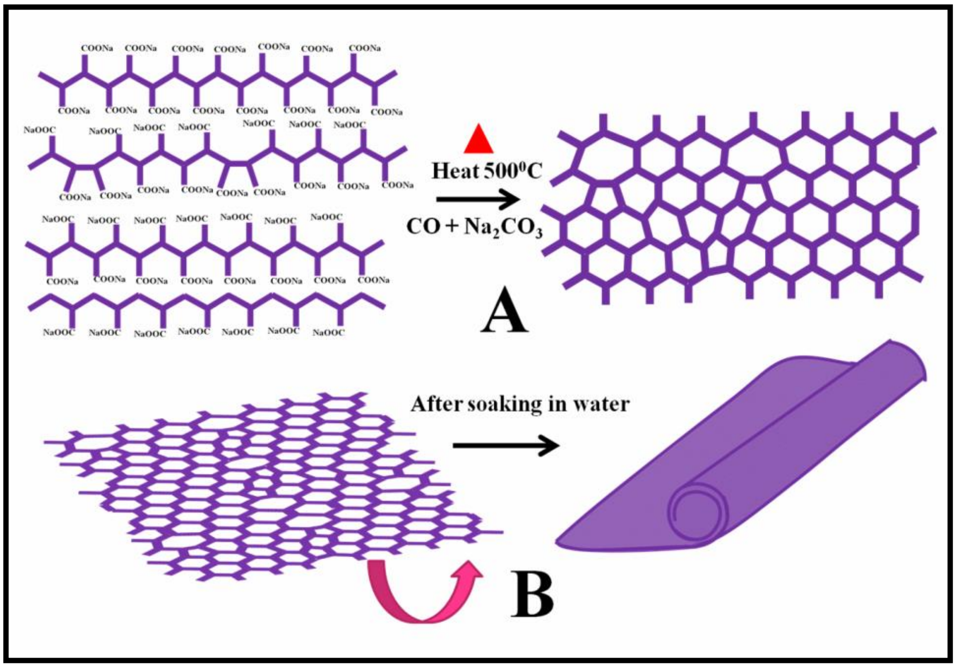

Fig.3.4 *Schematic of the suggested mechanism for the formation of graphitic carbon sheets during soaking process of pyrolysed product of poly (acrylic acid-co maleic-acid) sodium salt.*

However there are several possibilities of similar cyclization between the maleate units and acrylate units of different polymer chains resulting in the formation of pentagonal and heptagonal defects. The overall structure thus formed by this process is a graphene-like sheet with defects. The by-products of pyrolysis process are CO and Na_2CO_3. Since the pentagonal/heptagonal defects exert a strain in the graphene like sheet of carbon obtained by this process, there is a strong tendency of this sheet to roll around like a carbon nanotube. But the sodium carbonate formed in the process of pyrolysis, obstruct the rolling of nanosheets into carbon nanoscrolls. Once the pyrolised product is soaked in D.I. water, the formed carbon sheets favour the formation of carbon nanoscrolls as shown in figure 3.4B. In this context it is important to mention that Chen et. al. also discussed the scrolling of graphite oxide (GO) sheets on sonication in aqueous medium to carbon nanoscroll [24]. In our case during the process of water soaking the sodium carbonate dissolves in water, and rolling of nanosheets lead to formation of 3D network of carbon nanoscrolls. This is due to favourable van der Walls interaction within the carbon sheet which tends to scroll around itself in order to have minimum energy state.

Figure 3.5A shows the XRD spectrum of the as synthesized carbon nanoscrolls. The broad peak at around 26^{o} is a characteristic of graphitic carbon which has a d-spacing of ~ 0.34 nm. This value of interlayer distance consistent with that obtained from the HRTEM image (Figure 3.3c inset). This broad peak at 2θ = 26º is absent in the as-pyrolysed polymer as can be seen in figure 3.2. This suggests that the rolling of carbon sheet takes place during aqueous soaking of pyrolysed polymer and it leads to formation of carbon nanoscrolls.

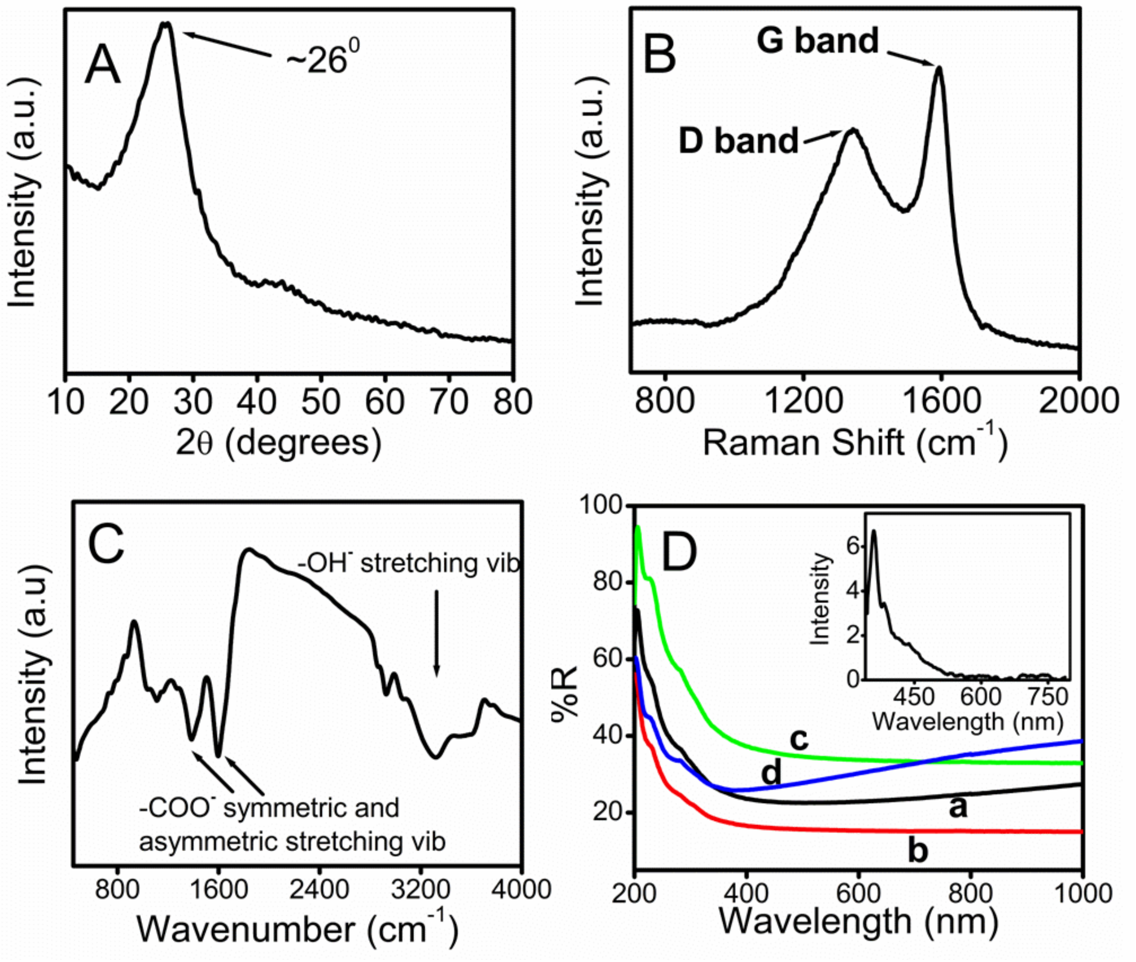

Fig. 3.5 *A) XRD B) Raman C) FTIR and D) UV-Vis-NIR diffuse reflectance spectrum of carbon nanoscrolls 'curve (a)', MWCNT 'curve (b)', chemically converted graphene 'curve (c)' and GO 'curve (d)' Inset of figure 4D shows the photoluminescence spectrum of carbon nanoscrolls.*

Figure 3.5B shows the Raman spectrum of as synthesized carbon nanoscrolls. The 1590 cm^{-1} signature peak corresponds to the G band. Generally this peak is present at 1580 cm^{-1} in the case of graphite, CNTs and defect-free single layer graphene and carbon nanoscrolls [42-45]. As the extent of oxidation in graphitic system increases this peak shifts to higher wave numbers [46,47]. These functional groups increase the defect sites on carbon nanoscrolls surface, thereby shifting the G band peak from 1580 to 1590 cm^{-1}. The D band at about 1320 cm^{-1} is also present in carbon nanoscrolls, which corresponds to disordered nature (defects) of the graphite like system. This peak is usually present in MWCNTs, carbon nanoscrolls and is absent in defect-free graphite and defect-free single layer graphene [42-47]. In carbon nanoscrolls or carbon nanotubes the D band in Raman spectrum arises due to defect sites which are inherent due to their rolled structure. Figure 3.5C shows the FTIR spectrum for the as synthesized carbon nanoscrolls. The characteristic band at 1600 cm^{-1} in carbon nanoscrolls is due to C=O asymmetric stretching of carboxylate anion that is reconfirmed by another peak at 1373 cm^{-1}, which is related to the symmetric stretching mode of the carboxylate groups [48]. The broad peak at around 3200 cm^{-1} is a characteristic signature of the hydroxyl group. It is interesting to compare the UV-Vis-NIR diffuse reflectance spectra of carbon nanoscrolls with MWCNT, GO, CCG, as in figure 3.5D. Graphene, MWCNT etc. do not possess a band gap; on the other hand GO possesses band gap which depends on the extent of oxidation [49]. Since the pyrolysis process is carried out in air, the resulting carbon nanoscrolls have oxygen functional groups. It is clear from the optical data shown in figure 3D, that the trend for our carbon nanoscrolls sample is intermediate between that for CCG/MWCNT and GO (increasing nature towards longer wavelengths). Clearly there is some contribution from oxidized carbon in our nanoscrolls. The Inset of figure 3.5D shows the PL spectrum of the carbon nanoscrolls sample. The excitation wavelength was 320 nm. The PL emission occurs at 360 nm. Carbon nanoscrolls have carboxyl functional groups which increase the defect sites on carbon nanoscrolls. These trap states give the photoluminescence near 360 nm [50].

Table 1 shows the comparison of Brunauer Emmett Teller (BET) surface area and porosity data for the carbon nanoscrolls. The surface area of the carbon nanoscroll sample is ~188 m^2/g. Due to high surface area of carbon nanoscrolls, these were exploited for the supercapacitor application.

	Carbon nanoscrolls
BET surface area (m^2/g)	188.4
Pore volume (cm^3/g)	0.266
Pore Radius Dv(r) (nm)	1.48

Table.3.1 *BET surface area and porosity data for the carbon nanoscrolls.*

Figure 3.6 ‘Curve A’ shows the CV of carbon nanoscrolls. The CV profiles exhibit a nearly symmetrical or slightly skewed rectangular shape. The value of specific capacitance was calculated by integrating area of CV curves. The specific capacitance value for carbon nanoscrolls is around 2 F/g. The low value of specific capacitance is due to defect sites present in carbon nanoscrolls which reduces electron transport properties of carbon nanoscrolls. This is due to air pyrolysis of polymer which is one of the steps in the formation of carbon nanoscrolls. These as synthesized carbon nanoscrolls were further annealed in argon atmosphere at 1000^0C for 2 hour. Curve B in figure 3.6 shows the CV of argon annealed carbon nanoscrolls which shows specific capacitance value of around 30 F/g. The specific capacitance value of argon annealed carbon nanoscrolls is comparable to that of carbon nanotubes which is reported to be about 40-50 F/g [51,52].

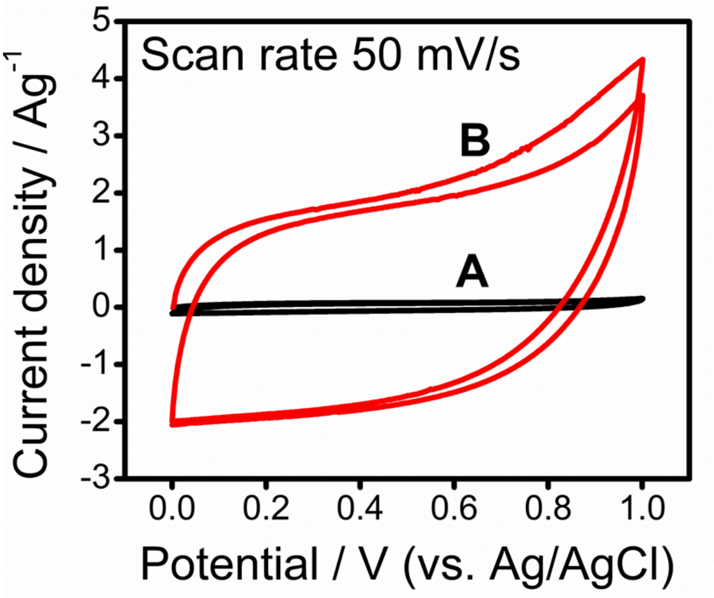

Fig. 3.6 *Cyclic voltammetric behaviour of as synthesized carbon nanoscrolls (Curve A) and argon annealed carbon nanoscrolls (Curve B)*

Before we conclude it is useful to point out that the unique morphology of nanoscrolls may be amenable to interesting magnetic effects. Hence, we carried out Electron Spin Resonance (ESR) and SQUID measurements on the sample. The corresponding results are presented below in fig. 3.7. The ESR spectrum of carbon nanoscrolls suggests presence of strong paramagnetic centres with g value ~2.0015. There are reports of paramagnetic centre in graphene, carbon nanotubes etc. with g value of 2.00 to 2.005 [53-55]. Also the presence of single ESR peak suggests no interaction of hydrogen (proton) with the unpaired electrons. The SQUID magnetization data suggests a weak coupling of paramagnetic centres to give mild ferromagnetism.

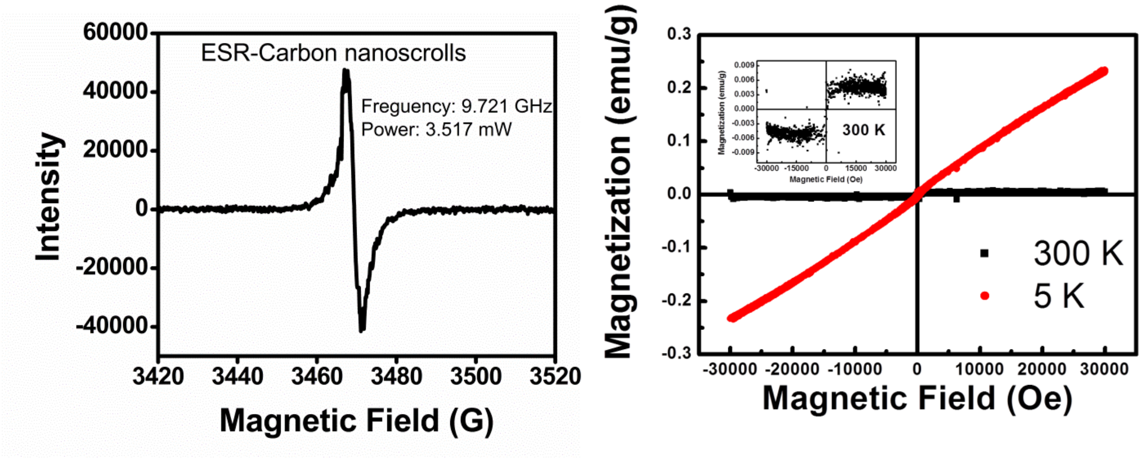

Fig. 3.7 *ESR spectrum and MH (magnetization) curve of carbon nanoscrolls.*

4-I.4 Conclusion

In summary this section demonstrated catalyst free efficient route for the synthesis of carbon nanoscrolls starting from pyrolysis of polymer. Pyrolysis of poly (acrylic acid co maleic acid) sodium salt leads to formation of carbon form and sodium carbonate. The carbon part of decomposition products undergo self-assembly upon its aqueous soaking to form carbon nanoscrolls. It is found that the as synthesized carbon nanoscrolls have ordered structure with interlayer distance of 0.34 nm.

Section II: Magnetite-Graphene oxide nanocomposite from pyrolysis of polymer

3-II.1 Introduction

There are several nano forms of carbon like graphene, carbon nanotube, graphene oxide which have interesting properties, and also are important for many applications in energy related problems. Graphene oxide (GO) is also such carbon lamellar flexible material with a wide range of functional groups, such as epoxy (C-O-C), hydroxyl (OH), and carboxyl (COOH) groups, on both basal planes and edges. Therefore, it can be easily exfoliated and functionalized to form homogeneous suspensions in both water and organic solvents, providing more possibility for synthesis of graphene-based materials. This material then can be used for various applications such as anode material in supercapacitors, batteries etc. The functionality of carbon forms can be further tuned by making their composites with transition metal oxides. Indeed metal oxide-carbon composites can serve not only as anode materials for lithium Ion batteries but also as efficient catalysts for various oxidation/reduction reactions. The existence of oxygen functional groups and aromatic sp^2 domains allow GO to participate in a wide range of bonding interactions. Here we also demonstrate the bonding of GO sheets with magnetite particles that renders various interesting properties.

3-II.2 Experimental Section

In this work we show the synthesis of magnetite-graphene oxide composite by pyrolysis route. In a typical experiment 1:1 wt% homogeneous physical mixture of Poly (acrylic acid-co-maleic acid) sodium salt and Fe-complex [Fe(III) (2'-hydroxy chalcone)$_3$] was heat treated in furnace in air at 500^{0}C for a specified time duration. It was observed that thermolysis of mixture of polymer and Fe-complex leads to a ferromagnetic Fe_3O_4 (Magnetite)-graphene oxide-sodium carbonate composite which on aqueous soaking leas to Magnetite-graphene oxide (M-GO) composite.

3-II.2 Results and discussion

Figure 3.8 shows the FESEM image of one of the sheets in the M-GO composite. The length of sheet is of the order of several microns, as seen in the figure 3.8a. Figure 3.8b shows the high resolution TEM image of the same composite which shows a very uniform distribution of the Fe_3O_4 nanoparticles over the surface of GO.

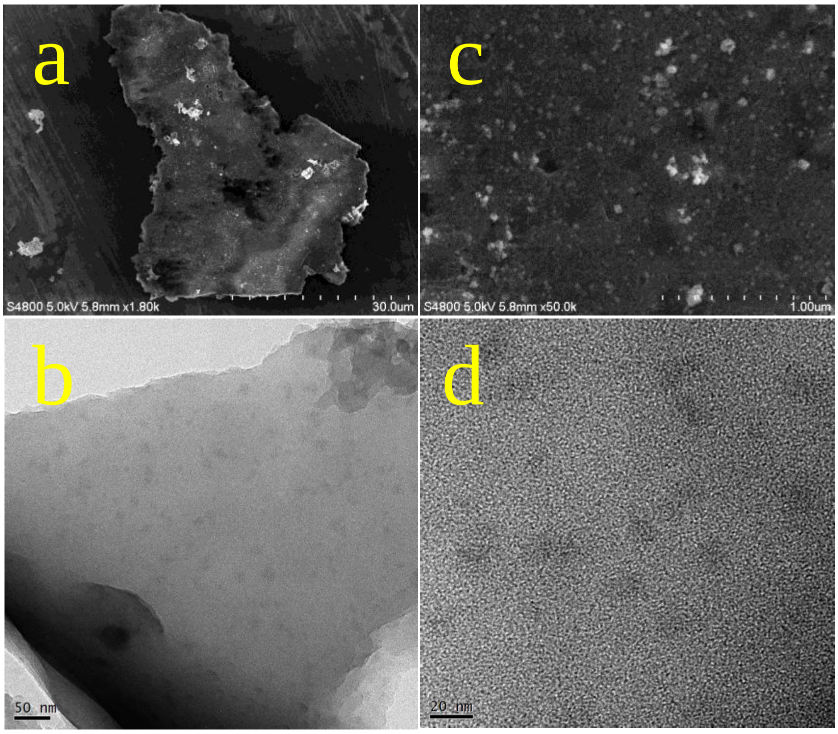

Fig. 3.8 *a) FESEM and b) TEM images of the as-synthesized* Fe_3O_4*-GO nanocomposite. Figures c and d show high resolution images.*

The average size of the Fe_3O_4 nanoparticles is around 20 nm, which is also confirmed from the high resolution TEM images shown in Fig. 3.8c and 3.8d. We used Mössbauer spectroscopy to confirm the specific phase of the nanoparticles. Figure 3.9 shows the Mössbauer spectrum of M-GO composite. The hyperfine interaction parameters corresponding to the two fitted sextets to the Mössbauer spectrum (sextet 1: IS (mm/s) – 0.172 ± 0.009, $\Gamma/2$ (mm/s) – 0.234 ± 0.015, H(T) – 493 ± 1, Area – 37% , sextet 2: IS (mm/s) – 0.550 ± 0.012, $\Gamma/2$ (mm/s) – 0.410 ± 0.021, H(T) – 460 ± 1, Area – 63%) unequivocally confirm that the nanoparticle phase is Fe_3O_4 or magnetite. This confirmation is important because both magnetite and maghemite (gamma-Fe_2O_3) nearly yield comparable XRD data, hence atomistic characterization through hyperfine interaction parameters is useful to decipher the phase identity. It is interesting to note that there is no signature of graphitic carbon in the XRD of the M-GO composite. Fig 3.10A shows the XRD pattern of M-GO composite which shows peaks (mark peaks in figure) that correspond to Fe_3O_4.

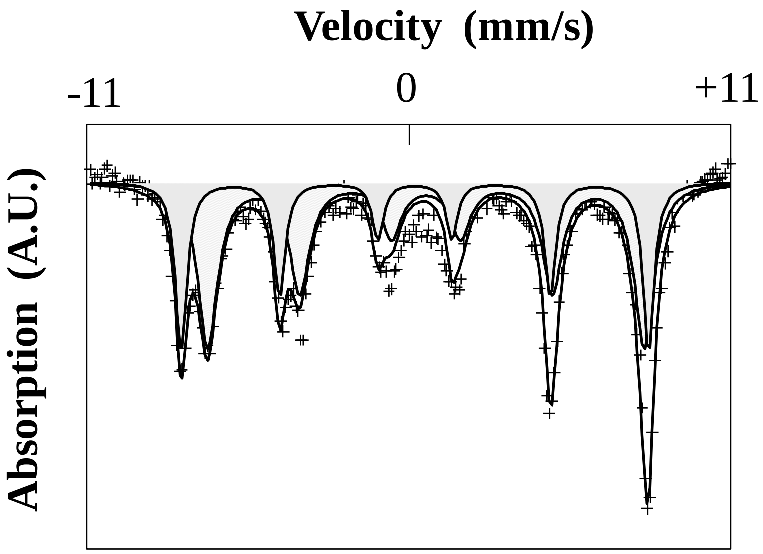

Fig. 3.9 *Mössbauer spectra of M-GO composite.*

Figure 3.10B shows the Raman spectra for the cases of M-GO composite. It can be clear that the characteristic peak at 1590 cm^{-1} which corresponds to the graphitic nature of carbon, known as the G band, is present in M-GO composite. Generally this peak is present at 1580 cm^{-1} in the case of graphite, CNTs and defect free single layer graphene.[42-45] As the extent of oxidation in graphitic system increases, this peak shifts to higher wave numbers [46,47] In the case of GO, this peak is located at 1600±5 cm^{-1}.

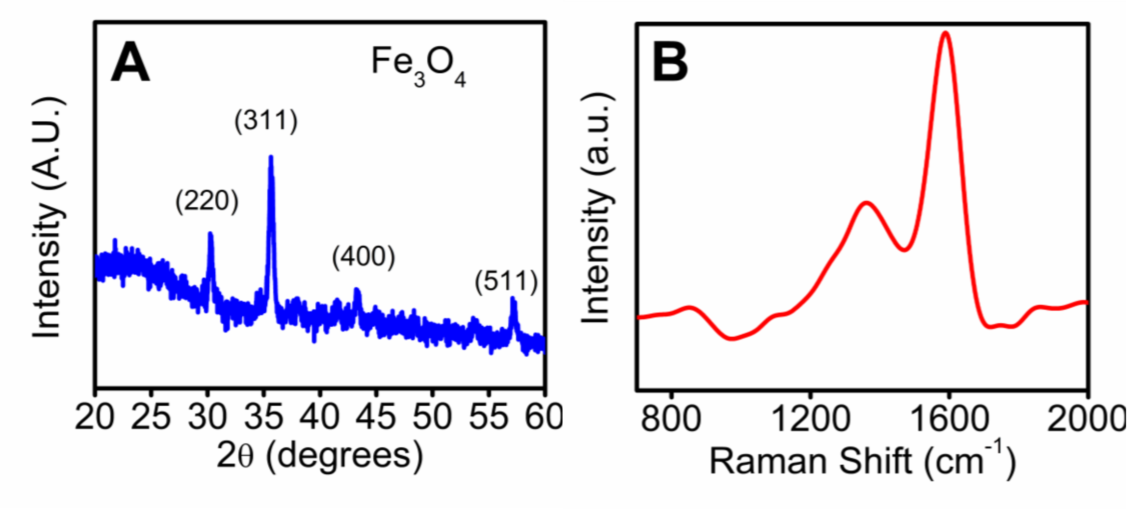

Fig. 3.10 *XRD and Raman spectra of M-GO composite.*

The D band at about 1320 cm^{-1} is present in all the cases, which corresponds to disordered nature (defects) in graphite like system. This peak is usually present in MWCNT, GO and is absent in graphite and defect free single layer graphene. [42-47].

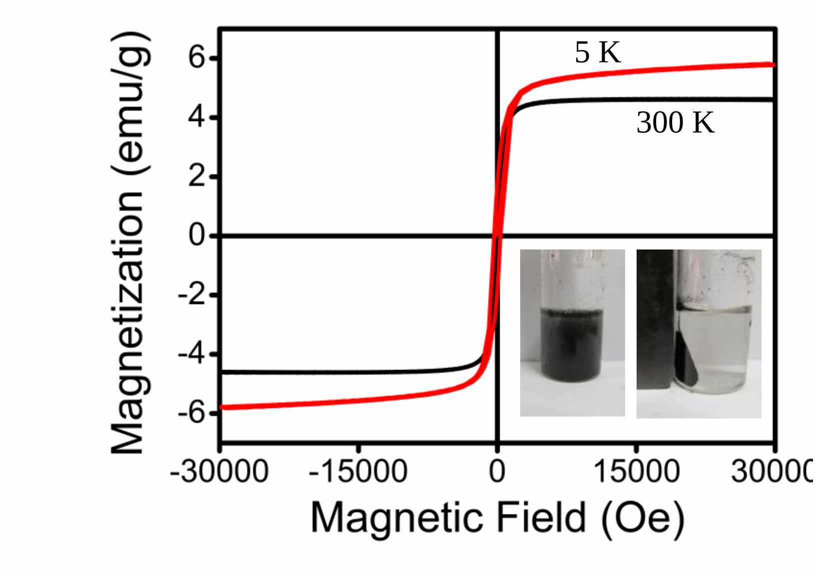

Fig. 3.11 *Magnetization data of M-GO composite. Inset shows photo of M-GO composite that gets pulled near magnet.*

Figure 3.11 shows the magnetic hysteresis loops for 20nm M-GO composites measured at 300 K and 5 K. The profiles of the magnetization curves corresponding to the 20 nm M-GO composite are characteristic of strongly ferromagnetic nanoparticles. The saturation magnetization of the M-GO composite and is around 5 emu/g at 300K and around 6 emu/g at 5K respectively. The lower value in our composite case reflects carbon loading of the magnetic component. The amount of the Fe_3O_4 component in the 20 nm M-GO composites is thus estimated to be around 10%.

	Fe_3O_4-GO composite
BET surface area (m^2/g)	91.7
pore volume (cm^3/g)	0.058
Pore Radius Dv(r) (nm)	3.02

Table 3.2 *BET surface areas and porosity data of Fe_3O_4-GO composite*

Table 3.2 shows the BET surface areas and porosities of Fe_3O_4-GO composite measured by N_2 adsorption desorption method. The surface area of the Fe_3O_4-GO composite is ~ 92 m^2/g. The pore radius in the case of M-GO composite is around 3 nm indicating mesoporous nature. The high surface area of M-GO composite is very important considerations for applications like fuel cell, hydrogen storage, supercapacitors and Li-ion battery. [11-15, 56]

3-II.4 Conclusion

In this work, we demonstrate the successful synthesis of magnetite-graphene oxide (M-GO) composite by pyrolysis route. This represents a very simple and catalyst free route for the synthesis of M-GO composites. The composite also possesses excellent magnetization as well as surface area properties.

General Conclusion

Polymer pyrolysis offers an interesting route to the synthesis of functional forms of carbon. The specific form can be guided and manipulated by proper choice of the initial polymer as well as the specific protocol for pyrolysis and post-pyrolysis treatment. Polymer poly (acrylic acid-co-maleic acid) sodium salt when pyrolysed without and with Fe-complex, it leads to formation of carbon nanoscrolls in one case and magnetite-graphene oxide in another case.

3.2 References

[1] S. Iijima, *Nature,* **1991**, *354,*56.

[2] H. W. Kroto, J. R. Heath, S. C. O’Brien, R. F. Curl, R. E. Smalley, *Nature,* **1985**, *318,* 162.

[3] C. Frondel, U. B. Marvin, *Nature*, **1967**, *214,* 587.

[4] S. E. Stenkvist, B. Bowman B, *Plasma Technology in Metallurgical Processing,* **1987**, 103.

[5] M. H. Cho, S. J. Kim, R. H. Basch, J. B. Fash, H. Jang, *Tribology International* **2003**, *36*, 537.

[6] W. Xiaohong, Q. Wei, G. Yun, X. Zhaoyang, *Applied Surface Science,* **2008**, *254,* 6395.

[7] K. Amine, J. Liu, S. Kang, I. Belharouak, Y. Hyung, D. Vissers, G. Henriksen, *Journal of Power Sources.* **2004**, *129,*14.

[8] T. Lierse, M. Kaiser, *Industrial Diamond Review,* **2002**.

[9] H. K. Tonshoff, H. Hillmann-Apmann, J. Asche, *Diamond and Related Materials* **2002**, *11*, 736.

[10] I. P. Hayward, *Surface and Coatings Technology*, **1991**, *49*, 554.

[11] M. Noked, A. Soffer, D. Aurbach, *J Solid State Electrochem*, **2011**, *15*,1563.

[12] M. Endo, Y. A. Kim, T. Hayashi, K. Nishimura, T. Matusita, K. Miyashita, M. S. Dresselhaus, *Carbon* **2001**, *39*, 1287.

[13] J. Su, M. Cao, L. Ren, C. Hu, *J. Phys. Chem. C* **2011**, *115*, 14469.

[14] X. Zhu, Y. Zhu, S. Murali, M. D. Stoller, R. S. Ruoff, *ACS Nano* **2011**, *5*, 3333.

[15] M. Biswal, V. Dhas, V. Mate, A. Banerjee, P. Pachfule, K. Agrawal, *J. Phys. Chem. C* **2011**, *115*, 15440.

[16] T. Ebbesen, P. Ajayan, *Nature* **1992**, *358*, 220.

[17] T. Guo, P. Nikolaev, A. Thess, D. Colbert, R. Smalley, *Chemical Physics Letters* **1995**, *243*, 49.

[18] A. Eftekhari, P. Jafarkhani, F. Moztarzadeh, *Carbon* **2006**, *44*, 1343.

[19] G. Tibbetts, *Journal of Crystal Growth*, **1985**, *73*, 431.

[20] A. Geim, K. Novoselov, *Nature Materials*, **2007**, *6*, 183.

[21] R. Bacon, *J Appl Phys*, **1960**, *31*, 283.

[22] L. Viculis, J. Mack, R. Kaner, *Science*, **2003**, *299*, 1361.

[23] M. Savoskin, V. Mochalin, A. Yaroshenko, N. Lazareva, T. Konstantinova, I. Barsukov, I. Prokofiev, *Carbon*, **2007**, *45*, 2797.

[24] Y. Gao, X. Chen, H. Xu, Y. Zou, R. Gu, M. Xu, A. Jen, H. Chen, *Carbon*, **2010**, *48*, 4475.

[25] G. Mpourmpakis, E. Tylianakis, G. Froudakis, *Nano Lett.* **2007**, *7,* 1893.

[26] V. Coluci, S. Braga, R. Baughman, D. Galvao, *Phys. Rev. B*, **2007**, *75*, 125404.

[27] A. Lu, W. Li, E. Salabas, B. Spliethoff, F. Schuth, *Chem Mater.* **2006**, *18*, 2086.

[28] Y. Yang, A. Centrone, L. Chen, F. Simeon, T. Hatton, G. C. Rutledge, *Carbon*, **2011**, *49*, 3395.

[29] V. Pol, P. Thiyagarajanb, *J Environ Monit.* **2010**, *12*, 455.

[30] W. Cho, E. Hamada, Y. Kondo, K. Takayanagi, *Appl Phys Lett.*, **1996**, *69*, 278.

[31] Z. Sun, Z. Yan, J. Yao, E. Beitler, Y. Zhu, J. Tour, *Nature*, **2010**, *468*, 549.

[32] S. Byun, H. Lim, G. Shin, T. Han, S. Oh, J. Ahn, *J Phys Chem Lett*, **2011**, *2*, 493.

[33] T. Zhao, Y. Liu, J. Zhu, *Carbon*, **2005**, *43,* 2907.

[34] N. Kobayashi, M. Kijima, *J Mater Chem.*, **2007**, *17*, 4289.

[35] C. Nguyena, D. Kim, *J Mater Chem*., **2011**, *21*, 14226.

[36] A. Oya, S. Yoshida, J. Alcaniz-Monge, A. Linares-Solano, *Carbon*, **1995**, *33*, 1085.

[37] J. Yamashita, M. Shioya, T. Kikutani, T. Hashimoto, *Carbon*, **2011**, *39*, 207.

[38] S. Shin, J. Janga, S. H. Yoon, I. Mochida I, *Carbon*, **1997**, *35*, 1739.

[39] H. Hines, A. Bagreev, and T. Bandosz, *Langmuir*, **2004**, *20*, 3388.

[40] J. Zheng, H. Liu, B. Wu, Y. Guo, T. Wu, G. Yu, Y. Liu, D. Zhu, *Adv. Mater*. **2011**, *23*, 2460.

[41] X. Xie, L. Ju, X. Feng, Y. Sun, R. Zhou, K. Liu, *Nano Lett.*, **2009**, *9*, 2565.

[42] D. Graf, F. Molitor, K. Ensslin. C. Stampfer, A. Jungen, C. Hierold, *Nano Lett.*, **2007**, *7*, 238.

[43] C. Casiraghi, S. Pisana, k. Novoselov, A. Geim, A. Ferrari, *Appl Phys Lett*., **2007**, *91*, 233108.

[44] M. Dresselhaus, G. Dresselhaus, R. Saito, A. Jorio, *Physics Reports*, **2005**, *409*, 47.

[45] H. Zhou, C, Qiu, H. Yang, F. Yu, M. Chen, L. Hu, *Chemical Physics Letters*, **2011**, *501*, 475.

[46] L. Liu, S. Ryu, M. Tomasik, E. Stolyarova, N. Jung, M. Hybertsen, *Nano Lett.*, **2008**, *8*, 1965.

[47] K. Kudin, B. Ozbas, H. Schniepp, R. Prudhomme, I. Aksay, R. Car, *Nano Lett.*, **2008**, *1*, 36.

[48] R. Silverstein, F. Webster, Spectrometric Identification of Organic Compounds, 6th edn, **1998**, Wiley, New York.

[49] G. Eda, Y. Lin, C. Mattevi, H. Yamaguchi, H. Chen, I. Chen, C. Chen, M. Chhowalla, *Adv. Mater*. **2010**, *22*, 505.

[50] L. Minati, G. Speranza, I. Bernagozzi, S. Torrengo, L. Toniutti, B. Rossi, M. Ferrari, A. Chiasera, *J. Phys. Chem. C.*, **2010**, *114*, 11068.

[51] W. Chen, Z. Fan, L. Gu, X. Baoc, C. Wang, *Chem. Comm.*, **2010**, *46*, 3905.

[52] C. Du, N. Pan, *Nanotechnology*, **2006**, *17*, 5314.

[53] S. Rao, A. Stesmans, K. Keunen, D. Kosynkin, A. Higginbotham, J. Tour, *Appl Phys Lett*., **2011**, *98*, 083116.

[54] M. Zaka, Y. Ito, H. Wang, W. Yan, A. Robertson, Y. Wu, M. Rummeli, D. Staunton, T. Hashimoto, J. Morton, A. Ardavan, G. Briggs, J. Warner, *ACS Nano*, **2010**, *4*, 7708.

[55] K. Shen, D. Tierney, T. Pietra, *Phys. Rev. B.*, **2003**, *68*, 165418.

[56] G. Srinivas, Y. Zhu, R. Piner, N. Skipper, M. Ellerby, R. Ruoff, *Carbon*, **2010**, *48*, 630.

Chapter IV

A 3D Hexaporous Carbon Assembled from Single-Layer Graphene as High Performance Supercapacitor

This chapter discusses the synthesis, properties and applications of single-layer-graphene-assembled 3D hexaporous carbon. The single-layer-graphene-assembled 3D hexaporous carbon is synthesized from pyrolysis of poly (4-styrenesulfonic acid-co-maleic acid) sodium salt. This method represents a facile approach to fabricate 3D graphene-based meso-microporous materials. The process is catalyst/template free and generates hierarchical structure of microporous as well as mesoporous graphene with hexagonal nanopores of uniform size and shape. The as-synthesized single-layer-graphene-assembled porous carbon is highly conducting in nature with specific conductivity of 23 S/m and also exhibits extremely high surface area of 1720 m^2/g. The electrochemical properties of single-layer-graphene-assembled porous carbon are investigated in *aqueous medium* which shows maximum capacitance of 154 F/g.

4.1 Introduction

Electrical energy drives the engines of growth and development of the modern world. Hence energy systems are invariantly engineered to convert most forms of energy (petroleum, natural gas, coal, solar, wind, nuclear) to the electrical form of energy. If not used efficiently or stored properly such energy gets wasted. Use of electrical energy concurrently with its generation is not always feasible hence electrical energy storage is as important as its generation. There are several ways for storage of energy such as batteries; capacitors etc. [1, 2]. Amongst these, carbon based electrochemical capacitors (ECs) are attracting significant attention recently because of their various rather unique quality factors [3, 4]. It is contemplated that with conceptual improvements in design as well as use of novel materials systems these supercapacitors will be able to perform in terms of both high specific power density and high specific energy density.

There are attempts to increase both the power density and energy density of supercapacitors by using various forms of sp^2 carbon like carbon nanotube, activated carbons, mesoporous carbon, graphene etc. [5-12]. However, the current applications of carbon based supercapacitors are still limited by their low energy density regime. Activated carbons, due to high surface area and porosity show typical capacitances up to 300 F/g in aqueous electrolytes or 120 F/g in organic electrolytes but at low discharge rates [5, 13]. However, their storage performance decreases radically at high discharge rates. On the other hand, carbon nanotubes in spite of having excellent electronic conductivity due to low surface areas provide low specific capacitances of less than 100 F/g in aqueous electrolytes or less than 50 F/g in organic electrolytes [5, 14]. There are reports on the synthesis of various carbon morphologies like carbon nanoparticles, carbon nanofibers etc. which have been investigated for supercapacitor application, but there performance is still not fully encouraging [15, 16]. With the unique electronic properties of graphene there are numerous reports on applications of graphene and its variants as anode materials in ECs. Only graphene typically shows the specific capacitance value in the range from 100 to 200 F/g, which renders it one of the potential candidates as anode material in the supercapacitors [5-8]. But like Carbon nanotubes, amorphous carbon and mesoporous carbon there are not many reliable methods for synthesis of graphene on truly large scale. Today graphene can be synthesized by different methods such as micromechanical cleavage, sonication in various solvents, chemical reduction of graphite oxide (GO), pyrolysis of polymers or organic materials, thermal decomposition of SiC or chemical vapour deposition etc. [17-26]. But the majority of work in supercapacitors has been dominated by the as-synthesized or modified variants of chemically converted graphene (CCG). This is due to the fact that in methods other than chemical reduction of GO, the yield of graphene is very low. Chemical synthesis involves Liquid exfoliation and reduction of GO which produces graphene in large quantities, but the method involves use of toxic chemicals. Other than this there are reports for the template assisted synthesis of microporous or mesoporous graphene [27-29]. Due to large surface area of these porous graphenes they find applications not only in energy storage but also in gas storage, gas sensing etc. [30-32]. But these methods are once again not simple for large scale synthesis. Also it is difficult to corrugate 2D material like graphene into 3D microporous or mesoporous structure; there is no reliable bottom-up or top-down approach for the large-scale production of porous graphene. In order to develop high performance supercapacitors, one therefore needs to seek newer approaches to obtain highly conducting graphene with microporosity and very high surface area.

In this work it is demonstrated the one-step catalyst-free synthesis of Single-layer-graphene-assembled porous carbon (SLGAPC) by polymer pyrolysis route. The polymer poly (4-styrenesulfonic acid-co-maleic acid) sodium salt (PSSCMA) is pyrolized in argon atmosphere at 1000^0C for 4 hours. This pyrolized product then washed for purification, filtered and dried in air. The carbon mass obtained was examined for the structural, chemical and morphological properties using various techniques. The surface area of as synthesized SLGAPC is found to be 1720 m^2/g. This SLGAPC is tested for supercapacitor application and shows high capacitance value of ~154 F/g in aqueous electrolyte in a typical electrochemical cell. We believe that high surface area with hierarchically porous architecture makes SLGAPC potential candidate as anode material in supercapacitor and or batteries. Hexagonal pores and conductive graphitic framework together provide a large double layer area, fast ion transport and efficient charge harvesting in aqueous electrolytes.

4.2 Experimental Section

The poly (4-styrenesulfonic acid-co-maleic acid) sodium salt was obtained from Sigma Aldrich (Mol wt 20,000). For pyrolytic decomposition, the polymer was heat treated in a furnace at 1000^0C for 4 hours in argon atmosphere. The product formed by pyrolysis of polymer was then washed and purified carefully with D.I. water to remove the inorganic by-products. This process was repeated till the pH of carbon mass dispersed in water became neutral. This carbon mass then dried subsequently and examined for the structural, chemical and morphological properties using various techniques such as X-ray diffraction (XRD, Philips X'Pert PRO), Raman spectroscopy (Confocal micro-Raman spectrometer LabRAM ARAMIS Horiba Jobin-Yvon apparatus with laser excitation wavelength of 532 nm), high resolution transmission electron microscopy (HRTEM, FEI Tecnai 300) and field emission scanning electron microscopy (FESEM, Hitachi S-4200). The surface area and porosity study were performed by the standard nitrogen adsorption (BET method) isotherm at 77K. Electrochemical measurements were performed with Autolab PGSTAT Potentiostat. Specific capacitance of SLGAPC was determined by cyclic voltammetry (CV) measurements in 1 M H_2SO_4.

4.3 Results and Discussion

Figure 4.1a shows the SEM image of SLGAPC structure, which confirms presence of well ordered and uniform pores. Figure 1b-d shows the TEM images of SLGAPC which clearly show its highly porous nature.

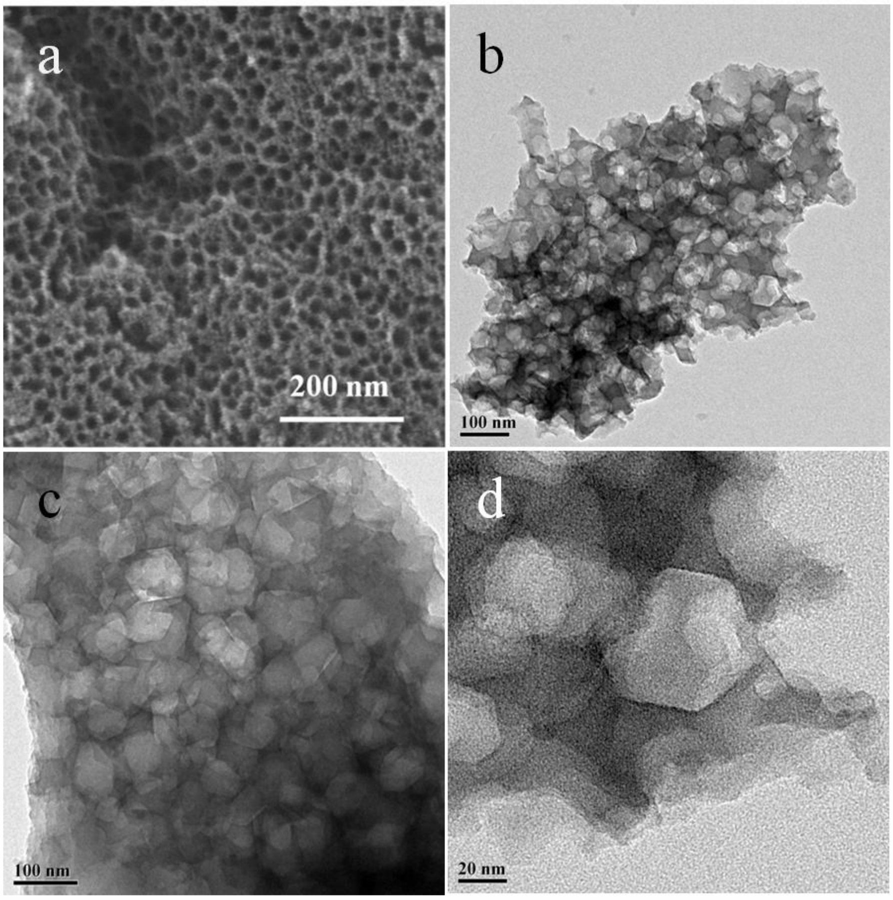

Fig. 4.1 *a) SEM and b–d) TEM images of graphene based SLGAPC*

The morphology is well-defined with hexagonal nanopores of uniform size and shape. The mean length of the edges of hexagonal pores is 30±10 nm, with a very few pores having edge length of more than 40 nm. The walls of pores are nothing but the graphene sheets which are interconnected to each other. It is interesting to discuss the possible mechanism for formation of SLGAPC by simple pyrolysis of polymer. In this context it is important to mention that polystyrene based polymers are known to generate porous carbon morphologies but of amorphous nature [33, 34].

In our case, it's the specific choice of the polymer with strictly controlled pyrolysis parameters such as gas flow during pyrolysis, temperature of pyrolysis and duration of heating which together lead to successful synthesis of meso-microporous graphene. PSSCMA which we have used as a precursor for the synthesis of SLGAPC is a copolymer of styrene sulfonate and maleic acid unit (see schematic 1a). Maleic acid units undergo inter-chain cyclization on pyrolysis to form extended graphene structures as shown in schematic 1b. On the other hand polystyrene sulfonate part of the copolymer decomposes during pyrolysis leaving behind graphene sheets with sp^3 carbon end. These sheets then bind with each other by sp^3 carbon ends to form the observed hierarchical porous structure with hexagonal pores (see schematic 1c).

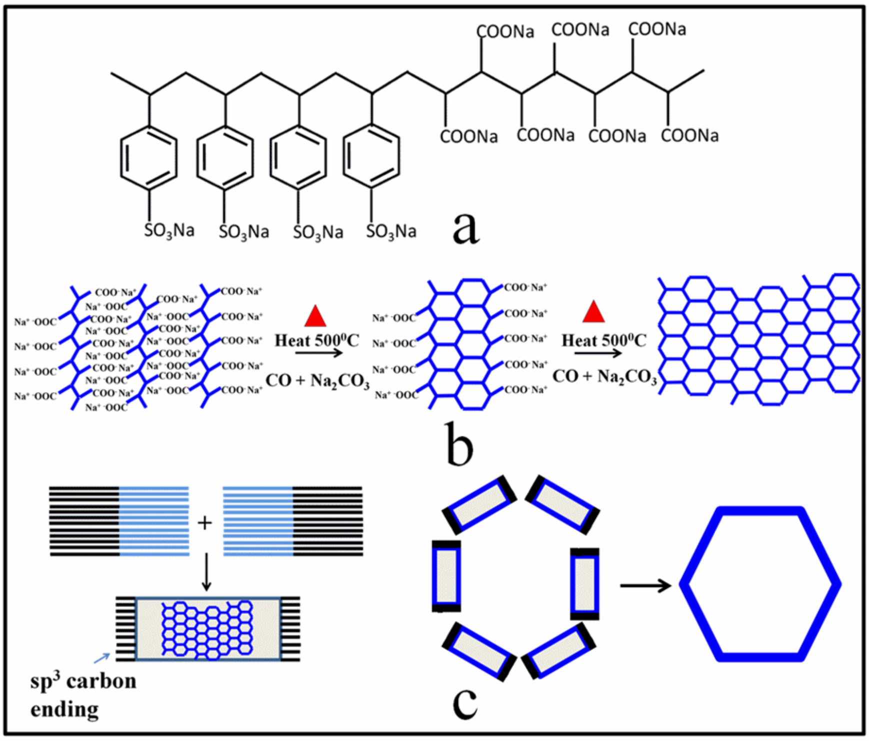

Scheme 4.1 *(a) structure of polymer PSSCMA (b) inter-chain cyclization between maleic acid unit of PSSCMA to form graphene sheet (c) formation of hexagonal pores from graphene sheets.*

Figure 4.2a shows the XRD spectrum of SLGAPC. The broad peak at 2 theta value of around 24^0 confirms that the graphene formed is not multilayer and there is no stacking of graphene sheets on the top of each other. Single layer graphene does not show graphitic d-spacing that is present in MWCNT, graphite etc. Multilayer graphene has the d-spacing of 0.34 nm as that in graphite which then shows a relatively sharp peak at around 2 theta value of 26^0 in the XRD spectrum. This confirms the presence of single layer graphene in the porous architecture.

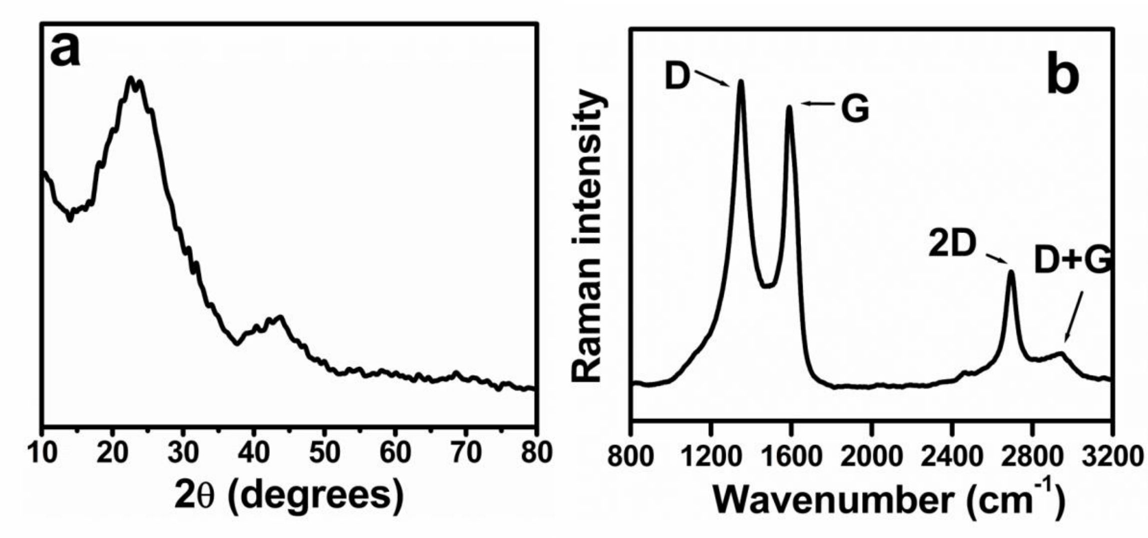

Fig. 4.2 *(a) XRD and (b) Raman spectrum of SLGAPC*

As it is well known that, Raman spectroscopy is the most powerful technique to distinguish between different forms of carbons such as graphene, CNT, graphite or non-graphitic amorphous carbon etc. [35-41]. Indeed, the same technique can unequivocally bring out the presence of single, double or multilayer graphene in a sample through a careful analysis of the related spectral parameters. Figure 4.2b shows the Raman spectrum of SLGAPC. The Raman spectrum of our porous graphene shows the presence of the fairly sharp signature peak at 1585 cm^{-1} which corresponds to the G band. It is to be noted that generally this peak is present at 1580 cm^{-1} in the case of graphite, CNTs, graphene and amorphous carbon. As in the case of many forms of graphitic carbons (e.g. CNTs, chemically converted graphene or CCG and amorphous carbon) the presence of D band peak at about 1345 cm^{-1} in our sample also signifies presence of defects. Also it is known that an increase in defect density causes upward shift of the G peak (e.g. from ~1580 cm^{-1} to 1585 cm^{-1}) as seen. But presence of G and D bands alone does not confirm presence of graphene uniquely. On the other hand, high quality graphene is characterized uniquely by the presence of G' or 2D peak, which appears at 2700 cm^{-1} in the Raman spectrum. The 2D peak is due to the Raman vibration of the second order of zone-boundary phonons which satisfy the Raman fundamental selection rules in the case of single layer graphene, but not in the case of graphite or multi-layer graphene.

No.	Reference (data for single layer graphene with green laser (514, 538 nm) excitation for Raman spectroscopy)	Position of G peak (cm^{-1})	Position of 2D peak (cm^{-1})	FWHM of 2D peak (cm^{-1})
1.	Raman Spectrum of Graphene and Graphene Layers by Geim *et. al. Phys. Rev. lett.* **2006**, *97*, 187401	~1580	~2700	~25
2.	G' band Raman spectra of single, double and triple layer graphene by Dresselhaus *et. al. Carbon*, **2009**, *47*, 1303	-	~2700	18-28
3.	Spatially Resolved Raman Spectroscopy of Single- and Few-Layer Graphene D. Graf *et. al. Nano Lett.*, **2007**, *7*, 238	~1582	~2700	30
4.	Raman fingerprint of charged impurities in graphene A. C. Ferrari *et. al. Appl. Phys. Lett.*, 2007, 91, 233108	1560-1580	~2700	28-30
5.	Temperature Dependence of the Raman Spectra of Graphene and Graphene Multilayers by A. A. Balandin et. al. *Nano Lett.*, **2007**, *7*, 2645	~1582	2691 (488 nm laser)	-
6.	Freestanding Graphene by Thermal Splitting of Silicon Carbide Granules by X. Bao *et. al. Adv. Mater.* **2010**, *22*, 2168	~1585	~2700	-
7.	Raman spectroscopy of graphene and graphite: Disorder, electron–phonon coupling, doping and nonadiabatic effects by A. C. Ferrari *Solid State Commun.*, 2007, **143**, 47	~1580	~2700	~25
8.	Our work (SLGAPC)	1585	2696	50

No of graphene layers	Position of 2D peak (cm^{-1})	FWHM of 2D peak (cm^{-1})
1	~2700±5	20-30
2	~2710	30-55
3	~2715	more than 60
Our work (SLGAPC)	2696	50

***Table 4.1** Tables of referenced Raman parameters for single layer graphene*

Hence this peak is present in the Raman spectrum of single layer graphene and absent in that of graphite, multi-layer (>10 layer) graphene or amorphous carbon. Presence of sharp signature peak corresponding to 2D band at 2700 cm^{-1} in the case of our sample strongly supports the presence of single layer graphene assembled configuration. Now, it is useful to further emphasize that Raman spectroscopy can also be used to distinguish between single layer, bilayer to few layer graphene. The position of this 2D peak as well as broadening or FWHM decides the character of graphene. In this regard, many authors (e.g. Geim et. al., Dresselhaus et. al., Ferrari et. al. etc. [35-37, 42-46]. have discussed the effect of thickness of graphene sheets on the position, FWHM and intensity of 2D band peak. They have also discussed the relationship between the energy of laser used for excitation in Raman studies with the position, FWHM and intensity of the 2D band peak. According to these studies, for the case of green excitation wavelength (λ =514 nm or λ =538 nm) the peak position of 2D band is around ~ 2700 cm^{-1} in the case of single sheet graphene and this peak shifts to higher wavenumber as the thickness of graphene increases from 1 layer to n layer graphene or graphite up to 2750 cm^{-1}. For the case of red excitation wavelength (λ = 633 nm) the position of 2D band lies at ~ 2650 cm^{-1} in the case of single sheet graphene and shifts to higher wavenumber as the thickness of graphene increases from 1 layer to n layer up to 2700 cm^{-1}. In our sample, with green excitation wavelength (λ=514 nm), the 2D peak is located around ~2696 cm^{-1}, clearly indicating primarily the presence of single sheet graphene. We have compared the peak position of 2D peak of our sample with the values reported in the literature on single layer graphene. Notably hardly any shift is found in the 2D peak as compared to the data from literature (see Table 4.1). The FWHM in our case is slightly broader (50 cm^{-1}) as compared to that for the case of single layer graphene reported by others (30 cm^{-1}). This can be attributed to the folding edge strains in our 3D architecture and related defects. It should be emphasized that these reports are mostly for large area graphene sheets (thin films on support material like Si) while our sample represents graphene sheets folded into 3D nanoscale architecture.

We also performed x-ray photoelectron spectroscopy study on our sample and compared the same with chemically converted graphene (CCG). These data are presented as figure 4.3. Brielfy, the C1s contribution in the XPS clearly shows the C-C (sp^2 carbon) bond peak present at 284.5 eV [47, 48]. Interestingly, in the case of our single-layer-graphene-assembled porous carbon (SLGAPC) the peak is much sharper as compared to that of CCG. This is due to fact that CCG is synthesized by reduction of graphite oxide in a typical reduction process. In this process some oxygen functional groups remain unaffected and are not reduced fully to remove oxygen from the graphene. In our case we are heating the precursor polymer (PSSCMA) at high temperature (1000^0C) in argon (inert atmosphere) which renders very minimal oxygen functional groups attached to the graphene, leading to a sharp C1s peak. This signifies the carbon purity of the material as well as similar chemical character for most carbons in the material.

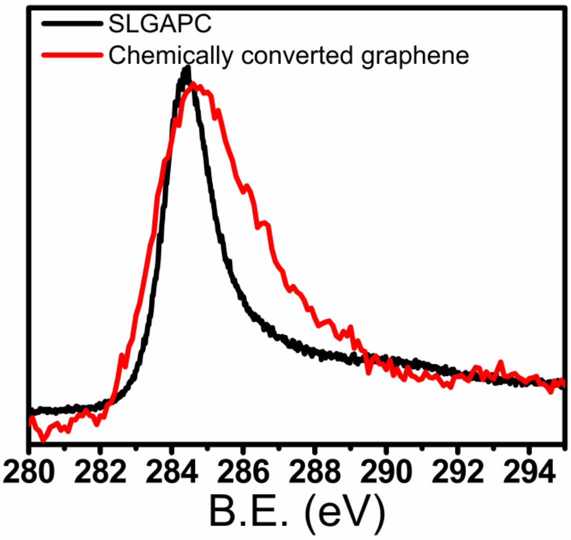

Fig. 4.3 *XPS spectra of our sample (SLGAPC) compared to that for chemically converted graphene*

The surface area and porosity of the as-prepared SLGAPC were measured by nitrogen adsorption-desorption method at 77 K. The surface area is found to be extremely high, ~1720 m^2/g.

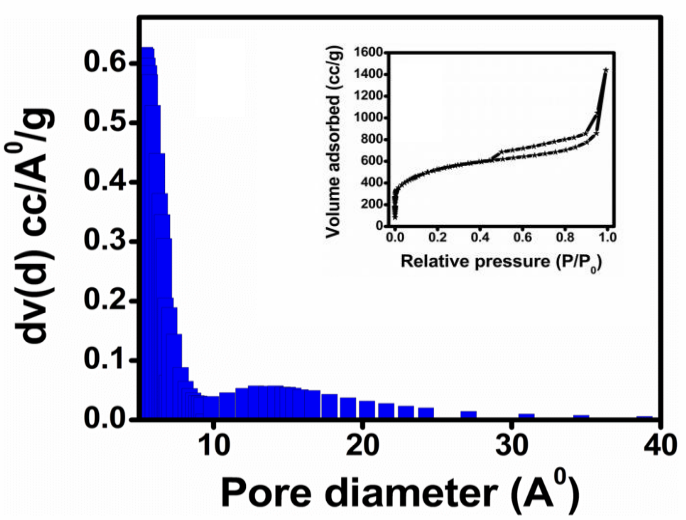

Fig. 4.4 *Pore size distribution of SLGAPC and inset shows N2 adsorption–desorption isotherm of SLGAPC*

Figure 4.4 shows the pore size distribution which shows that the average pore diameter is less than 1 nm indicating microporous nature [49]. Figure 3b shows the Nitrogen adsorption-desorption isotherm of SLGAPC which exhibits type II isotherm, indicating multilayer adsorption at high P/P0 value with small but prominent hysteresis behaviour [50]. Sorption analysis at low P/P0 values indicates the microporous nature and displays pronounced pore filling (up to 1400 cc/g) at high relative pressures. It indicates that SLGAPC have hexagonal nanoporous architecture in combination with microporous structure.

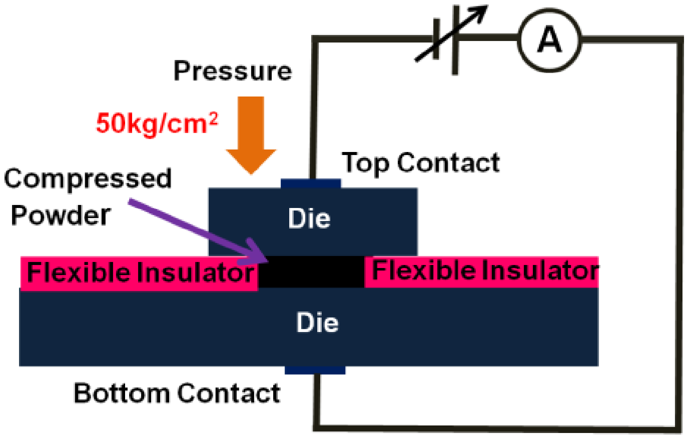

***Scheme 4.2** Schematic diagram of resistivity measurement process*

We measured the resistivity of SLGAPC by two probe method. It is very difficult to make a mechanically strong pellet out of SLGAPC powder for conductivity measurements, therefore the powder was placed in a die and a known (50 kg/m2) pressure was applied. The contact was made from both the sides of the die, and the top and bottom parts of the die were separated by a flexible insulator to avoid contact, as shown by a schematic 2. The resistivity was calculated by knowing the dimension parameters of dye and thickness of material. The resistivity of our sample was found to be about 0.044 Ω-m. The specific conductivity calculated from this value comes around to be 23 S/m, indicating highly conducting nature of the SLGAPC.

We explored the SLGAPC sample for supercapacitor application due to its conducting nature together with its very high surface area. Figure 4 shows the supercapacitor performance or electrochemical characteristics of SLGAPC. The Cyclic voltammetry (CV) measurements were performed by varying the scanning rates between 20 and 200 mV/s with a potential window of 1.0 V. Figure 4a shows the typical cyclc voltammetric response of SLGAPC recorded in 1M H_2SO_4 solution. The

CV curves exhibit a pure rectangular shape without any redox peaks (oxidation or reduction) with strong capacitive behaviour which indicates efficient charge storage with fast ion transport in aqueous electrolytes.

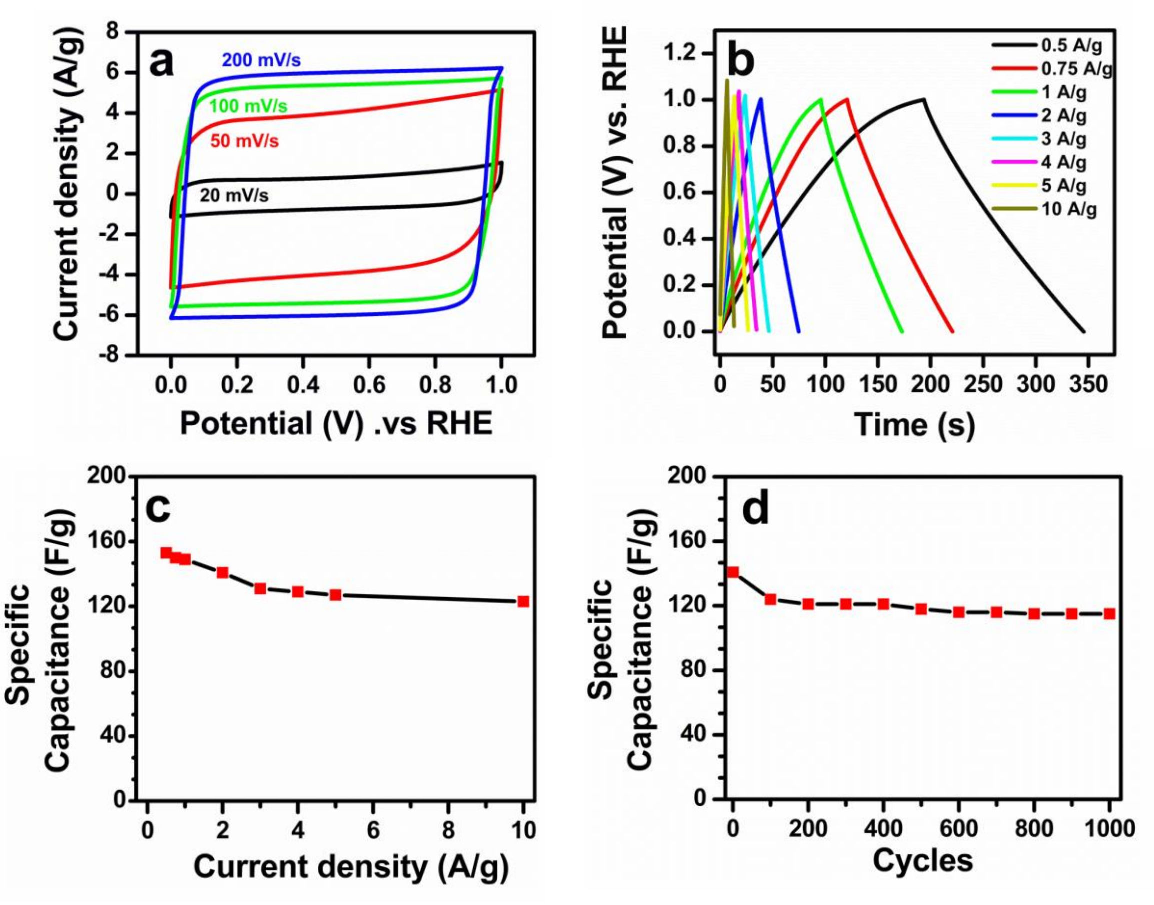

Fig. 4.5 *(a) CV curves of SLGAPC at different scan rates ranging from 20 to 200 mV/s (b) Charge-discharge curve of SLGAPC (c) Specific capacitance value at different current densities ranging from 0.5 to 10 A/g and (d) stability study of capacitance of SLGAPC till 1000 cycles*

The shape of curve remains purely rectangular even at high scan rate of 100 and 200 mV/s. This indicates that the hierarchically ordered SLGAPC structure possesses significantly lower resistance for ion transport during high-rate charge and discharge processes. The CV performance at high scan rate establishes the high power capability of SLGAPC. Also the rectangular CV shape represents a nearly perfect electrical double layer formation (reversible adsorption and desorption of the ions) across the surface of the carbon, which is a testimony to the high specific surface area and microporous character of the material. The rectangular nature of the CV curve maintained at very high scan rate implies the perfect double layer formation even at high scan rate which is may be attributed with the large hexagonal nanopores (mesopores) as well as the micropores present in the system. Large mesopores help to transport the ions whereas the micropores help for the formation electric double layers. The accurate value of specific capacitance for the two electrode system was calculated from the galvanostatic charge discharge values by using the following equation:

$$Cs = \frac{2\,I\,\frac{dt}{dv}}{m}$$

Where Cs is the specific capacitance (F/g), I is current, m is the active mass and (dv/dt) is the slope obtained from the discharge curve [51]. The charge-discharge plots at different current densities ranging from 0.5A/g to 10A/g are shown in Figure 4b, while the graph of specific capacitance vs. current density is plotted in Figure 4c. The highest specific capacitance value 154 F/g is obtained at a current density of 0.5A/g. Also it is clear from the graph that as the current density increases the specific capacitance value slightly decreases which is due to the limited diffusion of the active ions on the electrode surface for very high scan rates. Interestingly even at a high current density of 10 A/g the specific capacitance value is 123 F/g. The stability testing was also done up to 1000 cycles at current density of 2 A/g (Figure 4d). It shows that till 500 cycles there is a little drop in capacitance value, but after 500 cycles capacitance value is steady and remains constant.

4.4 Conclusion

We have successfully synthesized porous graphene with hexagonal nonopores. It is a catalyst-free synthesis leading to single-layer-graphene-assembled carbon without use of any template. The as-synthesized sample exhibits high surface area of about 1720 m^2/g and shows bulk specific conductivity of 23 S/m. The material exhibits excellent supercapacitance performance in aqueous medium with maximum specific capacitance of 154 F/g at a current density of 0.5 A/g. It also shows good stability at higher current densities and after 1000 charge discharge cycles without any apparent sign of decay rate even for further cycling.

4.5 Refferences

[1] A, Arico, P. Bruce, B. Scrosati, J. Tarascon, W. Schalkwij, *Nature Mater.* **2005**, *4*, 366 – 377.

[2] P. Hall, E. Bain, *Energy Policy* **2008**, *36*, 4352–4355.

[3] L. L. Zhang, X. S. Zhao, *Chem. Soc. Rev.* **2009**, *38*, 2520–2531.

[4] Y. Zhu, S. Murali, M. Stoller, K. Ganesh, W. Cai, P. Ferreira, A. Pirkle, R. Wallace, K. Cychosz, M. Thommes, D. Su, E. Stach, R. Ruoff, *Science* **2011**, *332*, 1537-1541.

[5] L. L. Zhang, R. Zhou, X. S. Zhao, *J. Mater. Chem.* **2010**, *20*, 5983–5992.

[6] Y. Wang, Z. Shi, Y. Huang, Y. Ma, C. Wang, M. Chen, Y. Chen, *J. Phys. Chem. C,* **2009**, *113*, 13103–13107.

[7] M. Stoller, S. Park, Y. Zhu, J. An, R. Ruoff, *Nano Lett.* **2008**, *8*, 3498-3502.

[8] Y. Zhu, S. Murali, W. Cai, X. Li, J. Suk, J. Potts, R. Ruoff, *Adv. Mater.* **2010**, *22*, 3906–3924.

[9] E. Frackowiak, F. Beguin *Carbon* **2001**, *39*, 937–950.

[10] M. Kaempgen, C. Chan, J. Ma, Y. Cui, G. Gruner, *Nano Lett.* **2009**, *9*, 1872-1876.

[11] S. Prabaharan, R. Vimala, Z. Zainal, *Journal of Power Sources* **2006**, *161*, 730–736.

[12] V. Ruiz, C. Blanco, R. Santamaria, J. Ramos-Fernandez, M. Martinez-Escandell, A. Sepulveda-Escribano, F. Rodrıguez-Reinoso, *Carbon* **2009**, *47*, 195-200.

[13] Z. Chen, D. Weng, H. Sohn, M. Cai, Y. Lu, *RSC Adv.*, **2012**, *2*, 1755–1758.

[14] M. Kaempgen, J. Ma, G. Gruner, G. Wee, S. G. Mhaisalkar, *Appl. Phys. Lett.* **2007**, *90*, 264104.

[15] C. Merino, P. Soto, E. Vilaplana-Ortego, J. Salazar, F. Pico, J. Rojo, *Carbon* **2005**, *43*, 551–557.

[16] C. Kim, *Journal of Power Sources* **2005**, *142*, 382–388.

[17] A. Geim, *Science* **2009**, *324*, 1530–1534.

[18] M. Choucair, P. Thordarson, J. Stride, *Nature Nanotech.* **2009**, *4*, 30-33.

[19] S. Byun, H. Lim, G. Shin, T. Han, S. Oh, J. Ahn, H. Choi, T. Lee. *J. Phys. Chem. Lett.* **2011**, *2*, 493–497.

[20] D. Wei, Y. Liu, *Adv. Mater.* **2010**, *22*, 3225–3241.

[21] M. Allen, V. Tung, R. Kaner, *Chem. Rev.* **2010**, *110*, 132–145.

[22] S. Park, R. Ruoff, *Nature Nanotech.* **2009**, *4*, 217–224.

[23] X. Zhou, Z. Liu, A. Scalable, *Chem. Commun.* **2010**, *46*, 2611-2613.

[24] K. Emtsev, *Nature Mater.* **2009**, *8*, 203–207.

[25] A. Reina, X, Jia, J. Ho, D. Nezich, H. Son, V. Bulovic, M. Dresselhaus, J. Kong, *Nano Lett.* **2009**, *9*, 30–35.

[26] Z. Sun, Z. Yan, J. Yao, E. Beitler, Y. Zhu, J. Tour, *Nature* **2010**, *468*, 549–552.

[27] B. Choi, M. Yang, W. Hong, J. Choi, Y. Huh, *ACS Nano* **2012**.

[28] S. Lee, H. Kim, J. Hwang, W. Lee, J. Kwon, C. Bielawski, R. Ruoff, S. Kim, *Angew. Chem. Int. Ed.* **2010**, *49*, 10084 –10088.

[29] D. Fan, Y. Liu, J. He, Y. Zhoua, Y. Yang. *J. Mater. Chem.* **2012**, *22*, 1396-1402.

[30] G. Ning, C. Xu, L. Mu, G. Chen, G. Wang, J. Gao, Z. Fan, W. Qian, F. Wei, *Chem. Commun.* **2012**, *48*, 6815-6817.

[31] F. Yavari, Z. Chen, A. V. Thomas, W. Ren, H. Cheng, N. Koratkar, *Sci. Rep.* **2011**, *1*, 116.

[32] D. Jiang, V. Cooper, S. Dai. *Nano Lett.* **2009**, *9*, 4019-4024.

[33] H. Hines, A. Bagreev, T. Bandosz, *Langmuir* **2004**, *20*, 3388-3397.

[34] J. Neely, *Carbon* **1980**, *19*, 21-36.

[35] A. C. Ferrari, J. C. Meyer, V. Scardaci, C. Casiraghi, M. Lazzeri, F. Mauri, S. Piscanec, D. Jiang, K. S. Novoselov, S. Roth, A. K. Geim, *Phys. Rev. lett*. **2006**, *97*, 187401.

[36] D. Graf, F. Molitor, K. Ensslin. C. Stampfer, A. Jungen, C. Hierold, *Nano Lett.* **2007**, *7*, 238-242.

[37] C. Casiraghi, S. Pisana, k. Novoselov, A. Geim, A. Ferrari, *Appl Phys Lett.* **2007**, *91*, 233108.

[38] M. Dresselhaus, G. Dresselhaus, R. Saito, A. Jorio, *Physics Reports* **2007**, *409*, 47-99.

[39] H. Zhou, C, Qiu, H. Yang, F. Yu, M. Chen, L. Hu, *Chemical Physics Letters* **2011**, *501*, 475-479.

[40] L. Liu, S. Ryu, M. Tomasik, E. Stolyarova, N. Jung, M. Hybertsen, *Nano Lett.* **2008**, *8*, 1965-1970.

[41] K. Kudin, B. Ozbas, H. Schniepp, R. Prudhomme, I. Aksay, R. Car, *Nano Lett.* **2008**, *8*, 36-41.

[42] J.S. Park, A. Reina, R. Saito, J. Kong, G. Dresselhaus, M.S. Dresselhaus, *Carbon*, **2009**, *47*, 1303-1310.

[43] I. Calizo, A. A. Balandin, W. Bao, F. Miao, C. N. Lau, *Nano Lett.*, **2007**, *7*, 2645-2649.

[44] D. Deng, X. Pan, H. Zhang, Q. Fu, D. Tan, X. Bao, *Adv. Mater.* **2010**, *22*, 2168-2171.

[45] A. C. Ferrari *Solid State Commun*., **2007**, *143*, 47-57.

[46] Y. Y. Wang, Z. H. Ni, T. Yu, Z. X. Shen, H. M. Wang, Y. H. Wu, W. Chen, A. T. S. Wee, *J. Phys. Chem. C.*, **2008**, *112*, 10637–10640.

[47] H. D. Pham, V. H. Pham, T. V. Cuong, T. D. Nguyen-Phan, J. S. Chung, E. W. Shin, S. Kim, *Chem. Commun.*, **2011**, *47*, 9672–9674.

[48] D. Zhan, Z. Ni, W. Chen, L. Sun, Z. Luo, L. Lai, T. Yu, A. T. S. Wee, Z. Shen, *Carbon*, **2011**, *49*, 1362-1366.

[49] C. Zhou, S. Kumar, C. Doyle, J. Tour, *Chem. Mater*. **2005**, *17*, 1997-2002.

[50] A. Adamson, A. Gast, *Physical Chemistry of Surfaces. Sixth Edition, John Wiley & Sons, Inc.* **1997**.

[51] A. Dale, C. Brownson, C. Banks, *Chem. Commun.* **2012**, *48*, 1425-1427.

Chapter V

Large area Single Layer Graphene by Pyrolysis of Polymer for a) Supercapacitor Application and b) Graphene-P3HT Composite for Field-Effect Transistor Application

This chapter discusses the synthesis, properties and applications of large area single layer graphene. Graphene is synthesized from pyrolysis of poly (acrylic acid) sodium salt. This method represents a facile approach to large area single layer graphene. The process is catalyst/template free. It is simple bottom-up process by which large amounts of graphene can be synthesized in single batch requiring no specialized chemicals. The method is scalable and establishes a new and easy approach to fabricate micron size sheets of graphene. The as synthesized graphene is highly conducting in nature with specific conductivity of 100 S/m and also exhibits extremely high surface area which is 350 m^2/g. The as synthesized graphene shows excellent properties for supercapacitor application. The graphene synthesized by this method was also composited with P3HT and characterized for field-effect transistor application.

Section-I: Large size single layer graphene by pyrolysis of polymer for supercapacitor application

5-I.1 Introduction

Graphene is a one atom-thick planar sheet of sp^2-bonded carbon atoms that are densely packed in a honeycomb crystal lattice. It is also the basic structural unit of some carbon allotropes including graphite, charcoal, carbon nanotubes and fullerenes. Graphene has some unique physicochemical properties such as excellent electrical, thermal conductivity, high surface area and optical transparency etc. [1-3]. The electrical conductivity of graphene is highest as compared to any other material on earth. Electrons moving in graphene behave as massless Dirac fermions which renders remarkably high electron mobility in graphene at room temperature [4, 5] Graphene bilayer acts as field-effect transistor where the band gap of graphene can be tuned from 0 to 0.25 eV, by applying voltage to a dual-gate bilayer graphene at room temperature [6]. The single layer graphene can have very high surface area of around 2630 m^2g^{-1}[7]. These properties render graphene various functionalities which are important in several fields such as supercapacitors, Li-ion batteries, photovoltaics, sensor, nanoelectronics etc. [1, 8-17]

There are very limited methods for the synthesis of graphene which include micromechanical cleavage, sonication in various solvents, chemical reduction of graphite oxide (GO), pyrolysis of polymers or organic materials, thermal decomposition of SiC and chemical vapour deposition etc. [18-27] In micromechanical cleavage method graphene layers are peeled off from graphite. Chemical reduction method involves the reduction of graphite oxide (GO) to graphene by suitable reducing agent such as hydrazine hydrate. Chemical vapour deposition involves epitaxial growth of graphene on suitable substrate such as silicon carbide at high temperature. Pyrolysis is also a unique method to synthesize graphene wherein the organic precursors such as sugar, sodium ethoxide, or suitable polymers such as PMMA, PAN, PS etc. are thermally decomposed in presence of catalysts at high temperature in an inert atmosphere. Out of these methods CVD is very expensive, micromechanical cleavage method is not useful for bulk production of graphene, and chemical exfoliation method involves use of toxic and hazardous chemicals. So in comparison with these methods, pyrolysis has several advantages. It is one step method where large scale production of graphene is possible with or without presence of catalyst (depends upon the choice of precursor). It does not involve use of toxic materials and chemicals for synthesis.

In this workthe catalyst free synthesis of graphene by pyrolysis route is demonstrated. Briefly the polymer poly (acrylic acid) sodium salt (Mol Wt 5000) is pyrolized in argon atmosphere at 1000^0C for 4 hours. This pyrolized product was washed for purification, filtered and dried in air. The carbon mass obtained was examined for the structural, chemical and morphological properties using various techniques. The surface area of as synthesized graphene was found to be 350 m^2/g, which is significant from the application point of view. The specific conductivity of this graphene was nearly 90 S/m. The as synthesized graphene was stested for supercapacitor application and shows high capacitance value of ~130 F/g when tested in *aqueous electrolyte* in a typical electrochemical cell. The high surface area with conductive graphitic framework together provide a large double layer area, fast ion transport and efficient charge harvesting in aqueous electrolytes.

5-I.2 Experimental Section

The poly (acrylic acid) sodium salt was obtained from Sigma Aldrich (Mol wt 5,000). For pyrolytic decomposition, the polymer was heated in a furnace at 1000^0C for 2 hours in argon atmosphere. The product formed by pyrolysis of polymer was then washed and purified carefully with D.I. water to remove the inorganic by-products. This process was repeated till the pH of carbon mass dispersed in water became neutral. This carbon mass then dried subsequently and examined for the structural, chemical and morphological properties using various techniques such as X-ray diffraction (XRD, Philips X’Pert PRO), Raman spectroscopy (Confocal micro-Raman spectrometer LabRAM ARAMIS Horiba Jobin-Yvon apparatus with laser excitation wavelength of 532 nm), high resolution transmission electron microscopy (HRTEM, FEI Tecnai 300) and field emission scanning electron microscopy (FESEM, Hitachi S-4200). The surface area and porosity study were performed by the standard nitrogen adsorption (BET method) isotherm at 77K. Electrochemical measurements were performed with Autolab PGSTAT Potentiostat. Specific capacitance of graphene was determined by cyclic voltammetry (CV) measurements in 1 M H_2SO_4.

5-I.3 Results and Discussion

Figure 5.1 shows the TEM image of as synthesized carbon mass. It shows presence of graphene sheets which has size of few microns. The graphene sheet shows a typical wrinkled morphology with presence of numerous folding. It resembles the crumpled silk veil wave structure which is characteristic of 2D geometry of graphene. High resolution TEM confirms the presence of monolayer graphene with high transparency. Inset of figure 5.1d shows the selected area electron diffraction pattern taken for graphene. The SAED pattern is relatively diffused, due to the folded structure of graphene sheet which do not hold perpendicular to the electron beam.

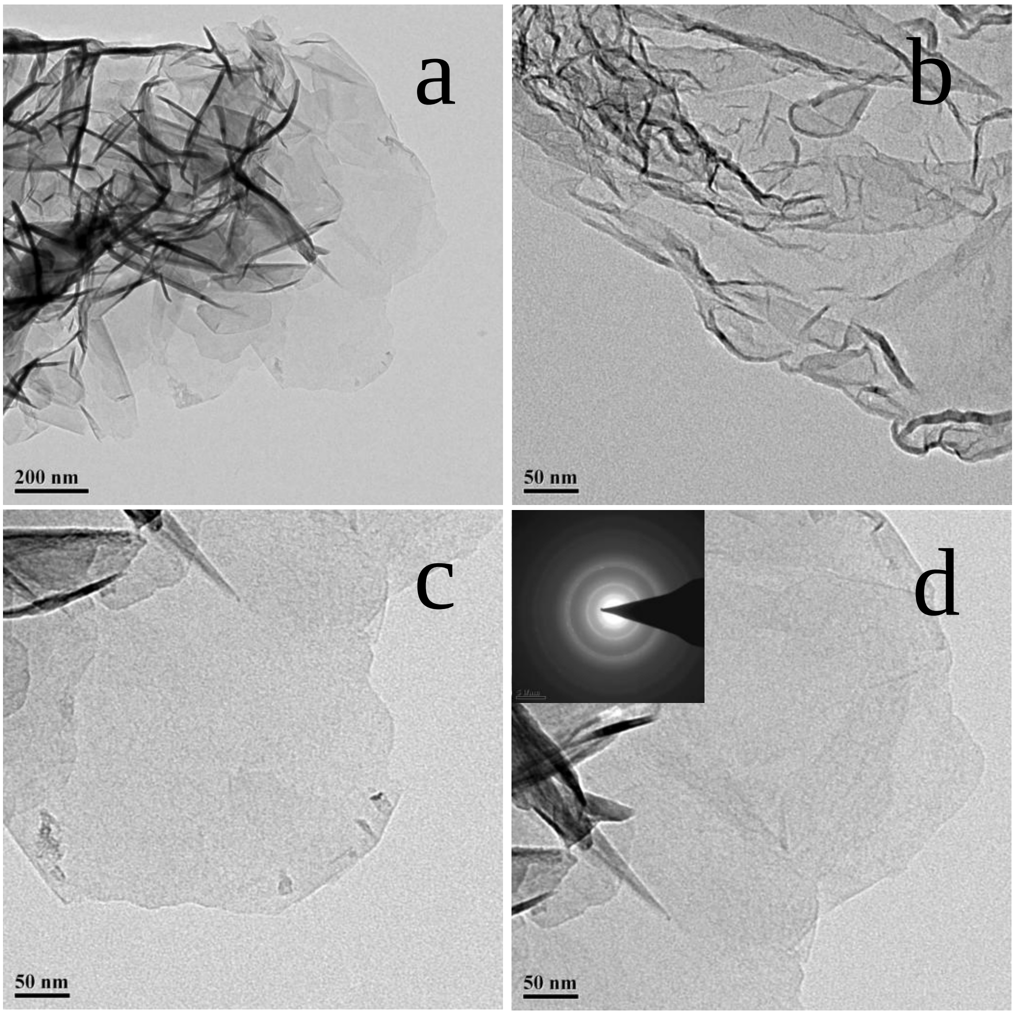

Fig. 5.1 *TEM images of Graphene*

Figure 5.2 shows the XRD spectrum and Raman spectrum of as synthesized graphene. The presence of characteristic graphitic peak at around 26° in the XRD spectrum confirms the presence of graphene sheets which are stacked above one another when it is in the powder form. The peak is very broad confirming the presence of few layer graphene. It is expected to get this peak in the XRD spectrum, as pure high quality graphene sheets attract each other due to van der walls forces. graphene sheets, which can come closer due to attractive forces amongst them in order to minimize the surface energy. Hence when the bulk quantity of dispersed graphene sheets is dried by removing solvent these sheets again come closer by van der walls forces and gives characteristic peak at 26^0 in the XRD spectrum.

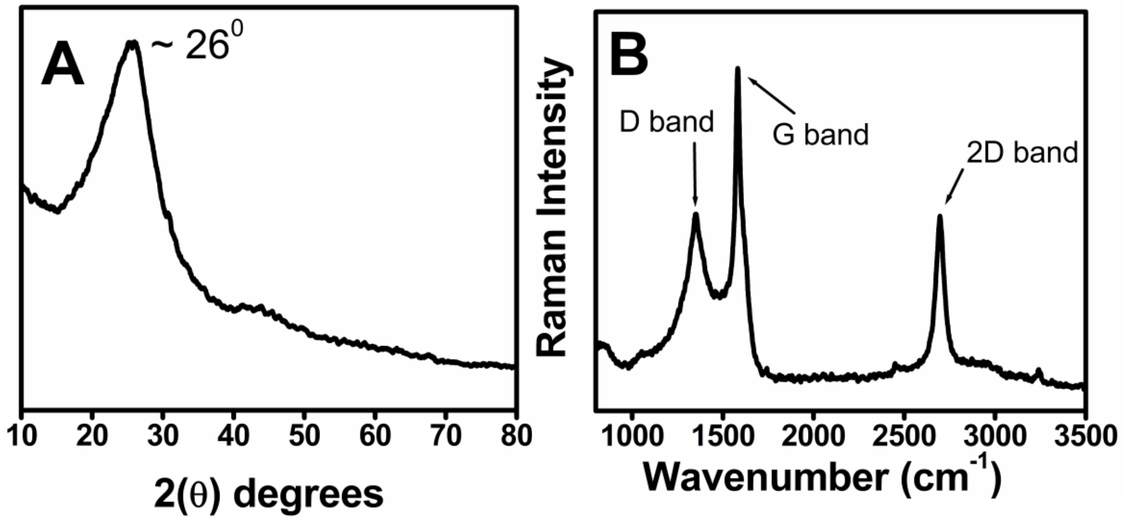

Fig. 5.2 *A) XRD spectrum and B) Raman spectrum of graphene*

Raman spectroscopy was further used to characterize the graphene sample. Raman spectroscopy is generally employed to distinguish between different forms of graphitic carbon such as graphene, CNT, graphite or non-graphitic amorphous carbon etc. It also useful for the diferentiation between single, double and multiple layered graphen [28-34]. Figure 5.2B shows the Raman spectrum of as synthesized graphene. The signature peak present at 1585 cm^{-1} in the Raman spectrum of graphene corresponds to the G band. Generally this peak is present at 1580 cm^{-1} in the case of graphite, CNTs, graphene and amorphous carbon. Presence of D band peak at about 1345 cm^{-1} in case of graphene signifies disordered nature (defects) of the graphite like system. This peak is usually present in CNTs, chemically converted graphene (CCG) and amorphous carbon. Also it can be noted that the intensity ratio I_D/I_G is about 0.6 which signifies presence of fewer defect in the graphene. The high quality graphene is characterized by the presence of G’ or 2D peak which appears at 2700 cm^{-1} in the Raman spectrum.

No.	Reference (data for single layer graphene with green laser (514, 538 nm) excitation for Raman spectroscopy)	Position of G peak (cm^{-1})	Position of 2D peak (cm^{-1})	FWHM of 2D peak (cm^{-1})
1.	Raman Spectrum of Graphene and Graphene Layers by Geim *et. al. Phys. Rev. lett.* **2006**, *97,* 187401	~1580	~2700	~25
2.	G' band Raman spectra of single, double and triple layer graphene by Dresselhaus *et. al. Carbon*, **2009**, *47*, 1303	-	~2700	18-28
3.	Spatially Resolved Raman Spectroscopy of Single- and Few-Layer Graphene D. Graf *et. al. Nano Lett.*, **2007**, *7*, 238	~1582	~2700	30
4.	Raman fingerprint of charged impurities in graphene A. C. Ferrari *et. al. Appl. Phys. Lett.*, 2007, 91, 233108	1560-1580	~2700	28-30
5.	Temperature Dependence of the Raman Spectra of Graphene and Graphene Multilayers by A. A. Balandin et. al. *Nano Lett.*, **2007**, *7*, 2645	~1582	2691 (488 nm laser)	-
6.	Freestanding Graphene by Thermal Splitting of Silicon Carbide Granules by X. Bao *et. al. Adv. Mater.* **2010**, *22*, 2168	~1585	~2700	-
7.	Raman spectroscopy of graphene and graphite: Disorder, electron–phonon coupling, doping and nonadiabatic effects by A. C. Ferrari *Solid State Commun.*, 2007, **143**, 47	~1580	~2700	~25
8.	Our work (large size single sheet graphene)	1585	2696	51

No of graphene layers	Position of 2D peak (cm^{-1})	FWHM of 2D peak (cm^{-1})
1	~2700±5	20-30
2	~2710	30-55
3	~2715	more than 60
Our work (large size single sheet graphene)	2696	51

***Table 5.1** Tables of referenced Raman parameters for single layer graphene*

The 2D peak is due to the Raman vibration of second order of zone-boundary phonons which satisfy the Raman fundamental selection rules in case of single layer graphene but not in case of graphite or multi-layer graphene. So this peak is present in the Raman spectrum of single layer graphene and absent in that of graphite, multi-layer graphene and amorphous carbon. Presence of sharp signature peak corresponding to 2D band at 2700 cm^{-1} in the case of our graphene then signifies the presence of single layer graphene. Also the intensity of 2D peak is equal to or slightly more than that of D peak indicating highly crystalline nature of the as synthesized graphene.

Raman spectroscopy can also be used to distinguish between single layer, bilayer to few layer graphene. Especially careful analysis of 2D peak in Raman spectra can assure the quality of graphene. The positions of 2D peak as well as its broadening or FWHM are the important parameters that decide nature of graphene. In this regard, many authors have addressed the effect of thickness of graphene sheets on the position, FWHM and intensity of 2D band peak [28-30, 35-39]. Also it should be emphasized that the position, FWHM and intensity of the 2D band peak also depends upon the energy of laser used for excitation in Raman studies. According to these studies, single sheet graphene shows the presence of 2D band at around ~ 2700 cm^{-1} for the case of green excitation wavelength (λ =514 nm or λ =538 nm) and this peak shifts to higher wavenumber as the thickness of graphene increases from 1 layer to n layer graphene or graphite up to 2750 cm^{-1}. For the case of red excitation wavelength (λ = 633 nm) the position of 2D band lies at ~ 2650 cm^{-1} in the case of single sheet graphene and shifts to higher wavenumber as the thickness of graphene increases from 1 layer to n layer up to 2700 cm^{-1}. In our sample, with green excitation wavelength (λ=514 nm), the 2D peak is located around ~2696 cm^{-1}, clearly indicating primarily the presence of single sheet graphene. In table 5.1 the peak position of 2D peak of our sample with the values reported in the literature on single layer graphene is compared. Notably any shift is found in the 2D peak as compared to the data from literature as shown below in table 5.1. The FWHM in our case is slightly broader (51 cm^{-1}) as compared to that for the case of single layer graphene reported by others (30 cm^{-1}). This can be attributed to the folding edge strains and related defects in the graphene. It should be emphasized that these reports are mostly for large area graphene sheets (thin films on support material like Si) while our sample represents graphene sheets without support.

The surface area and porosity of the graphene were measured by nitrogen adsorption-desorption method at 77 K. The surface area is found to be significantly high, ~350 m^2/g. Figure 3Ashows the pore size distribution of as synthesized graphene. It indicates the average pore diameter of graphene is less than 1 nm which indicates microporous nature [40]. Figure 3B shows the Nitrogen adsorption-desorption isotherm of graphene. It exhibits type II isotherm which is characteristic of multilayer adsorption at high P/P$_0$ value [41]. Also it shows small but prominent hysteresis behavior.

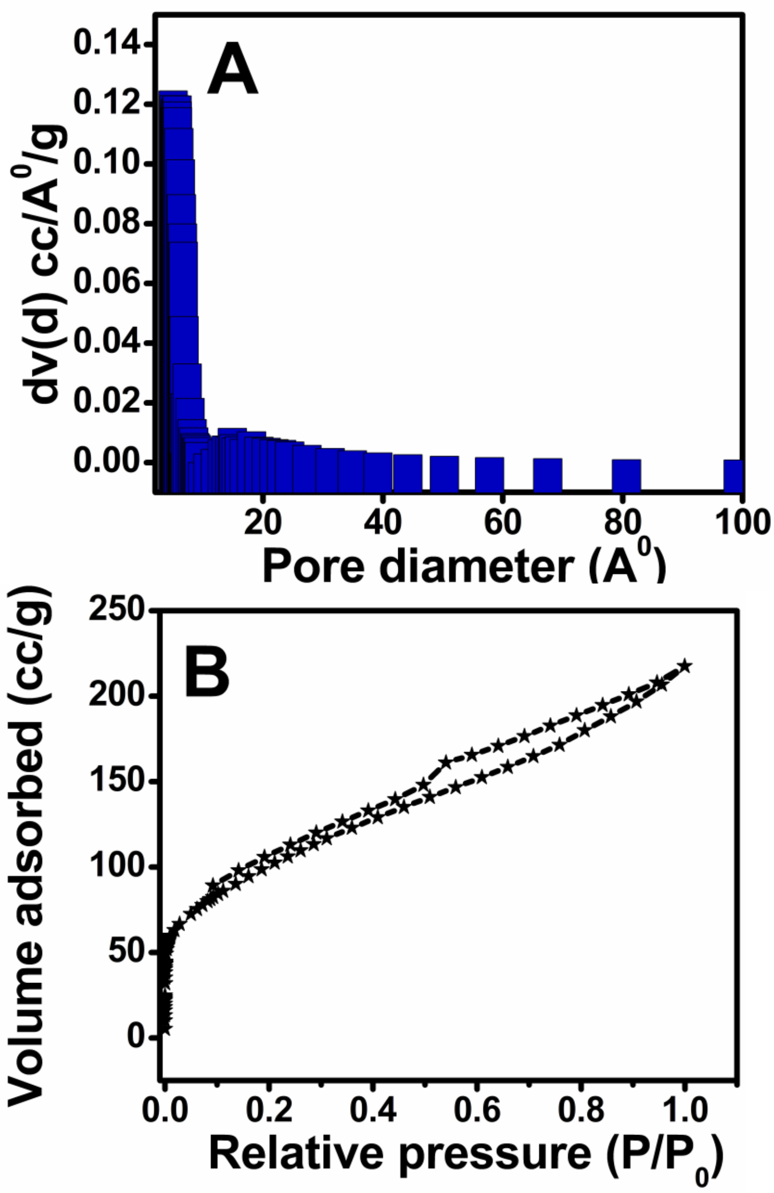

Fig. 5.3 *A) Porosity data and B) N_2 isotherm of graphene at measured at 77 K.*

The resistivity of graphene is measured by two probe method. It is very difficult to make a mechanically strong pellet out of graphene powder for conductivity measurements, therefore the powder was placed in a die and a known (50 kg/m^2) pressure was applied. The contact was made from both the sides of the die, and the top and bottom parts of the die were separated by a flexible insulator to avoid contact. The resistivity was calculated by knowing the dimension parameters of dye and thickness of material.

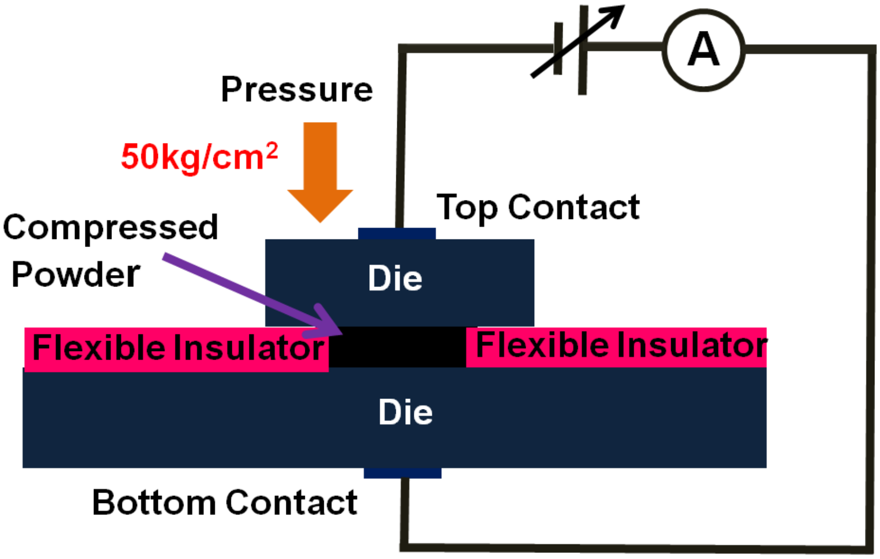

Fig. 5.4 *Schematic of conductivity measurement assembly*

The resistivity of our sample was found to be ~0.011 Ω-m. The specific conductivity calculated from this value comes around to be 90 S/m, indicating highly conducting nature of the graphene.

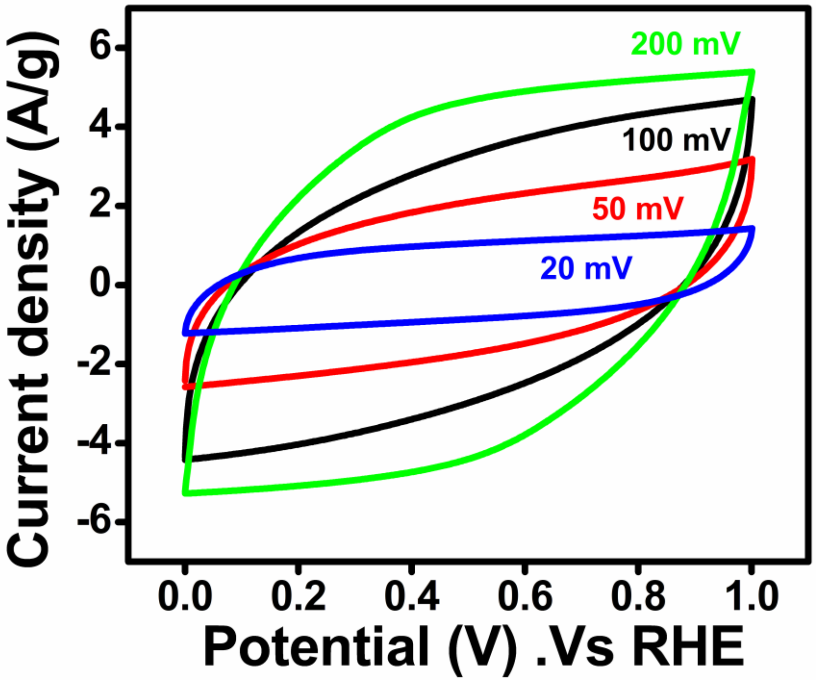

Fig. 5.5 *CV curves of graphene at different scan rates*

Figure 5.5 shows the typical cyclic voltammetric response of graphene recorded in 1M H_2SO_4 solution. The CV curves exhibit a slightly skewed rectangular shape without any redox peaks (oxidation or reduction). The shape of curve becomes skewed but remains nearly rectangular even at high scan rate of 100 and 200 mV/s. This indicates that the graphene possesses significantly lower resistance for ion transport during high-rate charge and discharge processes. The average value of capacitance from CV curves is about 130 F/g.

5-I.4 Conclusion

This section demonstrates catalyst free synthesis of large area single layer graphenewithout use of any template. The as-synthesized graphene exhibits fairly high surface area of about 350 m^2/g and shows bulk specific conductivity of 90 S/m. This graphene also shows good CV behaviour with approximate specific capacitance of 130 F/g.

Section-II:Graphene-P3HT composite for Field-effect transistor application

5-II.1 Introduction

Graphene has some unique physicochemical properties such as excellent electrical, thermal conductivity, high surface area and optical transparency etc. as discussed in previous section. Due to these properties graphene has attracted attention of scientist for a range of applications, such as as electrode material in supercapacitors, batteries displays, solar cells, and sensors [1-17] On the other hand organic and polymeric semiconductors offer potential low-cost, high-volume manufacturing of flexible transistor-based electronics, such as display drivers, radio frequency identification tags, pressure mapping elements, and chemical sensors etc. [42-49]. Today other than silicon based transistors, organic and polymeric semiconductors based transistors exhibit high on/off ratios in organic field-effect transistors. But these OFETs suffer from low mobility’s that limit the range of possible applications [50-54]. In this case it is interesting to see that graphene is a new 2D material which posses very high electron mobility can be an ideal candidate for a transistor material with gigahertz or terahertz of working frequency. Although poor on/off ratios of graphene based devices is the major hurdle in the development of FETs made so far. Also in case of OFETs the need for higher mobility organic semiconductors is still compelling, especially for materials used in conjunction with solution processes. The new alternative to this problem involve the use of both organic semiconductor materials together with carbon-based materials such as graphene and carbon nanotubes (CNTs) etc. which exhibit very high mobility. This approach enhances the effective mobility while keeps the on/off ratio sufficiently high in the device. This strategy also significantly enhances the charge injection/extraction across the electrode/organic semiconductor interface. This is due to highly conductive charge-transporting layer between the electrode and the active semiconductor layer. [55]

In this regard there are few reports for the use of organic semiconductor/carbon nanotube hybrid field-effect transistors [56–61] where inclusion of CNT with organic semiconductor results in remarkable increase in apparent field-effect mobility. Further it is indicated that CNTs act as conducting bridges between the crystalline regions of the semiconductor film thereby increasing the mobility. However, at the same time the on/off ratio appears to decrease just as the mobility begins to increase. This is because one dimensional carbon nanotubes has a percolation threshold when mixed with organic semiconductor. At low density of CNTs, the mobility of the organic semiconductor film increases drastically, but as the density of the CNTs appears to approach the percolation threshold, the on/off ratio is observed to decrease. With graphene, due to the single atom two-dimensional lattice, it is expected to have better electronic, mechanical and physical properties that will improve FET operation. It is expected that addition of graphene will provide good connection between the crystalline regions of the semiconductor film. Also compared to CNTs, increased area in the conduction channel of an organic semiconductor transistor can be covered by graphene before they start to percolate and reduce the on/off ratio. As a result, the mobility of organic transistors with graphene would be expected to show higher values than what can be accomplished using CNTs before device on/off ratio drops. In this regard there are very few reports for the use of organic semiconductor/graphene composite material as a channel material for FET based device applications. Hence this is very attractive area of research for the preparation of new generation devices based on graphene/organic semiconductor hybrid.

In this work, a general approach for the preparation of solution processable organic semiconductor/graphene hybrid thin film transistors is presented. In this method, graphene was synthesized by pyrolysis of poly (acrylic acid) sodium salt. The method is a catalyst free and cost effective. The as prepared organic semiconductor/graphene hybrid thin film transistor shows their efficient working. It is seen that as compared to FETs with pure organic semiconductors, hybrid FETs exhibit much higher effective mobility while keeping the on/off ratio of devices sufficiently high.

5-II.2Experimental Section

The graphene was synthesized by pyrolysis of poly (acrylic acid) sodium salt, as explained in the previous section. In this work, poly-(3-hexylthiophene) (P3HT), an organic semiconductor was blended with this as synthesized graphene in dichlorobenzene (DCB) and spin coated on Si/SiO_2 substrate having gold electrodes. A7w/w% graphene/P3HT composite was used to prepare the channel material of FET. The required graphene dispersion was made in P3HT solution of fixed molarity. This solution was then subjected to ultrasonic agitation and. This yielded a dark-purple solution with polymer nanoparticles and graphene suspended in DCB. A heavily doped silicon wafer with 300 nm thermally grown SiO_2 was used as a substrate material.

Wafers were cleaned by sonication in acetone, isopropanol and DI water, respectively, followed by N_2 drying. Hybrid field-effect transistors were fabricated by spin coating the P3HT/graphene composite solution onto a substrate at 1400 rpm for 60 s followed by vacuum drying to give 20–50-nm thick semiconductor layer. Control devices were fabricated with pure P3HT films using the same procedures but without the addition of graphene to the DCB solution. Gold source-drain electrodes were pre-deposited prior to spin coating with channel length L = 20 μm and channel width W= 1 mm. All of the resulting devices were annealed in a vacuum oven at 110^0C for 20 min, followed by slow cooling. All the current–voltage (I–V) curves were measured at room temperature under ambient conditions using a Cascade probe station connected to two Keithley 2400 source/measure units. The effective field-effect mobility of each transistor was extracted from the transfer characteristics using a linear fit to the plot of the square root of saturation source-drain current as a function of the gate voltage Vg.

5-II.3 Results and discussion

All the characterization for graphene is presented in previous section of same chapter. Here the application part of graphene/P3HT composite has only discussed. Graphene has high electron mobility, hence when incorporated into an organic semiconductor film, provides ‘‘fast lanes’’ for charge carriers within the conduction channel. Thus it enhances the effective mobility of the entire transistor device thereby reduces the conduction channel length, which acts to enhance the output source-drain current of the field-effect transistor.

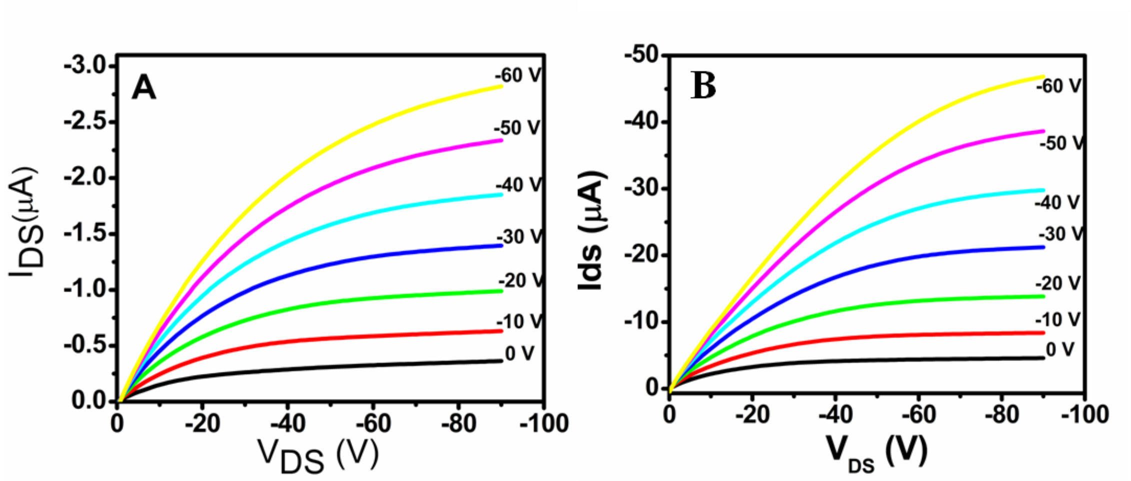

Fig. 5.6 *Output characteristics of A) pure P3HT, B) 7% graphene/P3HT FET devices.*

To compare the results only P3HT was also spin coated on silicon wafer having pre-deposited gold electrodes and studied for their transistor characteristic. The results are summaries in a table given in figure 5.8, which confirms the enhancement in the performance of transistors made from P3HT/graphene hybrid. The measured current–voltage characteristics for P3HT/graphene FETs show well-defined gate modulation.

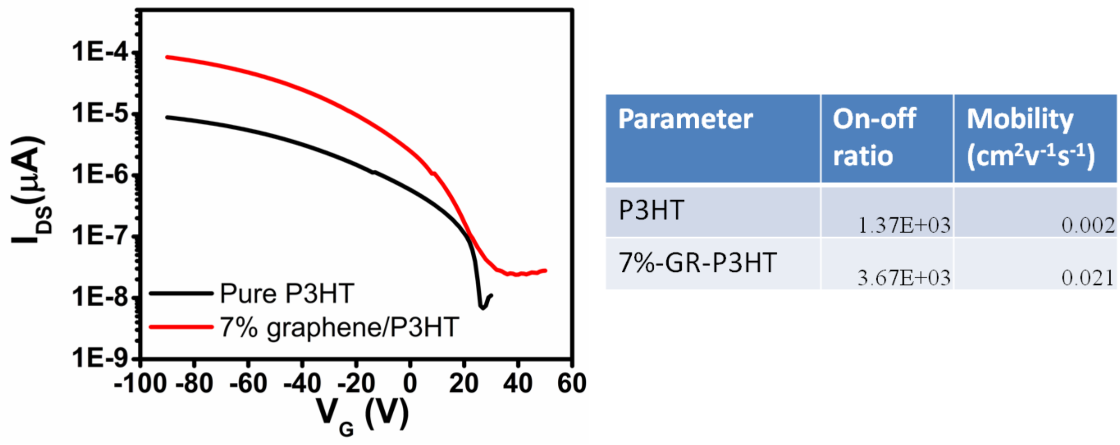

Parameter	On-off ratio	Mobility ($cm^2v^{-1}s^{-1}$)
P3HT	1.37E+03	0.002
7%-GR-P3HT	3.67E+03	0.021

Fig. 5.7 *Transfer characteristics of pure P3HT and 7% graphene/P3HT FET devices and respective on/off ratios and mobility values.*

Figure 5.6 depicts the current–voltage characteristics of pure P3HT as well as graphene/P3HT hybrid transistor, and Figure 5.7 compares the transfer characteristics of the same graphene/P3HT hybrid transistor to that of a pure P3HT transistor. It should be noted that much higher current was obtained from the device with graphene/P3HT device. In the case of 7% graphene/P3HT device the mobility is increase by one order (0.02 cm^2 $V^{-1}s^{-1}$) as compared to that from the pure P3HT FET (0.002 cm^2 $V^{-1}s^{-1}$). The on/off ratio of the 7% graphene/P3HT FET is nearly thrice that of the pure P3HT FET.

5-II.4 Conclusion

In conclusion, this section demonstrates a new way of synthesizing graphene/P3HT composite and its application for field effect transistors. It is shown that effective mobility as well as on/off ratio of polymer/graphene hybrid FETs can be significantly higher than that of a pure polymer FET. The mobility of graphen/P3HT FET device is found to be 0.02 cm^2 $V^{-1}s^{-1}$ which is one order higher as compared to only P3HT FET device. The on/off ratio of the graphene/P3HT FET device is also found to be nearly thrice that of the pure P3HT FET device.

5.2 References

[1] A. K. Geim, K. S. Novoselov, *Nat. Mater*., **2007**, *6*, 183.

[2] K. S. Novoselov, A. K. Geim, S. V. Morozov, D. Jiang, M. I. Katsnelson, I. V. Grigorieva, S. V. Dubonos, A. A. Firsov, *Nature*, **2005**, *438*, 197.

[3] Y. B. Zhang, Y. W. Tan, H. L. Stormer and P. Kim, *Nature*, **2005**, *438*, 201.

[4] A. H. Castro Neto, F. Guinea, N. M. R. Peres, K. S. Novoselov, A. K. Geim, *Rev. Mod. Phys*., **2009**, *81*, 109.

[5] K. S. Novoselov, A. K. Geim, S. V. Morozov, D. Jiang, Y. Zhang, S. V. Dubonos, I. V. Grigorieva, A. A. Firsov, *Science*, **2004**, *306*, 666.

[6] Y. Zhang, *Nature*, **2009**, *459*, 820.

[7] A. Peigney, C.Laurent, E. Flahaut, R. R. Bacsa, A. Rousset, *Carbon*, **2001**, *39*, 507.

[8] A, Arico, P. Bruce, B. Scrosati, J. Tarascon, W. Schalkwij, *Nature Mater.* **2005**, *4*, 366 – 377.

[9] P. Hall, E. Bain, *Energy Policy* **2008**, *36*, 4352–4355.

[10] L. L. Zhang, X. S. Zhao, *Chem. Soc. Rev.* **2009**, *38*, 2520–2531.

[11] Y. Zhu, S. Murali, M. Stoller, K. Ganesh, W. Cai, P. Ferreira, A. Pirkle, R. Wallace, K. Cychosz, M. Thommes, D. Su, E. Stach, R. Ruoff, *Science* **2011**, *332*, 1537-1541.

[12] L. L. Zhang, R. Zhou, X. S. Zhao, *J. Mater. Chem.* **2010**, *20*, 5983–5992.

[13] S.Bae, H. Kim, Y. Lee, X. F. Xu, J. S. Park, Y. Zheng, J. Balakrishnan, T. Lei, H. R. Kim, Y. I. Song,Y .J .Kim, K. S. Kim, B. Ozyilmaz, J. H. Ahn, B. H. Hong, S. Iijima, *Nature Nanotechnology*, **2010**, *5*, 574.

[14] X. Wang, L. Zhi, K. Mullen, *Nano Letters*, **2008**, *8*, 323.

[15] J. Wu, M. Agrawal, H. A. Becerril, Z. Bao, Z. Liu, Y. Chen, P. Peumans, *ACS nano*, **2009**, *4*, 43.

[16] F. Bonaccorso, Z. Sun, T. Hasan, A. C. Ferrari, *Nature Photonics*, **2010**, *4*, 611.

[17] F. Schedin, A. K. Geim, S. V. Morozov, E. W. Hill, P. Blake, M. I. Katsnelson, K. S. Novoselov, *Nature Materials*, **2007**, *6*, 652.

[18] A. Geim, *Science* **2009**, *324*, 1530–1534.

[19] M. Choucair, P. Thordarson, J. Stride, *Nature Nanotech.* **2009**, *4*, 30-33.

[20] S. Byun, H. Lim, G. Shin, T. Han, S. Oh, J. Ahn, H. Choi, T. Lee. *J. Phys. Chem. Lett.* **2011**, *2*, 493–497.

[21] D. Wei, Y. Liu, *Adv. Mater.* **2010**, *22*, 3225–3241.

[22] M. Allen, V. Tung, R. Kaner, *Chem. Rev.* **2010**, *110*, 132–145.

[23] S. Park, R. Ruoff, *Nature Nanotech.* **2009**, *4*, 217–224.

[24] X. Zhou, Z. Liu, A. Scalable, *Chem. Commun.* **2010**, *46*, 2611-2613.

[25] K. Emtsev, *Nature Mater.* **2009**, *8*, 203–207.

[26] A. Reina, X, Jia, J. Ho, D. Nezich, H. Son, V. Bulovic, M. Dresselhaus, J. Kong, *Nano Lett.* **2009**, *9*, 30–35.

[27] Z. Sun, Z. Yan, J. Yao, E. Beitler, Y. Zhu, J. Tour, *Nature* **2010**, *468*, 549–552.

[28] A. C. Ferrari, J. C. Meyer, V. Scardaci, C. Casiraghi, M. Lazzeri, F. Mauri, S. Piscanec, D. Jiang, K. S. Novoselov, S. Roth, A. K. Geim, *Phys. Rev. lett*. **2006**, *97*, 187401.

[29] D. Graf, F. Molitor, K. Ensslin. C. Stampfer, A. Jungen, C. Hierold, *Nano Lett.* **2007**, *7*, 238-242.

[30] C. Casiraghi, S. Pisana, k. Novoselov, A. Geim, A. Ferrari, *Appl Phys Lett.* **2007**, *91*, 233108.

[31] M. Dresselhaus, G. Dresselhaus, R. Saito, A. Jorio, *Physics Reports* **2007**, *409*, 47-99.

[32] H. Zhou, C, Qiu, H. Yang, F. Yu, M. Chen, L. Hu, *Chemical Physics Letters* **2011**, *501*, 475-479.

[33] L. Liu, S. Ryu, M. Tomasik, E. Stolyarova, N. Jung, M. Hybertsen, *Nano Lett.* **2008**, *8*, 1965-1970.

[34] K. Kudin, B. Ozbas, H. Schniepp, R. Prudhomme, I. Aksay, R. Car, *Nano Lett.* **2008**, *8*, 36-41.

[35] J.S. Park, A. Reina, R. Saito, J. Kong, G. Dresselhaus, M.S. Dresselhaus, *Carbon*, **2009**, *47*, 1303-1310.

[36] I. Calizo, A. A. Balandin, W. Bao, F. Miao, C. N. Lau, *Nano Lett.*, **2007**, *7*, 2645-2649.

[37] D. Deng, X. Pan, H. Zhang, Q. Fu, D. Tan, X. Bao, *Adv. Mater.* **2010**, *22*, 2168-2171.

[38] A. C. Ferrari *Solid State Commun*., **2007**, *143*, 47-57.

[39] Y. Y. Wang, Z. H. Ni, T. Yu, Z. X. Shen, H. M. Wang, Y. H. Wu, W. Chen, A. T. S. Wee, *J. Phys. Chem. C.*, **2008**, *112*, 10637–10640.

[40] C. Zhou, S. Kumar, C. Doyle, J. Tour, *Chem. Mater*. **2005**, *17*, 1997-2002.

[41] A. Adamson, A. Gast, *Physical Chemistry of Surfaces. Sixth Edition, John Wiley & Sons, Inc.* **1997**.

[42] S. E. Burns, K. Reynolds, W. Reeves, M. Banach, T. Brown, K. Jacobs, A. Menon, S. Siddique, P. Too, C. Ramsdale, J. Watts, P. Cain, T. Werne, J. Mills, C. Curling, H. Sirringhaus, K. Amindson, M. D. McCreary, *J. Soc. Inf. Display*, **2005**, *13*, 583.

[43] T. W. Kelley, P. F. Baude, C. Gerlach, D. E. Ender, D. Muyres, M. A. Haase, D. E. Vogel, S. D. Theiss, *Chem. Mater.*, **2004**, *16*, 4413.

[44] J. Huang, J. Miragliotta, A. Becknell, H. E. Katz, *J. Am. Chem. Soc.*, **2007**, *129*, 9366.

[45] T. Someya, A. Dodabalapur, J. Huang, K.C. See, H. E. Katz, *Adv. Mater.*, **2010**, *22*, 3799.

[46] J. Huang, T. J. Dawidcyk, B. J. Jung, J. Sun, A. F. Mason, H. E. Katz, *J. Mater. Chem.*, **2010**, *20*, 2644.

[46] H. E. Katz, J. Huang, *Annu. Rev. Mater. Res.*, **2009**, *39*, 71.

[48] J. Huang, J. Sun, H. E. Katz, *Adv. Mater.*, **2008**, *20*, 2567.

[49] R. Parashkov, E. Becker, T. Riedel, H. H. Johannes, W. Kowalsky, *Proc. IEEE*, **2005**, *93*, 1321.

[50] M. S. Fuhrer, B. M. Kim, T. Durkop, T. Brintlinger, *Nano Lett*, **2002**, *2*, 755.

[51] E. S. Snow, J. P. Novak, P. M. Campbell, D. Park, Appl. Phys. Lett. **2003**, *82*, 145.

[52] X. Z. Bo, C. Y. Lee, M. S. Strano, M. Goldfinger, C. Nuckolls, G.B. Blanchet, *Appl. Phys. Lett.* **2005**, *86*, 182102.

[53] X. Z. Bo, N. G. Tassi, C. Y. Lee, M. S. Strano, C. Nuckolls, G. B. Blanchet, *Appl. Phys. Lett.*, **2005**, *87*, 203510.

[54] J. X. Geng, B. S. Kong, S. B. Yang, S. C. Youn, S. Park, T. Joo, H. T. Jung, *Adv. Funct. Mater.*, **2008**, *18*, 2659.

[55] K. Walzer , B. Maennig , M. Pfeiffer , K. Leo , *Chem. Rev.* **2007** , *107* , 1233 .

[56] X. Z. Bo, C. Y. Lee, M. S. Strano, M. Goldfinger, C. Nuckolls, G. B. Blanchet, *Appl. Phys. Lett.*, ***2005***, *86*, 182102.

[57] X. Z. Bo, N. G. Tassi, C. Y. Lee, M. S. Strano, C. Nuckolls, G. B. Blanchet, *Appl. Phys. Lett.*, **2005**, *87*, 203510.

[58] J. X. Geng, B. S. Kong, S. B. Yang, S. C. Youn, S. Park, T. Joo, H. T. Jung, *Adv. Funct. Mater.*, **2008**, *18*, 2659.

[59] S. Liu, S. C. B. Mannsfeld, M. C. LeMieux, H. W. Lee, Z. Bao, *Appl. Phys. Lett.*, **2008**, *92*, 053306.

[60] Y. D. Park, J. A. Lim, Y. Jang, M. Hwang, H. S. Lee, D. H. Lee, H. J. Lee, J. B. Baek, K. Cho, *Org. Electron.*, **2008**, *9*, 317.

[61] G. W. Hsieh, F. M. Li, P. Beecher, A. Nathan, Y. Wu, B. S. Ong, W. I. Milne, *J. Appl. Phys.*, **2009**, *106*, 123706.

………………

CHAPTER VI

Transformation of ZnO Nanoplates into Carbon Coated ZnO nanorods for enhanced Visible light photocatalysis

This chapter discusses the synthesis, properties and applications of carbon coated ZnO. This is achieved by using poly (acrylic acid-co-maleic acid) sodium salt as a coating during the synthesis of ZnO nanoplates by solution phase reaction. Polymer assisted growth of ZnO is anisotropic and looks like a popcorn ball structure with feature size varying from 1-4 microns. The polymer coated ZnO nanoplates are then annealed in air at 500^0C for 2 hours to obtain carbon coated ZnO nanoroads. The carbon coated ZnO nanoroads gives excellent photocatalytic activity in the visible region. It is also resistant to degradation by and scavenging of the dye without hindrance to charge transfer which is significant for optical applications.

6.1 Introduction

Synthesis of carbon composites of transition metal oxide is a technologically important area of research. The properties of these hybrid composites are superior to either metal oxide or carbon. Also the metal oxide carbon composites have unique opto-electronic properties and applications which may not be found in oxide or carbon alone such as visible light photocatalysis [1-4]. Apart from this carbon based metal oxide composites are also attractive for various applications involving supercapacitor, battery, etc. [5, 6], thus having a large scope of research. In this context, there are many reports for the synthesis of carbon composites especially carbon composites of metal oxides such as TiO_2, ZnO, Mn_3O_4, SnO_2, NiO etc. for several applications [2, 3, 7, 8] Among these, carbon composites of ZnO are relatively well studied in the context of their properties and applications. This is due to the fact that ZnO has several advantages over other metal oxides due to its superior optical, electrical, photoconductivity, piezoelectric and sensor properties [9]. It is also easy to tailor morphology of the ZnO-carbon composites due to easy and controlled growth of ZnO. Also ZnO is known to exhibit faceted growth along some crystal planes leading to more ordered structure. There are numerous reports on the synthesis of well-defined ZnO nanostructures such as nanorods, nanosheets, nanotubes, nanobelts, nanoflower, nanocables etc. [10-18]. Along with these structures, there have been reports for the successful synthesis of more complicated hierarchical structures of ZnO such as microspheres of self assembled ZnO nanorods, hollow spheres of ZnO etc. [19, 20]. But apart from the design and controlled fabrication of ZnO nanostructure of definitive size and shape, it is also important to impart the functional properties to these nanostructures. Hence synthesis of ZnO-carbon composites with hierarchical structures serves the better strategy for introducing new properties in ZnO nanostructures while keeping their size and shape related properties intact.

In this regard, there are several reports for the synthesis of ZnO-carbon composite by different routes [1-4, 21]. Among these, polymer assisted synthesis of a nanostructure or a microstructure of ZnO and their carbon composite is attractive route due to mainly two reasons. Firstly the morphology of ZnO is dramatically controlled by the physical and chemical properties of polymers in solution phase reaction.22-25 Secondly the as synthesized ZnO-polymer composites then can be pyrolysed to obtain ZnO-carbon composite which possesses several interesting properties albeit preserving the original shape and size rendering related functional properties. In this context there are several reports for the synthesis of metal oxide carbon composites but relatively very few reports for the synthesis of ZnO-carbon composites, starting from the polymer as a source of carbon [26-28].

Here we discuss the case of integrating ZnO nanostructure with a suitably chosen polymer poly (acrylic acid-co-maleic acid) sodium salt that on annealing at higher temperature (500^0C for 2 hrs) forms the functional form of carbon coated ZnO with hierarchical structure. We also show that the composite material synthesized by us not only shows excellent photocatalytic activity in the visible region (charge transfer enabled), but is also resistant to the degradation by dye. There are two major problems that arise when considering ZnO as a candidate for application involving photocatalysis. The first one is that it is well known that the ZnO nanoparticles are known to exhibit good UV photocatalytic activity, but are inefficient to show visible light photocatalysis due to its large band gap (3.2 eV). The property of visible light photocatalysis in ZnO appears if it is doped with suitable dopents [29, 30]. The other problem is that certain dyes used in photocatalytic reactions can leach this oxide through dye-solid reaction. The polar oxide surface of ZnO scavenge certain dye molecules and thereby forming the Zn2+-dye aggregates on the surface, which forbid the charge transfer across this layer [31]. This is also a known problem in the case of (N3) dye sensitized solar cells based on ZnO and TiO_2 [32-35]. This invites strategies for surface passivation especially for ZnO, but such strategies should not forbid charge transfer across the passivating layer because that would defeat the purpose of the related device action. In the light of these problems we show that the carbon coated ZnO exhibits visible light photocatalysis, by degradation of dye Methylene blue and also resistant to leaching of ZnO by dye-solid reaction.

6.2 Experimental Section

The polymer poly(acrylic acid-co-maleic acid) sodium salt (Mol Wt 50,000) was obtained from Sigma-aldrich Germany and zinc acetate dihydrate was obtained from SRL labs, India. The 0.5 gm polymer is added to a mixture of 0.5 gm of Zinc acetate and 1 gm of NaOH in 140 ml of de-ionized water at room temperature. This mixture was sonicated for 5 mins. The solution was then poured into a hydrothermal autoclave, which was tightly screwed and kept in the oven at 120 ^{0}C for 24 hours. The autocalave was then allowed to cool down naturally to the room temperature. The polymer coated ZnO powder was collected from the reaction mixture by centrifugation followed by several washings by de-ionised water and ambient drying. The as synthesized polymer coated ZnO powder was annealed at 500^{0}C for 2 hours in air atmosphere to obtain carbon coated ZnO. Optical spectroscopy measurements of the as synthesized and annealed polymer nanocomposite were carried out on a JASCO dual-beam spectrophotometer (model V-570) operated at a resolution of 1 nm. The phase composition was characterized using X-ray diffraction (XRD) and it was confirmed to be single phase ZnO. Scanning electron microscopy (SEM) measurements were performed on a field emission scanning electron microscopy (FESEM, Hitachi S-4200) instrument. The high resolution transmission electron microscopy were done using instrument FEI Tecnai 300. X-ray Photoelectron spectroscopy was performed using VG scientific ESCA-3000. Electrochemical measurements were performed with Autolab PGSTAT Potentiostat. The photocatalytic activity of carbon coated ZnO was examined by Methylene Blue degradation in CFL light (60 watt) illumination. The 100 ml solution of Methylene blue dye (1mg/100mL) is mixed with known amount of catalyst, and is exposed to CFL light. The photodegradation of dye is monitored by absorbance measurement of aliquots removed from the reaction mixture at time intervals.

4.3 Results and Discussion

Figure 6.1 shows the X-ray diffraction spectra of polymer coated ZnO and that of carbon coated ZnO. The XRD peaks in both the cases are marked for the corresponding crystal plane which signifies presence of Wurtzite crystal system of ZnO in both the cases. It can be seen that there is no increase in crystallite size, which can be clear from SEM and TEM images shown further in the text. This is due to fact that the carbon structure formed during heating process restricts further growth of the ZnO.

Figure 6.2 shows the TEM images of as synthesized carbon coated ZnO along with the SEM images of the polymer coated ZnO. SEM images clearly show the popcorn ball type morphology of polymer coated ZnO with hierarchical structure (fig. 6.2a). Also it shows a thick coating of the polymer coating around ZnO ultrathin nanoplatelets which resemble to a nanoflower-like morphology. Figure 6.2b and 6.2c shows the TEM images of as synthesized carbon coated ZnO. It clearly indicates that the nanoflower shape of ZnO is retained but the nanoplatelets of ZnO are converted to nanorod assembled structure. These carbon coated ZnO nanorod are randomly packed to form self-assembled carbon coated ZnO nanorod structure.

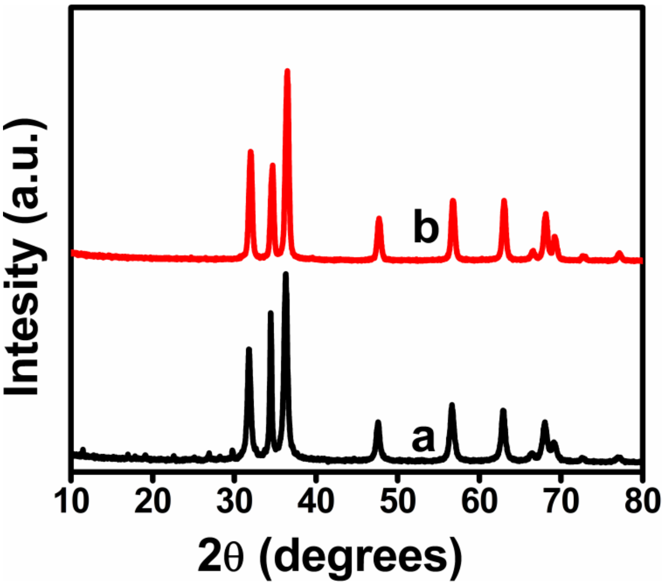

Fig. 6.1 *X-ray Diffraction spectra of polymer coated ZnO (curve a) and carbon coated ZnO (curve b).*

Figue 6.2d shows the HRTEM image of isolated carbon coated ZnO nanorod. The d-spacing is measured from the lattice fringes of the interior part and of the surface part of nanorod. The d-spacing profile shows two sets of d-spacing value with lattices constant of 0.345 nm at near surface and 0.268 nm in the interior part of ZnO as shown in figure 6.2d. The d-spacing of 0.268 nm corresponds to (002) crystallographic plane of ZnO (PCPDF data sheet PDF #800075). The d-spacing value of 0.345 nm on the surface part of nanorod corresponds to ((111) crystallographic plane of graphite) graphitic layers of carbon (PCPDF data sheet PDF #751621).

Figure 6.3A shows the Diffuse Reflectance Spectra of the polymer coated ZnO and carbon coated ZnO. Curve ‘a’ is for the polymer coated ZnO and Curve b is for the carbon coated ZnO respectively. There is considerable decrease in reflectance in the visible region which indicates increase in absorbance in that region in the later case. This can be attributed to the formation of carbon coating on the surface of ZnO. Also it can be noted that in the case of the carbon coated ZnO, a small narrowing of the band gap is noted. This can be attributed to the small decrease in band gap of ZnO, which is due overlap of carbon energy levels with that of zinc oxide (conduction band) which provides the electronic pathway for the charge transfer between the surface carbon layers and the ZnO nanostructure.

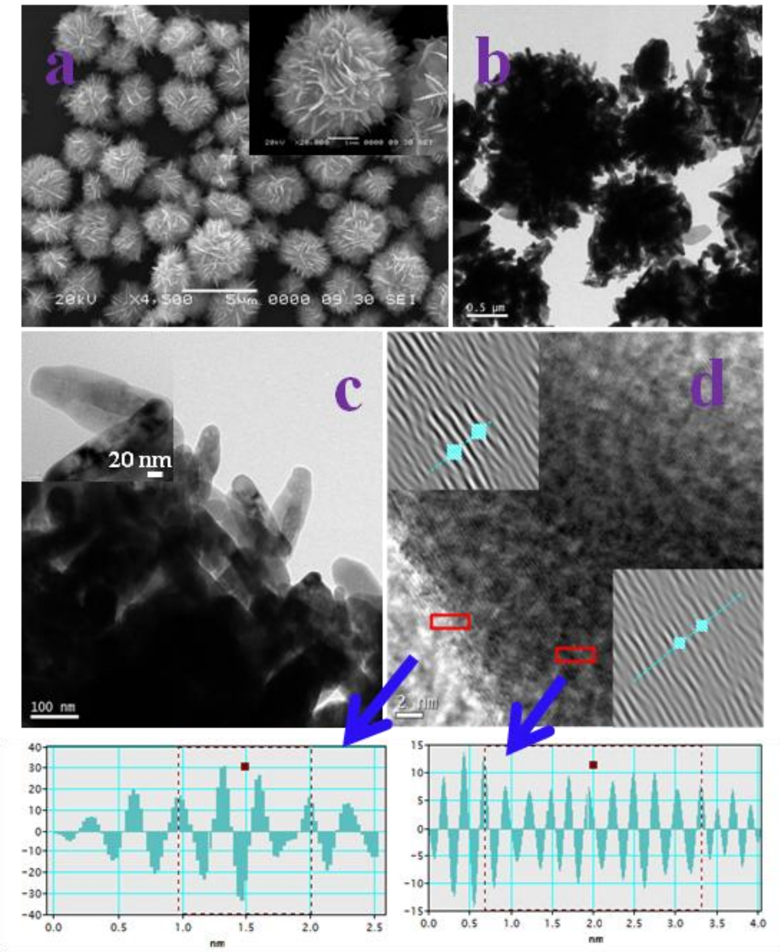

Fig. 6.2 *a) SEM image of polymer coated ZnO showing nanoflower morphology (inset shows single nanoflower) b) and c) carbon coated ZnO nanoflower (inset of c shows magnified image of single carbon coated ZnO nanorod) d) HRTEM image of carbon coated ZnO showing d-spacing profile at the bottom (left profile shows d-spacing of 0.347 nm and right profile shows d-spacing of 0.268 nm)*

Figure 6.3B shows the photoluminescence (PL) spectra of bare ZnO (curve a), polymer coated ZnO (curve b) and that of carbon coated ZnO (curve c). The observed optical structure involves free and bound excitonic transitions and a broad band (green) PL suggested to result from charged surface defect states (oxygen vacancies) [36,37]. In the case of the polymer coated ZnO no significant change is observed in the PL intensity or its optical structure as compared to the bare zinc oxide. In the case of the carbon coated ZnO the dramatic quenching of PL is observed over the visible range representing passivation of surface defect states. This indicates that annealing also leads to specific attachment of the carbon form on the surface of ZnO that cleans electronic surface defects of ZnO. It also indicates that there is coupling of ZnO electronic levels with carbon electronic levels.

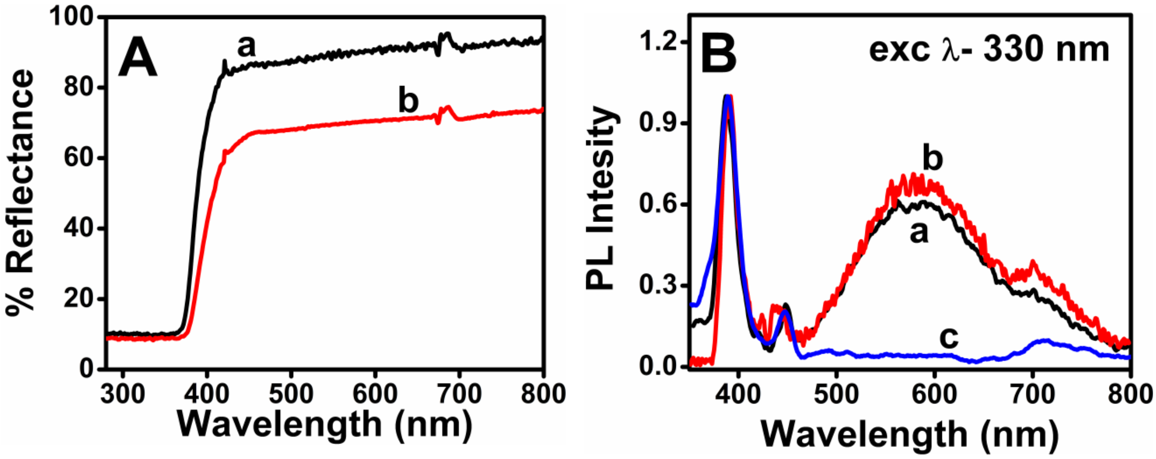

Fig. 6.3 *A) Optical DRS spectra and B) Photoluminescence (PL) Spectra of (curve a) polymer coated ZnO and (curve b) carbon coated ZnO. (In PL spectra, the data for (curve c) bare ZnO is also presented for comparison)*

Figure 6.4 shows the C1s core level X-ray photoelectron spectra of carbon coated ZnO. The O1s and Zn2p are given in supporting information. We have also compared the XPS spectra of bare ZnO (without using polymer in the synthesis protocol of ZnO and then annealed to get ZnO without carbon coating) for all the C1s, O1s and Zn2p levels. Both the samples i.e bare ZnO and carbon coated ZnO shows a peak at ~284.5 eV corresponding to graphitic (C-C sp^2 bonded) carbon [2, 3]. The intensity of this peak is very low in case of bare ZnO as compared to carbon coated ZnO. In case of bare ZnO this peak is due to carbon impurities that get adsorbed on the ZnO surface while synthesis. But presence of sharp peak with high intensity in case of carbon coated ZnO, confirms the presence of carbon coating on ZnO surface, as also discussed previously in TEM discussion earlier in the text. It is also interesting to note that in case of carbon coated ZnO, a broad and low intensity peak at higher binding energy ~ 288-289 eV arises, which is due to oxidized carbon [2, 3]. As the synthesis involves heating of polymer coated ZnO to 500^{0}C in air atmosphere to obtain carbon coated ZnO, which renders the outer surface of carbon to get oxidized. It is also important to note that the case of carbon coated ZnO should not be confused with the carbon doped ZnO. As in the case of carbon doped ZnO there is possibility of Zn-C bonding which peak in C1s XPS spectra at about 281 eV, which is not observed in our carbon coated ZnO case [30].

We further carried out the cyclic voltammetry of carbon coated ZnO in order to understand the energy level alignment of carbon electronic level with conduction and valence band of ZnO.

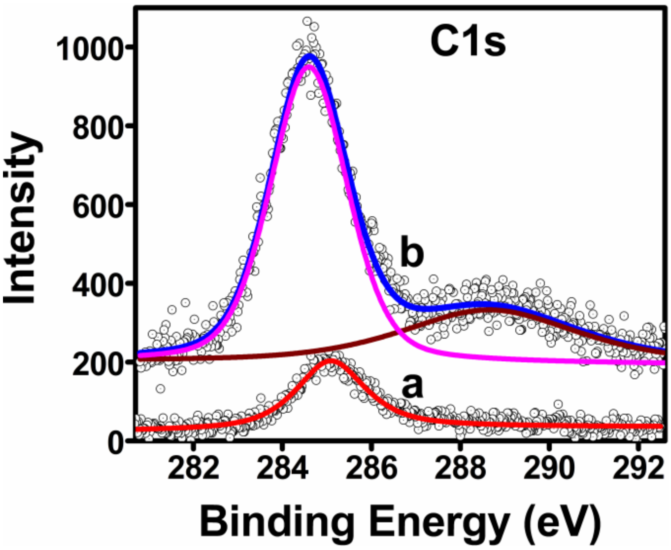

Fig. 6.4 *XPS C1s core level spectra of bare ZnO (curve a) and carbon coated ZnO (curve b).*

Figure 6.5A shows the typical cyclic voltammetric response of ferrocene, which is a redox couple and that of carbon coated ZnO. Ferrocene was used as external standard. Cyclic voltammetry results indicates a redox peak in case of carbon coated ZnO at E_{red}= -0.03 V. Also from the CV data of ferrocene, two peaks are observed at 0.33 and 0.43 V, from which $E_{1/2(ferrocene)}$ is calculated to be 0.38 V. From the equation E_{carbon}= $[(E_{red}- E_{1/2(ferrocene)}) +4.8]$ eV, the value of E_{carbon} calculated as 4.39 eV. Figure 6.5B shows the band diagram of carbon energy level with respect to conduction and valence band of ZnO [38]. The energy level of carbon is just below the conduction band of ZnO by 0.04 eV. From the vacuum level it is located at 4.39 eV. Our results are consistent with the earlier reports on location of carbon energy level with respect to vacuum level [2, 39-40].

The photocatalytic performance of ZnO was checked by following the photocatalytic degradation of MB under visible light irradiation. The photocatalysis experiments were done using a CFL lamp (65 W), which has little emission in the UV range. Figure 6.6 shows the photodegradation profile of methylene blue (MB) dye in the presence of carbon coated ZnO and without catalyst. It is also observed that the MB dye is degraded to a very small extent under visible light irradiation in the absence of the photocatalyst. The photocatalytic degradation efficiency of carbon coated ZnO system is calculated to be 85%. As it is well known that pure ZnO has band gap of 3.2 eV with absorption mainly in the UV region, it cannot harvest the visible light efficiently. Therefore the degradation of MB must take place due to due photosensitization process.

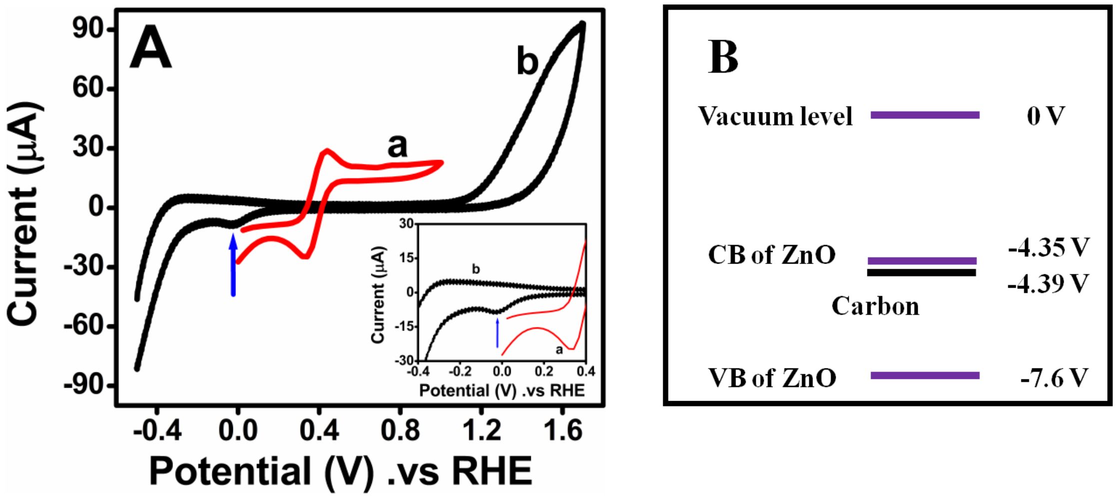

Fig. 6.5 *A) CV curves of redox couple ferrocene (curve a) and of carbon coated ZnO (curve b) B) Band diagram and energy level alignment of carbon with respect to that of ZnO in carbon coated ZnO system*

In this context, it is important to mention that there are many reports for the degradation of dye by metal oxide-carbon system under the irradiation of visible light [2, 3, 4, 39]. It can be inferred from the relevant band positions of ZnO, carbon and MB dye (as shown in scheme 6.1) that there is an easy transfer of photo-induced electrons from the dye to carbon and then to ZnO conduction band [41]. The heterogeneous system separates the photo-induced electrons and holes efficiently and avoids the charge recombination in electron-transfer processes. As shown in scheme 6.1, the MB dye after excitation by visible light irradiation, transfer the photo excited e^- to ZnO or to carbon.

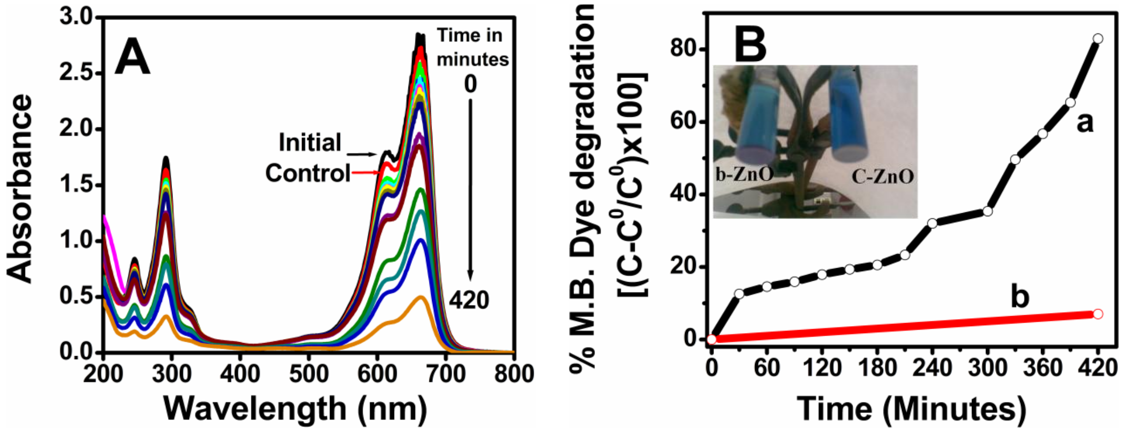

Fig. 6.6 *Photodegradation of methylene blue (MB) dye in the presence of Carbon coated ZnO A) Decrease in absorbance of MB dye with respect to time B) % dye degradation with respect to time (curve a) with catalyst and (curve b) without catalyst. Inset of B) shows the formation of* Zn^{2+}*-dye aggregates in case of bare ZnO (b-ZnO) and carbon coated ZnO (C-ZnO) shows no such formation* Zn^{2+}*-dye aggregates.*

But the probability of electron recombination between the injected electron to ZnO and the surface adsorbed dye is more. This is due to slow mobility of e^- in metal oxide. On the other hand when the photo excited e- is transferred to carbon, there is very less or negligible probability of electron recombination between the injected electron in carbon and the surface adsorbed dye. Also the carbon energy levels are nearly overlapping with that of conduction band of ZnO, this injected electron can be further injected into ZnO conduction band. As carbon layer avoids the direct interaction of dye and ZnO it is more probable that the electron on the ZnO surface is trapped by dissolved oxygen to form various reactive oxygen species (ROSs), thereby degrading the MB dye. The role of carbon coating on ZnO is not limited to only visible light photocatalysis, but this layer also protects leaching of Zn^{2+} ions from ZnO. As it is well known that certain dyes used in photocatalytic reactions can leach this oxide through dye-solid reaction. The polar oxide surface of ZnO[31] scavenge certain dye molecules and thereby forming the Zn^{2+}-dye aggregates on the surface, which forbid the charge transfer across this layer. Thus it further prevents the charge transfer reaction from photocatalyst to dye molecule. In our case the carbon layer also acts protecting layer for ZnO so as to forbid the leaching of Zn^{2+} from ZnO and therby prevents the formation of Zn^{2+}-dye aggregates as shown in figure 7.

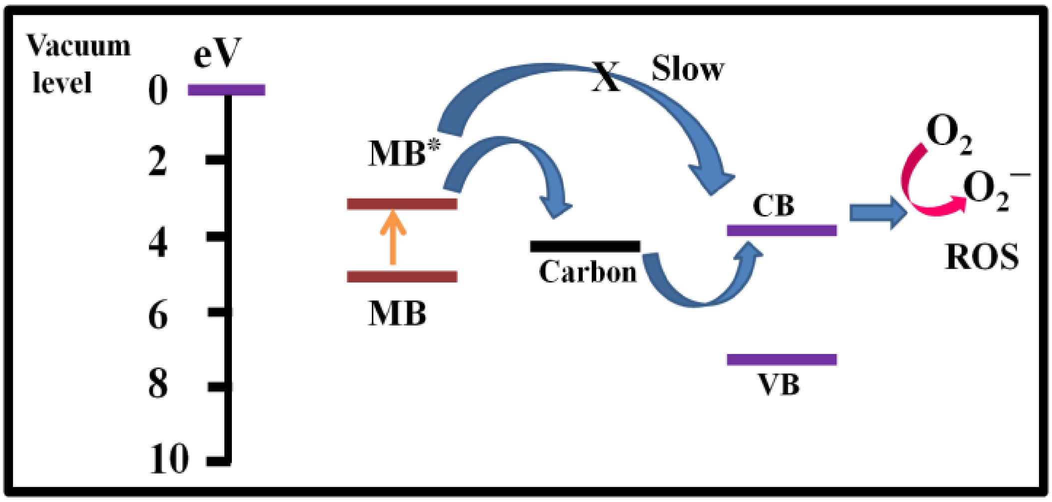

Scheme 6.1 *Energy level diagrams of MB dye, carbon coated ZnO and the possible mechanism of photocatalysis process*

It is important to point out that the MB dye is seen to be scavenged by the pure ZnO (see the blue color of the powder at the bottom of the bottle on the left in figure 5B inset, but when the carbon coated ZnO is added to solution of MB dye, this scavenging is not seen (see the white color of the powder at the bottom on the right side bottle in figure 5B inset). The denser blue color of this right side as compared to the left side bottle further emphasizes that the dye is not scavenged by the carbon coated ZnO. It proves that this carbon coating on ZnO facilitates the efficient electron transfer during photocatalysis between dye molecules and ZnO and also avoids scavenging of dye molecules on ZnO surface.

4.4 Conclusion

Polymer hybrid of ZnO nanoplatelates are synthesized by hydrothermal reaction. It exhibits hierarchical popcorn ball-like structure consisting of ZnO nano-platelates. The polymer coated ZnO nano-platelates are then annealed in air at 500^0C for 2 hours to obtain anisotropic structure of carbon coated ZnO nanoroads. The as-synthesized carbon coated ZnO nanorods show improved visible light photocatalytic activity. Moreover these are also resistant to degradation by and scavenging of the dye without hindrance to charge transfer; a characteristic of significant interest to optical device applications.

4.5 Reference

[1] X. Wang, P. Hu, Y. Fangli, L. Yu, *J. Phys. Chem. C,* **2007**, *111*, 670.

[2] T. Lv, L. Pan, X. Liu, Z. Sun, *Catal. Sci. Technol.,* **2012**, *2*, 2297.

[3] J. Zhang, Z. Xiong, X. S. Zhao, *J. Mater. Chem.*, **2011**, *21*, 3634.

[4] Q. Luo, X. Yu, B. Lei, H. Chen, D. Kuang, C. Su, *J. Phys. Chem. C,* **2012**, *116*, 8111.

[5] L. L. Zhang, X. S. Zhao, *Chem. Soc. Rev.*, **2009**, *38*, 2520.

[6] L. Zhang, R. Zhou, X. Zhao, *J. Mater. Chem.*, **2010**, *20*, 5983.

[7] Z. Li, N. Liu, X. Wang, C. Wang, Y. Qi, L. Yin, *J. Mater. Chem.*, **2012**, *22*, 16640.

[8] Z. L. Wang, *J. Phys.:Condens. Matter,* **2004**, *16*, R829.

[9] M. Y. Cheng, B. J. Hwang, *J. Power Sources,* **2010**, *195*, 4977.

[10] M. H. Huang, S. Mao, H. Feick, H. Q. Yan, Y. Y. Wu, H. Kind, E. Weber, R. Russo, P. D. Yang, *Science*, **2001**, *292*, 1897.

[11] H. Rensmo, K. Keis, H. Lindstrom, S. Sodergren, A. Solbrand, A. Hagfeldt, S. E. Lindquist, L. N. Wang, M. Muhammed, *J. Phys. Chem. B*, **1997**, *101*, 2598.

[12] W. I. Park, G. C. Yi, *Adv. Mater.*, **2004**, *16*, 87.

[13] M. H. Zhao, Z. L. Wang, S. X. Mao, *Nano Lett.*, **2004**, *4*, 587.

[14] L. Vayssieres, *Adv. Mater.*, **2003**, *15*, 464.

[15] W. Pan, Z. R. Dai, Z. L. Wang, *Science,* **2001**, *291*, 1947.

[16] R. R. Tian, J. A. Voigt, J. Liu, B. McKenzie, M. J. McDermott, M. A. Rodriguez, H. Konishi, H. F. Xu, *Nat. Mater.*, **2003**, *2*, 821.

[17] J. Q. Hu, Q. Li, X. M. Meng, C. S. Lee, S. T. Lee, *Chem. Mater.*, **2003**, *15*, 305.

[18] J. Q. Hu, Y. Bando, J. H. Zhan, Y. B. Li, T. Sekiguchi, *Appl. Phys. Lett.*, **2003**, *83*, 4414.

[19] M. Mo, J. C. Yu, L. Zhang, S.K. A. Li, *Adv. Mater.* **2005**, *17*, 756.

[20] P. Hu, N. Han, X. Zhang, M. Yao, Y. Cao, A. Zuo, G. Y. F. Yuan, *J. Mater. Chem.*, **2011**, *21*, 14277.

[21] R. Ding, J. Liu, J. Jiang, Y. Li, Y. Hu, X. Ji, Q. Chi, F. Wu, X. Huang, *Chem. Commun.*, **2009**, 4548.

[22] N. Jochen, H. M. Wolfgang, W. Gerhard, *Chem. Mater.* **1998,** *10,* 460.

[23] T. Andreas, G. Gunnar, P. Dennis, *Langmuir* **2002,** *18,* 4488.

[24] P. Yin, X. An-Wu, D. Bin, A. Markus, C. J. Helmut, *J. Phys. Chem. B* **2006,** *110,* 2988.

[25] G. Yanfeng, N. Masayuki, *Langmuir* **2006**, 22, 3936.

[26] Z. Yang, J. Shen, L. A. Archer, *J. Mater. Chem.*, **2011**, *21*, 11092.

[27] H. Chien , W. Cheng , Y. Wang, S. Lu, *Adv. Funct. Mater.*, **2012**, *22*, 5038.

[28] M. Inagaki, Y. Yang, F. Kang, *Adv. Mater.*, **2012**, *24*, 2547.

[29] V. Etacheri, R. Roshan, V. Kumar, *ACS Appl. Mater. Interfaces*, **2012**, *4*, 2717.

[30] S. Cho, J. Jang, J. S. Lee, K. Lee, *CrystEngComm*, **2010**, *12*, 3929.

[31] G. R. Li, G. L. Pan, T. Y. Yan, X. P. GaO, H. Y. Zhu, *J. Phys. Chem. C*, **2008**, *112*, 11859.

[32] H. Hiroaki, K. Ryuzi, H. Kohjiro, Y. Masatoshi, M. Shigeo, A. Hironori, M. Tachiya, *J.Phys.Chem.B.*, **2003**, *107*, 2570.

[33] K. Ryuzi, F. Akihiro, T. Yoshiaki, Y. Toshitada, M. Miki, H. Kohjiro, M. Shigeo, A. Hironori, M. Tachiya, *Journal of Photochemistry and Photobiology A: Chemistry*, **2004**, *166*, 69.

[34] W. Bernard, G. Michael, E. M. Jacques, *J. Am. Chem. Soc.* **2005**, *127*, 12150.

[35] C. K. Ali, H. Surat, D. Suresh, P. V. Kamat, *J. Phys. Chem. B*, **1999**, *103*, 4693.

[36] M. Anpo, Y. Kubokawa, *J. Phys. Chem.*, **1984**, *88*, 5556.

[37] T. Sun, J. Qiu, C. Liang, *J. Phys. Chem. C*, **2008**, *112*, 715.

[38] Z. Sun, C. Wang, J. Yang, B. Zhao, J. R. Lombardi, *J. Phys. Chem. C*, **2008**, *112*, 6093.

[39] B. Li, H. Cao, *J. Mater. Chem.*, **2011**, *21*, 3346.

[40] H. Hibino, H. Kageshima, M. Kotsugi, F. Maeda, F.Z. Guo, Y. Watanabe, *Phys. Rev. B*, **2009**, *79*, 125437.

[41] P. R. Somani, S. Radhakrishnan, *Chem. Phys. Lett.*, **2003**, *379*, 401.

....

CHAPTER VII

Conclusions and Future Scope

This chapter presents the principal outcomes and conclusions of the present doctoral study. Additionally we have also discussed some future prospects of the current work.

7.1 Summary of the thesis

The technological and scientific potentials of carbon based materials is certainly bright as revealed in the present study on carbon nanoscrolls, porous graphene, single sheet graphene, magnetite-graphene oxide, carbon coated ZnO etc. These are essentially the nanostructures of carbon of graphitic origin. Moreover the ultimate use of these carbon nanostructures is strongly dependent upon the ability to precisely control their dimension and surface property like porosity and surface area. As the basic building block of these carbon nanostructures is a sheet of carbon in hexagonal network (graphene), these structures have very high surface area together with enhanced conductivity, which is important for many applications. This work hence opens the new perceptive towards promising synthesis methods and developments of graphene based nanostructures to stretch the applications of these fascinating nanomaterials in the field of energy and environment. Finally, some of the future prospects of these carbon nanostructured materials are explained within the broad perspective.

During the course of the present research work, we have investigated various methods for the synthesis of carbon based nanomaterials and their applications for energy storage, field-effect transistor and photocatalysis.

The salient features of the results are as follows:

1. We have demonstrated the catalyst free efficient route for the synthesis of carbon nanoscrolls starting from pyrolysis of polymer. Pyrolysis of poly (acrylic acid co maleic acid) sodium salt leads to formation of carbon form and sodium carbonate. The carbon part of decomposition products undergo self-assembly upon its aqueous soaking to form carbon nanoscrolls. We find that the as synthesized carbon nanoscrolls have ordered structure with interlayer distance of 0.34 nm. We have also demonstrated the synthesis of magnetite-graphene oxide (M-GO) composite by pyrolysis route. In this work, a mixture of poly (acrylic acid-co-maleic acid) sodium salt and an Fe-complex [Fe(III) (2'-hydroxy chalcone)3] is pyrolyzed at 500^{0}C for 2 hours in air atmosphere. Upon soaking in water, this pyrolysis product leads to formation of Magnetite-graphene oxide (M-GO) composite. This is very simple and catalyst free route for the synthesis of M-GO composites. The composite also possesses excellent magnetic as well as surface area properties which are very important in the context of many applications.

2. We have synthesized hierarchically porous graphene with hexagonal nonopores. It is a catalyst-free synthesis leading to single-layer-graphene-assembled carbon without use of any template. The as-synthesized sample exhibits high surface area of about 1720 m^2/g and shows bulk specific conductivity of 23 S/m. The material exhibits excellent supercapacitance performance in aqueous medium with maximum specific capacitance of 154 F/g at a current density of 0.5 A/g. It also shows good stability at higher current densities and after 1000 charge discharge cycles without any apparent sign of decay rate even for further cycling.

3. We have synthesized large area single layer graphene. It is a catalyst-free synthesis without use of any template. The as-synthesized graphene exhibits high surface area of about 350 m^2/g and shows bulk specific conductivity of 90 S/m. This graphene also shows good CV behaviour with approximate specific capacitance of 120-140 F/g. We have used this graphene for making graphene/P3HT composite and used this composite as a channel material for field effect transistor application. We have shown that effective mobilities of P3HT/graphene hybrid FETs can be significantly higher than that of a pure P3HT FET. But at the same time the on/off ratio of hybrid FETs significantly decreased when the concentration of graphene in semiconductor film was increase. This is due to exceeding the percolation threshold of graphene in the composite.

4. Polymer hybrid of ZnO nanoplatelates were synthesized by hydrothermal reaction. It has hierarchical popcorn ball structure consist of ZnO nanoplatelates. The polymer coated ZnO nanoplatelates is then annealed in air at 500^0C for 2 hours to obtain anisotropic structure of carbon coated ZnO nanoroads. The as synthesized carbon coated ZnO shows efficient visible light photocatalytic activity. Moreover it is also resistant to degradation by and scavenging of the dye without hindrance to charge transfer; a characteristic of significant interest to optical device applications.

7.2 Scope for future work

Graphene is wonder material for many applications like energy storage (as electrode material in supercapacitors, batteries etc.), hydrogen storage and for many other optoelectronic and catalytic applications. Due to the two dimensional structure, graphene can be molded into various interesting shapes and sizes in three dimensional architecture, still retaining or even enhancing the properties of graphene. Also there are not many synthesis methods for bulk production of graphene with good control on morphology. This is the major hurdle for utilizing graphene for such applications. Other method like CVD can produce graphene but only in the form of a thin film. Hence large amount synthesis of graphene is a real challenge in this field.

Therefore synthesis of graphene from the Pyrolysis of polymers is very attractive technique for number of reasons.

1. Polymers are not so costly and easily available or can be synthesized in the lab.
2. If pyrolysis is catalyst free, it is very good for purification of carbon (graphene) material at low cost and no problem of catalyst recovery.
3. Large scale synthesis is possible for pyrolysis process.

So mainly due to these reasons, pyrolysis of polymers is an attractive method for synthesis of graphene and allied materials. The main question now remains whether it is possible to obtain such a materials at large scale or not? In this regard, it is important to mention that the work presented in this study will be useful. In this work we have used copolymers containing either acrylic acid or maleic acid or both, namely poly (acrylic acid-co-maleic acid) sodium salt, poly (4-styrenesulfonic acid-co-maleic acid) sodium salt, poly (acrylic acid) sodium salt. From our study it is understood that, the advantage of sodium salt of these polymers is that we can synthesize single sheet graphene on large scale. This is because on pyrolysis of sodium salt of these polymers the sodium carbonate a bi-product generates within the process keeps graphene sheets apart by intercalating within any two graphene sheets. This bi-product also helps to create micropores and mesopores in the carbon structure obtained after pyrolysis. The speciality of these types of polymers is that, there is no need of catalyst for the synthesis of graphene from these polymers by pyrolysis method and easy to control. As stated above, we have studied 3 different polymers for the study, where we could find a mechanism of cross-linking of these polymers on pyrolysis to form graphene sheets. Although we have studied only three cases of polymer pyrolysis for the completion of Ph.D, there can be a detailed scientific study on this issue, where we can use one or more copolymer combinations of these acrylic acid and maleic acid units along with the chemically similar monomers. Alternatively we can synthesize different copolymers of various combinations of the repeating units in the lab and then use them for pyrolysis. This approach can generate different morphologies of graphene in 2D as well as 3D architecture.

Also thin films of graphene can be deposited on substrates like n-type silicon or quartz by pyrolyzing the acid form (-COOH) of these types of polymer. The spin coating of very thin layer of polymer can be coated on the substrates like quartz or n-type silicon with thin SiO_2 as dielectric layer, and then can be pyrolysed very quickly in argon at high temperature to obtain graphene film. The study of such very thin films of graphene, is very important for some applications like graphene based FET (field effect transistor), sensor and other possible opto-electronic property based applications of graphene.

APPENDIX: Observation of unusual and strong Ferroelectricity in hydrated sodium carbonate

The discovery of very first piezoelectric material Rochelle salt by Valasek, initiated the research interest of scientist in the field of ferroelectricity [1]. Its nearly a century has gone past, for the understanding of the physical phenomenon underlying ferroelectricity and piezoelectricity. Studying ferroelectricity, not only enriches our understandings but also gives a new route for potential applications like ferroelectric random access memory (FeRAM) and ferroelectric field-effect transistors etc. [2-7]. The search for better ferroelectrics is still continuing with the advent of modern science. Ferroelectrics are the ordered polar materials which can generate spontaneous electric polarization on the application of external electric field. These can be either solid (crystalline or polymeric) or liquid crystal, in which spontaneously generated electric polarization can be reversed by inverting the external electric field [8-13]. The hysteresis observed in the polarization, dielectric function, and strain of these materials has been studied and there are theories which accounts for the anomalous dielectric, piezoelectric, elastic, and phase transition behaviors in these materials. The observations of ferroelectricity were first made by the study of ionic solids like KH_2PO_4, but today the world of ferroelectrics is immensely dominated by inorganic and organic materials [8-11, 14]. The first report of ferroelectricity in $BaTiO_3$ and related perovskite-structure oxides in the 1940 stimulated the research in this field [15]. With further understanding of fundamental physics underlying phenomenon of ferroelecticity, new organic based ferroelectrics like PVDF (poly (vinylidene difluoride)), Thiourea, TEMPO etc. have been discovered [14]. In any of these, either inorganic or organic materials the ferroelectricity results from the phase transitions in solids, where a paraelectric state is transformed into ferroelectric state. The phase transition in ferroelectrics is usually categorized as either displacive or order–disorder type. In the order disorder type, the most accepted mechanism is that of the sodium nitrite ($NaNO_2$) case, where the permanent dipoles of the polar molecules or ions generate spontaneous polarization, and their reorientation generates the ferroelectricity. In the ferroelectric state the dipole moments are ordered without canceling each other out, whereas the paraelectric state corresponds to disorder in their orientations. Although according to some reports, ferroelectricity in $NaNO_2$ is not of purely order–disorder type but also contributed by displacive nature of sodium [16]. The example for the pure displacive nature of ferroelectrics is that of $BaTiO_3$, where an ion is displaced from equilibrium slightly, hence the force from the local electric fields due to the ions in the crystal increases faster than the elastic-restoring forces. This leads to an asymmetrical shift in the equilibrium ion positions and hence leads to a permanent dipole moment. The ionic displacement in barium titanate concerns the relative position of the titanium ion within the oxygen octahedral cage, which is hence important to account for observed ferroelectricity in these types of materials. Apart from these materials there are reports for the observation of ferroelectricity in the water in its ice form [17-19]. Still there is a debate, whether the bulk ice can or cannot be a ferroelectric (FE) material. Water molecules are dipolar and thus ferroelectric alignment of water molecules is conceivable when water freezes into special forms of ice. Although evidence of a fully proton ordered ferroelectric ice is still elusive. Also there are reports for the observation of ferroelectricity in metal-organic framework [20].

In the light of these reports we are reporting a new ferroelectric phase ordering that take place in the hydrated sodium carbonate. The dielectric and ferroelectric properties of this hydrated sodium carbonate are better and comparable with that of the ferroelectric materials already known to world. We have given the table of selected existing ferroelectrics that have better properties in terms of dielectric constant, coercive field and spontaneous polarization at room temperature and an extended table comprising of all the ferroelectrics known to us is given in the supporting information. The structural measurements were carried out using X-ray diffraction. Raman studies are carried out to study the phase evolution of the material. Dielectric and ferroelectric analysis were carried out to study the electrical properties of the material.

Figure A-1 shows the TEM images of hydrated sodium carbonate (predominantly sodium carbonate monohydrate) crystals. These are orthorhombic crystals of micrometer size range. Figure A-2A shows the XRD spectrum of hydrated sodium carbonate (sodium carbonate monohydrate). The peaks are matched with the PCPDF data base PDF# No 760910. The peaks correspond to sodium carbonate monohydrate [21]. The sharp peaks in the XRD spectrum crystalline nature of sodium carbonate monohydrate. Figure A-2B shows the Raman spectrum of hydrated sodium carbonate (sodium carbonate monohydrate). Raman is only sensitive to symmetric molecules or crystal structure. The carbonate anion possesses the symmetry in the plane of carbonate anion hence is only Raman active. It shows the very high intensity peak at 1070 cm^{-1}. Also there are two more peaks at ~700 and ~1430 cm^{-1} are observed for sodium carbonate but these are very weak [22,23].

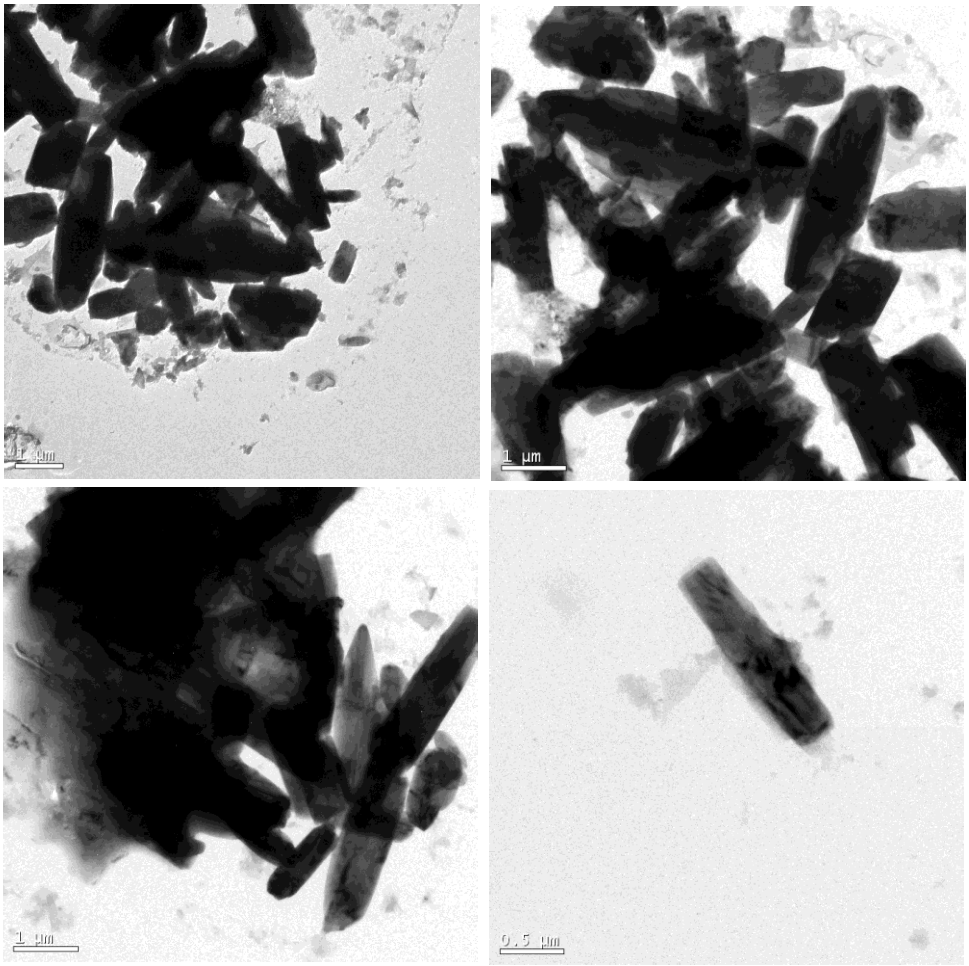

Fig. A-1. *TEM images of hydrated sodium carbonate*

Figure A-3 shows the variation of the relative dielectric constant versus frequency of hydrated and anhydrous sodium carbonate at room temperature (300^0K). We performed dielectric property measurements on a pellet made of anhydrous sodium carbonate and sodium carbonate monohydrate. The dielectric constant of hydrated sodium carbonate composite is extremely high (10^3 times at 100 Hz) as compared to that of pure sodium carbonate. The intrinsic polarizability of sodium carbonate is very low, so the enormous increase in relative dielectric constant in hydrated sodium carbonate is due to due to interaction between water molecules and sodium carbonate. The relative dielectric constant increases as the frequency decreases, which signifies that the all 3 types of polarization i.e. electronic, atomic or molecular and orientation polarization exist in the system. Of these the orientation polarization occurs only in materials consisting of molecules or particles with a permanent dipole moment. Also it should be noted that the dielectric constant of composite is very high (10^6) at lower frequency as compared to frequencies corresponding to kilohertz and megahertz region, which signifies that the orientation polarization is strongly exist and dominant in the hydrated sodium carbonate, which is responsible for ferroelectric polarization in the composite.

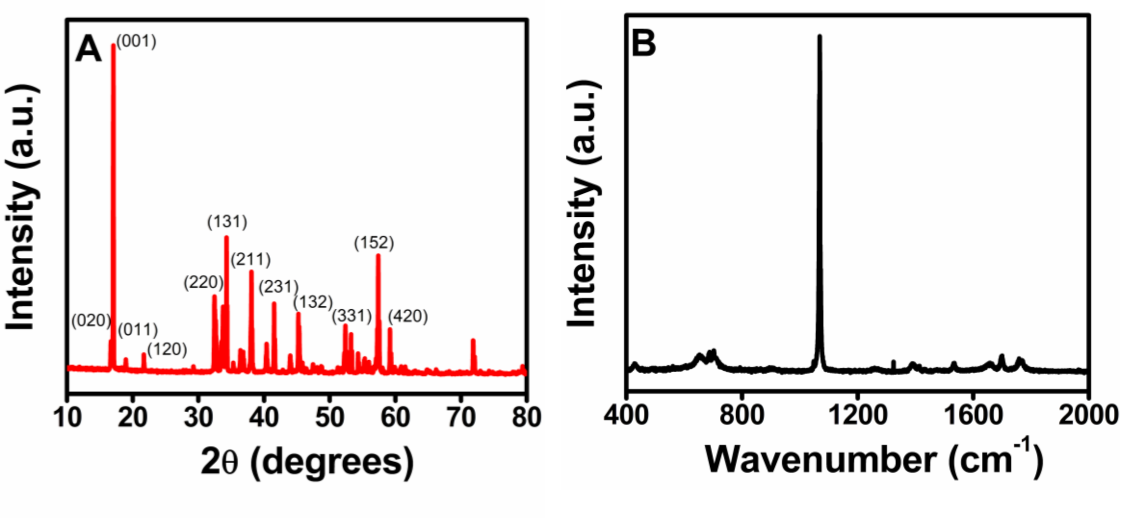

Fig. A-2. *A) XRD spectrum and B) Raman spectrum of sodium carbonate monohydrate*

Figure A-4A shows the P-E hysteresis curve for the hydrated sodium carbonate. We performed ferroelectric property measurements on a pellet made of sodium carbonate monohydrate. It shows a strong ferroelectric response with a square loop. The value of saturation polarization is found to be ~20 μC/cm^2.

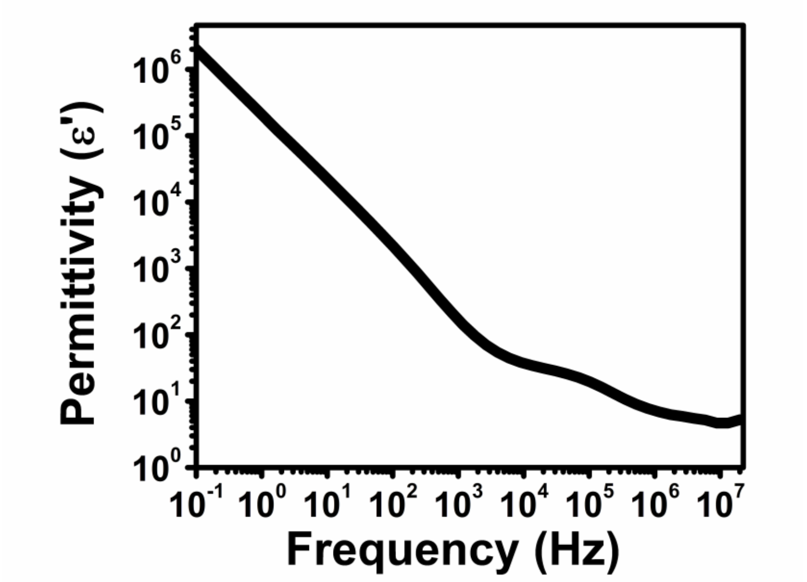

Fig. A-3. *Dielectric data of sodium carbonate monohydrate*

The coercive field is about 4 kV. The value of saturation polarization and coercive field are dependent on the amount of hydration of sodium carbonate, as discussed next, and hence these properties can be tuned with degree of hydration of sodium carbonate.

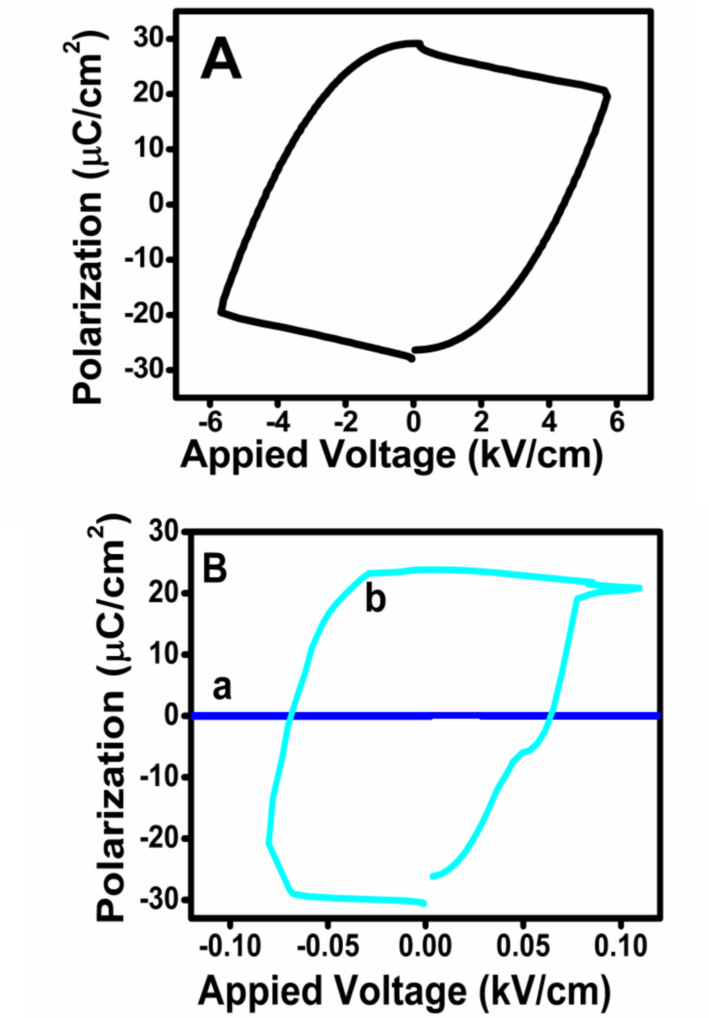

Fig. A-4. *A) Ferroelectric hysteresis loop of sodium carbonate monohydrate. B) curve (b) signifies the ferroelectric hysteresis loop of sodium carbonate monohydrate after exposure to mild vacuum condition and (c) after exposure to 80% humidity condition*

The observation of ferroelectricity in the hydrated sodium carbonate was rather unexpected. It was therefore interesting to find out whether either anhydrous or hydrated form of sodium carbonate is responsible for ferroelectricity. To our knowledge there is no report of ferroelectricity in sodium carbonate. Anhydrous sodium carbonate is monoclinic having trigonal bi-pyramidal structure and hence should not be not ferroelectric (symmetry considerations) [21]. On the other hand sodium carbonate monohydrate (SCM) is orthorhombic having space group P21ab (PCPDF data base, PDF No #760910) which is non-centrosymmetric and thus could support ferroelectricity. To test our hypothesis, the pellet was kept separately in vacuum and moisture desiccators for several hours and then ferroelectric measurements were performed. Figure A-4B shows the effect of humidity on ferroelectric response of sodium carbonate. When the pellet was kept in vacuum desiccator for several hours the ferroelectric response vanished and when the pellet was kept in moisture desiccator for several hours, it showed a strong ferroelectric response. This confirms that hydration in sodium carbonate holds the key to ferroelectricity.

Methods

Transmission Electron Microscopy was done using FEI Tecnai T20. The X-ray diffraction data were recorded by Panalytical Powder XRD Xpert-1712. The dielectric measurements were carried out using Novocontrol broadband dielectric spectrometer at room temperature. The Ferroelectric measurement was done by the ferroelectric test system TF Analyzer 2000 FE by aixACCT systems GmbH Germany. The ferroelectric and dielectric measurements were taken on a palate made of the anhydrous as well as hydrated sodium carbonate. The area of palate was ~1cm^2, and thickness was ~2 mm.

References

[1] J. Valasek, *Phys. Rev.***1921**, *17*, 475.

[2] S. Ducharme, A. Gruverman, *Nature Mater.*, **2009**, *8*, 9.

[3] P. R. Evans, *Nano Lett.*, **2007**, *7*, 1134.

[4] R. C. G. Naber, *Nature Mater.*, **2005**, *4*, 243.

[5] S. Mathews, *Science*, **1997**, *276*, 238.

[6] J. Y. Son, *ACS Nano*, **2010**, *4*, 7315.

[7] W. Fu, *Nano Lett.*, **2009**, *9*, 921.

[8] R. E. Cohen, *Nature*, **1992**, *358*, 136.

[9] A. Bussmann-Holder, H. Böttner, *Nature*, **1992**, *360*, 541.

[10] T. Furukawa, *Phase Trans.*, **1989**, *18*, 143.

[11] T. Furukawa, M. Date, E. Fukada, *J. Appl. Phys.*, **1980**, *51***,** 1135.

[12] G. W. Taylor, (ed.). *Ferroelectric Liquid Crystals — Principles, Preparations and Applications*, **1991**, Gordon & Breach, New York.

[13] S. T. Largerwall, *Ferroelectric and Antiferroelectric Liquid* Crystals, **1999**, Wiley-VCH, Weinheim.

[14] S. Horiuchi, Y. Tokura, *Nature Mater.***2008**, *7*, 357.

[15] A. V. Hippel, R. G. Breckenridge, F. G. Chesley, L. Tisza, *High dielectric constant ceramics.* **1946**, *38*, 1097.

[16] M. Ichikawa, *Solid State Commun.*, **2002**, *123*, 135.

[17] S. T. Bramwell, *Nature*, **1999**, *397*, 212.

[18] C. F. Luo, W. Fa, J. Zhou, J. M. Dong, X. C. Zeng, *Nano Lett*, **2008**, *8*, 2607.

[19] F. Mikami, K. Matsuda, H. Kataura, Y. Maniwa, *ACS Nano*, **2009**, *3*, 1279.

[20] G. Xu, X. Ma, L. Zhang, W. Wang, S. Gao, *J. Am. Chem. Soc*, **2010**, *132*, 9588.

[21] A. Seyrankaya, B. Ozalp, *Thermochimica Acta.*, **2006**, *448*, 31.

[22] H. Meekes, T. Rasing, P. Wyder, A. Janner, T. Janssen, *Physical Review B*, **1986**, *34*, 4240.

[23] I. A. Degen, G. A. Newman, *Spectrochimica Acta*, **1993**, *49*, 659.

……………………………….

LIST OF PUBLICATIONS

---

1. Controlling Stoichiometry in Low Temperature Synthesis of $La_{0.7}Sr_{0.3}MnO_3$ Nanoparticles, Azarifar, Ali; **Yadav, P.A.**; Chawla, A.K.; Jog, J.P.; Patil, S.I.; Chandra, R.; Ogale, S.B. *Advanced Science Letters*, **2011**, *4*, 424-430.

2. Magnetite/CdTe magnetic–fluorescent composite nanosystem for magnetic separation and bio-imaging, Anup Kale, Sonia Kale, **Prasad Yadav**, Haribhau Gholap, Renu Pasricha, Jyoti Jog, Benoit Lefez, Beatrice Hannoyer, Padma Shastry and Satishchandra Ogale. *Nanotechnology*, **2011**, *22*, 225101.

3. Carbon nanoscrolls by pyrolysis of a polymer. **Prasad Yadav**, Sambhaji Warule, Jyoti Jog, Satishchandra Ogale. *Solid state communications*, **2012**, *152*, 2092-2095.

4. Single A 3D Hexaporous Carbon Assembled from Single-Layer Graphene as High Performance Supercapacitor, **Prasad Yadav**, Abhik Banerjee, Sreekuttan Unni, Jyoti Jog, Sreekumar Kurungot and Satishchandra Ogale. *ChemSusChem.*, **2012**, *5*, 2159-2164.

5. Nanoparticle-loaded multifunctional natural seed gel-bits for efficient water purification. Mandakini Biswal, Kirti Bhardwaj, Pradeep K Singh, Pooja Singh, **Prasad Yadav**, Asmita Prabune, Chandrashekhar Rode, Satishchandra Ogale. *RSC Advances*, **2012** (accepted).

6. Advanced Functionality of CdTe-TiO_2 Nanocomposite as a Quorum Sensing Inhibitor. Haribhau Gholap, Rajendra Patil, **Prasad Yadav**, Arun Banpurkar, Satishchandra Ogale, Wasudeo Gade. *Nanotechnology*, **2012** (under review).

7. From particulate-like to flaky-faceted $La_{0.7}Sr_{0.3}MnO_3$ by citrate chelating: Consequences for magnetism and RF hyperthermia. Shreelekha Khatavkar, Onkar Game, Mandakini Biswal, Anil Jadhav, **Prasad Yadav**, Sambhaji Warule, Sangeeta Kale, Satishchandra Ogale. *Journal of applied physics*, **2012** (under review).